

## ABSTRACT

Title of thesis: THERMAL VACUUM TEST CORRELATION  
OF A ZERO PROPELLANT LOAD CASE  
THERMAL CAPACITANCE PROPELLANT  
GAUGING ANALYTICAL MODEL

Stephen A. McKim, M.S. Aerospace Engineering, 2016

Thesis directed by: Associate Professor Christopher Cadou  
Department of Aerospace Engineering

This thesis describes the development and correlation of a thermal model that forms the foundation of a thermal capacitance spacecraft propellant load estimator. Specific details of creating the thermal model for the diaphragm propellant tank used on NASA's Magnetospheric Multiscale spacecraft using ANSYS and the correlation process implemented are presented. The thermal model was correlated to within +/- 3 Celsius of the thermal vacuum test data, and was determined sufficient to make future propellant predictions on MMS. The model was also found to be relatively sensitive to uncertainties in applied heat flux and mass knowledge of the tank. More work is needed to improve temperature predictions in the upper hemisphere of the propellant tank where predictions were found to be 2-2.5 Celsius lower than the test data. A road map for applying the model to predict propellant loads on the actual MMS spacecraft in 2017-2018 is also presented.

THERMAL VACUUM TEST CORRELATION OF A  
ZERO PROPELLANT LOAD CASE THERMAL  
CAPACITANCE PROPELLANT GAUGING  
ANALYTICAL MODEL

by

Stephen Andrew McKim

Thesis submitted to the Faculty of the Graduate School of the  
University of Maryland, College Park in partial fulfillment  
of the requirements for the degree of  
M.S. Aerospace Engineering  
2016

Advisory Committee:

Associate Professor Christopher Cadou, Chair/Advisor

Associate Professor Raymond Sedwick

Associate Professor Bao Yang

This work was prepared as part of my official duties as an employee of the U.S. Government and, in accordance with 17 U.S.C. 105, is not available for copyright protection in the United States.

## Dedication

To my parents, who always stand behind and support me in all my endeavors.

# Table of Contents

List of Tables	vi
List of Figures	viii
List of Abbreviations	x
1 Introduction	1
1.1 Scope	2
1.2 Motivation	5
1.3 Thesis Objective	8
1.4 Acceptance Criterion	9
1.5 Previous Work	10
1.5.1 Overview of Spacecraft Propellant Gauging Methods	10
1.5.1.1 Book Keeping Method	11
1.5.1.2 Pressure-Volume-Temperature	15
1.5.1.3 Thermal Capacitance Methods	22
1.5.2 Applications of the Thermal Capacitance Method	25
1.6 Overall Approach to TCM Model Development	28
1.6.1 TCM Phase I	29
1.6.2 TCM Phase II	30
1.6.3 TCM Phase III	30
1.7 Structure of the Thesis	31
2 TCM: Theory and Application	32
2.1 Thermal Capacitance Gauging Concept & Theory	32
2.2 Implementation	34
3 Phase I: Initial Thermal Model Development and Validation	37
3.1 Description of Initial Thermal Model	38
3.1.1 Analytical & Solid Model Description	38
3.1.2 Mesh	39
3.1.3 Assumptions	40
3.1.4 Material Properties	41

3.1.5	Boundary Conditions . . . . .	42
3.1.6	Test Cases . . . . .	43
3.2	Model Validation . . . . .	43
3.2.1	Hand Calculations . . . . .	44
3.2.2	Spreadsheet Calculations . . . . .	44
3.2.3	Thermal Desktop Verification . . . . .	45
3.3	Thermal Model Results . . . . .	46
3.4	Preliminary Error Estimation . . . . .	47
4	Phase II: ANSYS Correlation Model Development . . . . .	49
4.1	Thermal Vacuum Test Overview . . . . .	49
4.2	Model Development . . . . .	51
4.2.1	Description of Tank System . . . . .	51
4.2.2	Assumptions . . . . .	54
4.2.3	Material Properties . . . . .	66
4.2.3.1	Mass of Parts & Mass Smearing . . . . .	67
4.2.3.2	Effective Thermal Conductivity of Grouped Parts . . . . .	69
4.3	Initial & Boundary Conditions . . . . .	72
4.3.1	Temperature Boundary Conditions . . . . .	73
4.3.2	Radiation Boundary Conditions . . . . .	74
4.3.3	Heat Flux Boundary Conditions . . . . .	76
4.4	Sensor Locations and Test Data . . . . .	79
4.5	ANSYS Model Details . . . . .	79
4.5.1	Model De-Featuring . . . . .	80
4.5.2	Meshing . . . . .	82
4.5.3	Locations to Query Results . . . . .	85
4.6	Model Correlation Process . . . . .	87
4.6.1	Overview & Approach . . . . .	87
4.6.2	Conductance Study Results . . . . .	89
4.6.2.1	Lower Strut Tab Interface Conductance Study . . . . .	90
4.6.2.2	Boomerang Conductance Study . . . . .	93
4.6.2.3	Upper Strut End Conductance Study . . . . .	97
4.6.2.4	Final Configuration . . . . .	100
4.7	Final Results . . . . .	102
4.7.1	Gas Side Results . . . . .	103
4.7.2	Liquid Side Results . . . . .	106
4.7.3	Discussion . . . . .	110
4.7.3.1	Gas Side Correlation Results . . . . .	110
4.7.3.2	Liquid Side Correlation Results . . . . .	114
4.8	Uncertainty Analysis . . . . .	115
4.8.1	Analysis Cases . . . . .	116
4.8.1.1	Heater Power . . . . .	116
4.8.1.2	Tank Mass . . . . .	119
4.8.1.3	Temperature Boundary Conditions . . . . .	120
4.8.2	Uncertainty Analysis Results . . . . .	120

4.8.3	Discussion . . . . .	124
5	Phase III: Using the Thermal Model to Estimate EOL Propellant Load	127
5.1	Part A: Model Refinements Using Commissioning Data . . . . .	127
5.2	Part B: Mid-Mission Orbit Change Propellant Gauging . . . . .	127
5.3	Part C: End of Life Propellant Gauging . . . . .	128
5.4	Approximate Time Line . . . . .	129
6	Conclusion, Issues, Lessons Learned & Future Work	130
6.1	Thesis Conclusion . . . . .	130
6.2	Issues & Lessons Learned . . . . .	132
6.2.1	Issues . . . . .	132
6.2.1.1	Complexity of the Model . . . . .	132
6.2.1.2	Solve Time . . . . .	134
6.2.2	Lessons Learned . . . . .	135
6.3	Future Work . . . . .	138
7	Acknowledgements	144
A	Material Properties	146
B	Boundary Conditions	153
C	Sensor Location Details	156
D	Area-Weighted Average Temperature Algorithm	160
E	Mesh Sensitivity Study Results	162
E.1	Mesh Used in Analysis . . . . .	162
E.2	Refined Mesh . . . . .	163
E.3	Comparison of Mesh Results . . . . .	163
F	Model Change Log	165
	Bibliography	173

## List of Tables

1.1	Sensitivity to Pressure Sensor Uncertainty . . . . .	19
1.2	Applications of TCM to Flight Missions: 2007-2014 . . . . .	25
3.1	Phase I Mass Validation . . . . .	45
4.1	Tank Nomenclature . . . . .	54
4.2	Calculated Thermal Quantities . . . . .	59
4.3	CAD Part Density Modifications . . . . .	68
4.4	Strut Material Properties . . . . .	71
4.5	Applied Initial Conditions . . . . .	73
4.6	Radiation Boundary Condition Locations . . . . .	75
4.7	Sensor Location Nomenclature . . . . .	79
4.8	Lower Strut Tab Interface Conductance Study Results . . . . .	92
4.9	Boomerang Conductance Study Results . . . . .	95
4.10	Upper Strut End Conductance Study Results . . . . .	98
4.11	Final Conductance/Conductivity Configuration . . . . .	101
4.12	Heater Power Uncertainty Study Results . . . . .	121
4.13	Tank Mass Uncertainty Study Results . . . . .	122
4.14	Temperature Boundary Condition Uncertainty Study Results . . . . .	122
A.1	StrutCombo Material Properties . . . . .	147
A.2	TankTiCombo Material Properties . . . . .	148
A.3	Kapton Material Properties . . . . .	149
A.4	6-4 Ti Material Properties . . . . .	150
A.5	304 L Stainless Steel Material Properties . . . . .	151
A.6	AR+N2 Mix Material Properties . . . . .	152
B.1	Boundary Conditions . . . . .	154
B.2	Radiative Properties . . . . .	155
C.1	Sensor Locations . . . . .	157
E.1	Analysis Mesh Statistics . . . . .	162
E.2	Refined Mesh Statistics . . . . .	163



E.3	Comparison of Mesh Results . . . . .	164
F.1	Model Change Log . . . . .	166
F.2	Model Change Log (cont.) . . . . .	167
F.3	Model Change Log (cont.) . . . . .	168
F.4	Model Change Log (cont.) . . . . .	169
F.5	Model Change Log (cont.) . . . . .	170
F.6	Model Change Log (cont.) . . . . .	171
F.7	Model Change Log (cont.) . . . . .	172

## List of Figures

1.1	MMS Spacecraft in Launch Configuration . . . . .	3
1.2	Magnetic Reconnection Regions of Study . . . . .	4
1.3	MMS Propulsion System & Schematic . . . . .	6
1.4	Thermal Margins . . . . .	10
1.5	TRMM BKM and PVT . . . . .	14
1.6	Pressure Sensor Uncertainty of Estimated Propellant Volume . . . . .	21
1.7	Propellant Estimates Using TCM . . . . .	23
1.8	Propellant Estimator Development Road Map . . . . .	29
2.1	Effects of Mass on Temperature Increase Over Time . . . . .	33
3.1	Phase I Model Boundary Conditions . . . . .	42
3.2	Phase I Thermal Desktop Verification Results . . . . .	46
3.3	Phase I Thermal Model Results . . . . .	47
4.1	Flight Tank Configuration . . . . .	51
4.2	Tank Model Configuration & Nomenclature . . . . .	53
4.3	1-D Heat Transfer in Tank Schematic . . . . .	57
4.4	Circuit Notation . . . . .	57
4.5	Avg Tank Wall Temperature . . . . .	61
4.6	Avg Gas Temperature . . . . .	62
4.7	Heat Flow Within Tank System . . . . .	65
4.8	Installation of MMS Propellant Tank . . . . .	70
4.9	CAD Model of Tank Strut . . . . .	71
4.10	Temperature Boundary Condition Locations . . . . .	74
4.11	Radiation Boundary Condition Locations . . . . .	75
4.12	Tank Temperatures & Heater Circuit Current vs. Time . . . . .	77
4.13	Tank Heater Heat Flux vs. Time . . . . .	78
4.14	Applied Heat Flux Boundary Condition . . . . .	78
4.15	Upper Hemisphere De-Featuring Before & After . . . . .	81
4.16	Lower Hemisphere De-Featuring Before & After . . . . .	82
4.17	Tank Mesh . . . . .	83
4.18	Distribution of Mesh Thermal Error . . . . .	84

4.19	Location of As-Built and CAD Model 1-Wires . . . . .	86
4.20	Tank Lower Strut Conductance Study Locations . . . . .	91
4.21	Boomerang Conductance Study Locations . . . . .	94
4.22	Upper Right Strut Temperature Response, Rev. 45 . . . . .	96
4.23	Upper Strut End Conductance Study Locations . . . . .	97
4.24	Upper Right Strut Temperature Response, Rev. 48 . . . . .	100
4.25	Gas Thermistor (PRP_068) Results . . . . .	103
4.26	Boomerang (PRP_053) Results . . . . .	104
4.27	Upper Right Tank Strut (PRP_054) Results . . . . .	105
4.28	Liquid Thermistor (PRP_072) Results . . . . .	106
4.29	Belly Button Tab (PRP_051) Results . . . . .	107
4.30	Lower Left Tank Strut at Tab (PRP_056) Results . . . . .	108
4.31	Lower Left Tank Strut by Ring (PRP_057) Results . . . . .	109
4.32	Heater Heat Flux Distributions . . . . .	112
4.33	Initial Heater Heat Flux Distribution . . . . .	113
4.34	Sensitivity Coefficients . . . . .	123
4.35	Uncertainty Analysis Percent Deviation Results . . . . .	124
5.1	Phase III Time Line . . . . .	129
6.1	Effect of Temperature Gradient on Query Locations . . . . .	137
6.2	Newton's Method . . . . .	141
C.1	Gas Side Sensor Locations . . . . .	158
C.2	Liquid Side Sensor Locations . . . . .	158
C.3	Liquid Side Sensor Locations (cont.) . . . . .	159
E.1	Original Mesh & Thermal Error . . . . .	162
E.2	Refined Mesh & Thermal Error . . . . .	163

## List of Abbreviations

$(P_p)_f$	Pressurant tank pressure after re-pressurization
$(P_u)_f$	Propellant tank pressure after re-pressurization
$\alpha$	Thermal diffusivity
$\beta$	Gas thermal expansion coefficient, $\beta = \frac{1}{T_\infty}$
$\Delta \mathbf{q}$	Change in heat flux
$\Delta m$	Difference in masses
$\Delta P_p$	Pressurant tank pressure decrease due to re-pressurization
$\Delta P_u$	Propellant tank pressure increase due to re-pressurization
$\Delta P_{nom}$	Difference in parameter from nominal value
$\Delta T_{nom}$	Difference of temperature from nominal temperature
$\dot{m}$	Mass Flow Rate
$\dot{m}$	Mass Flow Rate
$\dot{Q}$	Rate of heat input or loss
$\dot{Q}_{in}$	Heat into system
$\dot{Q}_{in}(t)$	Known heat input over time
$\dot{Q}_{loss}$	Heat out of system
$\dot{Q}_{loss}(T)$	Heat losses to the environment
$\epsilon$	Emissivity
$\frac{dV_p}{dP_p}$	Pressurant tank stretch coefficient
$\frac{dV_T}{dP_u}$	Propellant tank stretch coefficient
$\frac{U_q}{q_g}$	Uncertainty in gas side heat flux, $q_g$

$\mathbf{q}^a$	Average heat flux at each node
$\mathbf{q}^i$	Direction of heat flux at each node (vector)
$\mathcal{F}$	View factor
$\mu$	Dynamic viscosity
$\nu$	Kinematic viscosity
$\psi$	Ratio of volumetric heat capacities
$\rho_p$	Density of propellant
$\sigma$	Stefan-Boltzmann constant
$A$	Cross-sectional area
$A_{upper}$	Surface area of upper tank
$c$	Heat capacity
$C_a$	Convergence acceptance criterion
$C_p$	Specific heat at constant pressure
$C_s$	Sensitivity Coefficient, $\frac{\Delta T_{nom}}{\Delta P_{nom}}$
$dI$	Error in current measurement
$dR_g$	Error in gas heater resistance measurement
$dR_L$	Error in liquid heater resistance measurement
$dR_{worst}$	Worst case accuracy of Ohm meter
$e$	Thermal error
$e_i$	Error per element
$e_{bit}$	Bit error
$F$	Thrust
$FS$	Full Scale
$g$	Acceleration of gravity
$Gr_L$	Grashof Number for vertical flat plates
$h$	Convective heat transfer coefficient
$h_{gas}$	Convective heat transfer coefficient of pressurant gas

$I$	Current
$i_c$	Current of heater circuit
$I_{sp}$	Specific Impulse
$k$	Material conductivity
$k_{adh}$	Thermal conductivity of adhesive
$k_{Ti}$	Thermal conductivity of titanium
$L$	Length
$m$	Mass
$m_{actual}$	Measured mass of part(s)
$M_{CAD,Lower}$	Mass of part(s) from CAD program, lower tank hemisphere
$M_{CAD,Upper}$	Mass of part(s) from CAD program, upper tank hemisphere
$m_{model}$	Mass of part(s) in model
$m_p$	Mass of propellant
$MR_{CAD}$	Mass ratio from CAD program
$MR_{Mod}$	Modified mass ratio
$N$	Total number of
$n_{init}$	Initial number of Moles
$n_{leak}$	Number moles lost due to leakage
$Nu$	Nussult Number
$P$	Pressure
$Pr$	Prandtl Number
$q$	Heat transfer rate per unit area
$q_g$	Heat flux into gas side of tank
$Q_{cond}$	Heat transfer due to conduction
$Q_{gen}$	Heat generated
$Q_{heaters}$	Heat from tank heaters
$Q_{rad}$	Heat transfer due to radiation

$Q_{stored}$	Heat stored
$q_{upper}$	Heat per unit area into upper tank
$R$	Universal gas constant
$R_k$	Thermal Resistance parameter, current value
$R_L$	Resistance of liquid heater
$R_{adh}$	Thermal resistance of adhesive
$R_c$	Resistance of heater circuit
$R_{gasE}$	Equivalent electrical resistance of gas heaters
$R_{gas}$	Thermal resistance of pressurant gas
$R_g$	Resistance of gas heater
$R_{htr}$	Resistance of heater
$R_{k+1}$	Thermal Resistance parameter, updated value
$R_{Ti}$	Thermal resistance of titanium
$Ra$	Rayleigh Number
$T$	Temperature
$t$	Time
$T_\infty$	Free stream or quiescent temperature
$T_i$	Temperature of $i$ th surface
$T_j$	Temperature of $j$ th surface
$T_p$	Pressurant tank temperature
$T_u$	Propellant tank temperature
$T_w$	Temperature at wall
$T_{envr}$	Temperature of the environment
$t_m$	Maneuver time
$T_{tank}$	Temperature of the tank
$U$	Thermal Conductance
$U_{i_c}$	Uncertainty in full circuit current

$U_{R_g}$	Uncertainty in equivalent gas circuit resistance
$U_{R_L}$	Uncertainty in equivalent liquid circuit resistance
$V_g$	Volume of pressurant gas
$V_L$	Estimated mean propellant volume present
$V_p$	Pressurant tank volume
$V_T$	Propellant tank volume
$V_c$	Voltage of heater circuit
$V_{elem}$	Volume of element
$V_{prop}$	Volume of propellant
$x$	Horizontal position
$x_{adh}$	Length of adhesive
$X_{mod}$	Amount of mass added to lower hemisphere mass
$x_{Ti}$	Length of titanium
$Y_{mod}$	Amount of mass added to upper hemisphere mass
ACS	Attitude Control System
BKM	Book Keeping Method
BOL	Beginning of Life
CAD	Computer Aided Design
CFD	Computational Fluid Dynamics
CMF	Conductivity Multiplication Factor
EOL	End of Life
EPDM	Ethylene Propylene Diene Monomer
EPR	Ethylene Propylene Rubber
FA	Flight Acceptance
FE	Finite Element
GPS	Global Positioning System
JPL	Jet Propulsion Laboratory



MMH Monomethylhydrazine  
MMS Magnetospheric Multiscale  
NASA National Aeronautics and Space Administration  
NTO Nitrogen Tetroxide  
PMD Propellant Management Device  
PVT Pressure-Volume-Temperature Method  
Rev Model Revision  
RPG Rapid Propellant Gauging  
TCC Thermal Contact Conductance,  $\frac{W}{m^2K}$   
TCM Thermal Capacitance Method  
TRMM Tropical Rainfall Measurement Mission  
TSF Thrust Scale Factor  
TVAC Thermal Vacuum

## Chapter 1: Introduction

Knowledge of the amount of propellant contained within a spacecraft's propulsion system is essential in determining the effective operating life of the spacecraft in orbit. Since the cost of developing and launching a satellite can exceed hundreds of millions of dollars, operating the spacecraft for as long as possible is critical for commercial companies to see returns on their investments and government agencies to wisely use taxpayer dollars.

The instrumentation integrated within the propulsion system is typically limited to measurements of temperature and pressure, which do not directly measure the amount of propellant in the tank. This means that alternate methods must be developed to indirectly gauge propellant. The propellant estimates made by these gauging methods, as well as the level of uncertainty in those estimates, become an important parameter in ascertaining how long the spacecraft can continue to operate, and ultimately how long it can return usable data to its users. NASA's Magnetospheric Multiscale (MMS) Mission is an example of four spacecraft that will rely on such indirect means to determine the amount of propellant left in each propulsion system, and has unique mission requirements that require these propellant estimates to have the lowest uncertainty possible.

## 1.1 Scope

The Magnetospheric Multiscale (MMS) Mission seeks to understand the fundamental process of how magnetic fields within charged plasmas connect and disconnect in a process known as magnetic reconnection. Magnetic reconnection is a fundamental process within nature and is a main driver in the severity of space weather generated by the interaction of solar wind and Earth's magnetosphere. Space weather events can impact GPS, communication and weather satellites, as well as terrestrial power grids and distribution systems.

The fundamental mechanisms of magnetic reconnection are not well understood by scientists. A group of four, identically instrumented spacecraft (Figure 1.1) [1] were built at NASA Goddard Space Flight Center to help scientists study the phenomenon and determine its fundamental mechanisms. These spacecraft, launched in March 2015, fly in a closely spaced (10 km) tetrahedral pyramid formation that allows the instruments to capture both the three dimensional and temporal structure of the magnetic reconnection phenomenon [2]. In the first general stage of the mission, the MMS constellation will study magnetic reconnection in the magnetopause region of space which lies between the Earth and the Sun (see Figure 1.2) [3]. In the second stage, the constellation will change its orbit to study magnetic reconnection in the magnetotail region of space. These orbit changes will be accomplished by using a propulsion system.

Each of the four MMS spacecraft is equipped with a mono-propellant blow-down propulsion system, a sketch of which is shown in Figure 1.3(a) and schemat-



Figure 1.1: Photograph of the MMS Observatories in their stacked configuration for launch. Each Observatory is identical. (Image from [1])

ically shown in Figure 1.3(b) [4]. A blowdown propulsion system operates by expelling propellant from a pressurized tank through a thruster valve. The propellant tank(s) are not re-pressurized during the mission, so the pressure in the tank gradually decreases as propellant is expelled through the thrusters. This occurs until there is either insufficient pressure to force the propellant out of the tank or all propellant has been expelled. A blowdown propulsion system differs from a regulated propulsion system, in which the pressure in the propellant tank is maintained by a

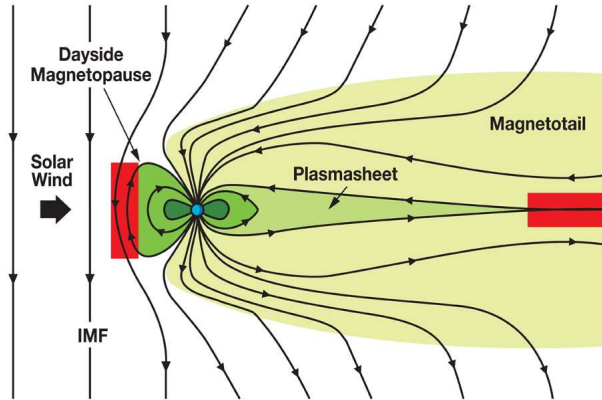


Figure 1.2: MMS will study Magnetic Reconnection in the magnetopause and magnetotail (red boxes). (Image from [3])

high pressure source which is reduced through a pressure regulation device.

A mono-propellant propulsion system carries only one type of propellant, which is anhydrous hydrazine ( $N_2H_4$ ). Thrust is produced by decomposing the hydrazine into hot  $N_2$  and  $H_2$  over a catalyst bed within the thruster. The hot decomposition products are accelerated out of the nozzle producing thrust. A mono-propellant propulsion system differs from a bi-propellant system, in which both a fuel and an oxidizer, such as nitrogen tetroxide (NTO), are used to generate thrust. When the fuel, which is typically monomethylhydrazine (MMH), is mixed with NTO, a hypergolic reaction occurs producing hot decomposition products which are accelerated out of the thruster nozzle producing thrust. The hypergolic nature of the reaction means that fuel and oxidizer must be kept in separate tanks and conveyed to the thrusters using completely separate tubing systems. These factors make mono-propellant propulsion systems less complex than bi-propellant systems.

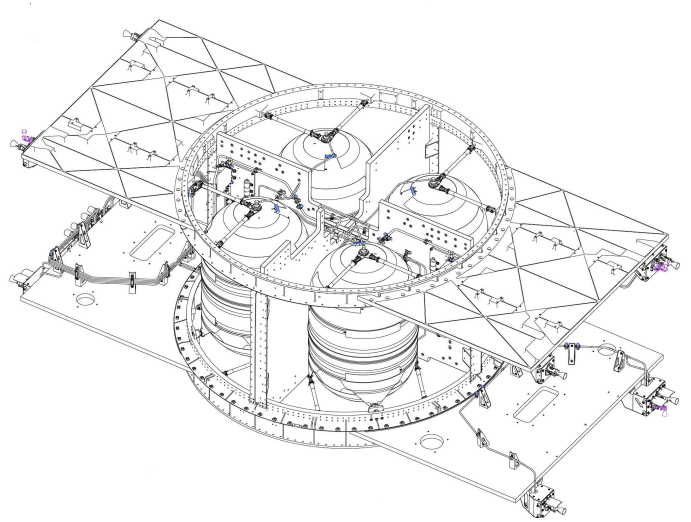
The mono-propellant blowdown propulsion system in MMS enables the four spacecraft to maintain their formation and orbit to study the magnetic reconnection phenomenon. Each propulsion system carries approximately 400 kg of hydrazine propellant and utilizes 12 thrusters. Propellant flow from the four propellant tanks are controlled via a series of latch valves, and propellant tank pressure is monitored by two pressure transducers (see Figure 1.3(b)). Tank temperatures are monitored by two thermistors, each one located on the top and bottom of the tank.

The propellant tanks utilized on MMS are diaphragm tanks. The pressurant gas and propellant are separated by a flexible membrane that is made of a polymeric material. As propellant is expelled from the tank, the diaphragm moves toward the tank outlet. This contrasts with tanks that use a propellant management device (PMD). A PMD is a series of metal structures that convey propellant to the tank outlet using the surface tension properties of the fluid. There is no separation between gas and propellant within a PMD tank, so the two are allowed to mix.

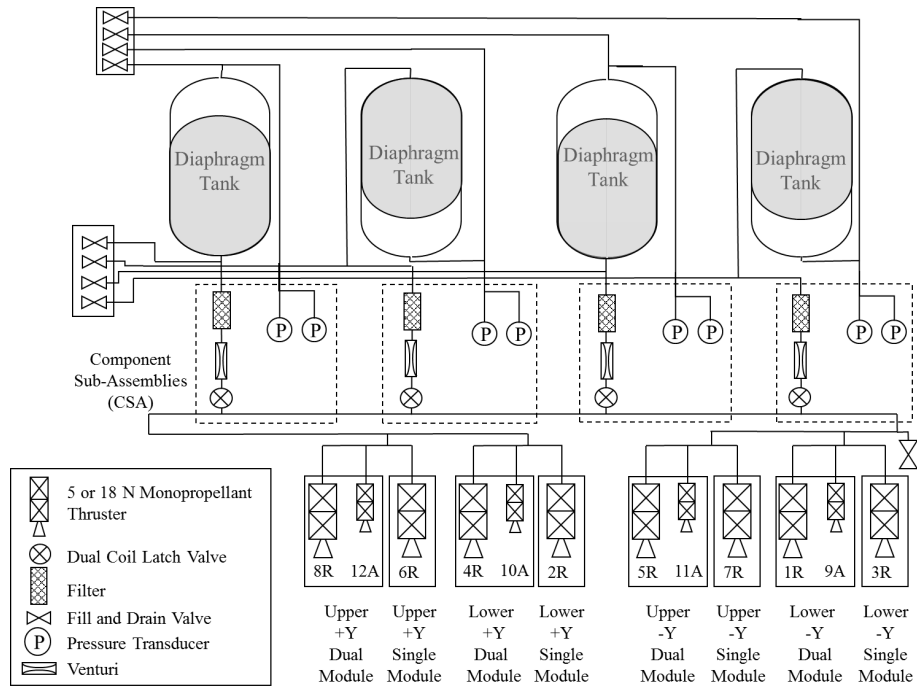
## 1.2 Motivation

Knowledge of propellant load in each of the MMS spacecraft is critical for maintaining both the tight formation of the spacecraft constellation, as well as performing the orbit changing maneuver mid-way through the mission to study magnetic reconnection in the magnetotail region.

If any of the spacecraft runs too low on propellant, the ability to maintain the proper spacing in the formation is degraded, which in turn negatively impacts



(a) Propulsion System Isometric View (Image from [4])



(b) Propulsion System Schematic

Figure 1.3: Drawing of MMS propulsion system and fluid schematic.

the observations of magnetic reconnection. Since the mid-mission orbit change will consume approximately half of the propellant, accurate knowledge of the propellant after to the orbit change is essential to determining how much mission time is left to study the magnetotail region on the opposite side of Earth. Accurate estimation of propellant load towards the End of Life (EOL) is also critical to determine how long the MMS constellation can continue returning usable science data, as well as assuring that the constellation can safely be decommissioned in order to generate minimal orbital debris or not become a hazard to other spacecraft.

Since knowledge of propellant is critical at all stages of the MMS mission, having a means by which to determine propellant loads with low uncertainty is critical to not only the general operation of the MMS spacecraft but also in enabling MMS to meet its own scientific objectives. This motivates the need to develop a propellant estimator which can determine propellant with low levels of uncertainty. The use of a thermal capacitance propellant gauging method (TCM), which relies only on the temperature response of the propellant tank to a known thermal load, enables low-uncertainty—and thus more accurate—estimates of the propellant load in a spacecraft [5]. These estimates are independent of other common propellant gauging methods, such as Book Keeping and Pressure-Volume-Temperature, that rely on temperature and/or pressure.



### 1.3 Thesis Objective

The primary objective of this thesis is to develop a thermal model of the MMS propellant tank and validate it with thermal vacuum data such that it may be later used to make predictions of propellant load in the MMS spacecraft. The validated model is the key component of the propellant load estimator to be created and refined in TCM Phase III (see Chapter 5). A broader, secondary objective is to provide a clear explanation of how to create a thermal capacitance model that will enable the propulsion and spacecraft operator community to understand how the thermal capacitance method works and develop TCM tools of their own.

This thesis also seeks to provide specifics on how to model and create a TCM propellant estimator for diaphragm-style propellant tanks like those used on the MMS spacecraft. This is important because the literature (Section 1.5.2) available on thermal capacitance methods pertains almost exclusively to tanks with propellant management devices (PMDs). Since propellant is allowed to freely move around inside of a PMD tank, some level of CFD must be completed to determine the location of the propellant in the tank and the associated heat transfer to the tank wall. This makes thermal capacitance models much more complicated to build and implement. Diaphragm tanks force propellant to one end of the tank where its location is known, making them easier to model. As of this writing, no known published literature exists on TCM implementations with diaphragm tanks.

Finally, this thesis also seeks to uncover the details of implementing the TCM in order to make it more accessible to the propulsion community. A large majority

of the published work on implementing TCM (see Section 1.5.2) is vague and lacks details that are necessary to easily develop and implement the method.

## 1.4 Acceptance Criterion

The primary objective of correlating the MMS tank thermal model with thermal vacuum test data will be considered met when the output of the thermal model is within  $\pm 3^{\circ}\text{C}$  of the thermal vacuum test data at each corresponding sensor location. This criterion, or goal, for thermal model correlation with test data is considered an industry baseline. The criterion is documented in the Spacecraft Thermal Control Handbook, Vol. 1, which is the industry standard reference for thermal design, modeling and testing practices [6]. The  $\pm 3^{\circ}\text{C}$  criterion has also been used by thermal analysts in the Thermal Branch at NASA's Goddard Space Flight Center.

The criterion is reasonable since it provides a tolerance around actual measured test temperatures that accounts for a number of unknowns that are inherent to both testing and modeling. The criterion is also well within the flight acceptance (FA) thermal reliability margin of  $\pm 5^{\circ}\text{C}$ , which is typically used by NASA for acceptance testing of flight hardware [7]. Figure 1.4, based on descriptions from [7], illustrates the typical thermal margins applied to NASA and JPL programs, including the FA thermal reliability margin.

A model correlated to  $\pm 3^{\circ}\text{C}$  assures that any over- or under-predictions by the model will not pose undue risk to flight hardware. The criterion is not so tight

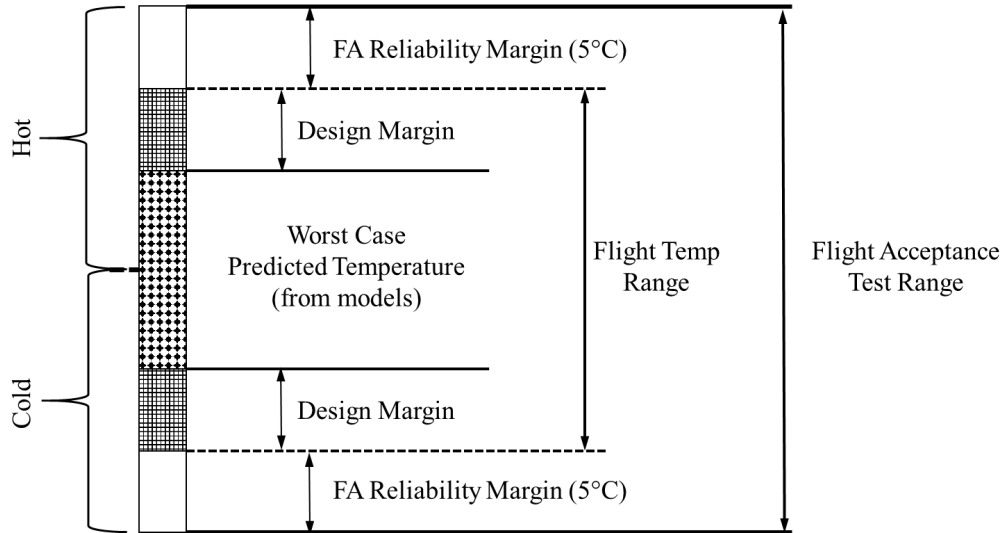


Figure 1.4: Thermal margins for JPL/NASA missions from Gilmore. The  $\pm 3^{\circ}\text{C}$  model validation acceptance criterion fits within the  $\pm 5^{\circ}\text{C}$  FA thermal reliability margin shown. (Data from [7])

that the thermal model has to be overly detailed to capture every aspect of the physical system, but is not too large such that the uncertainty of the model is so high that it is not useful for predicting temperatures.

## 1.5 Previous Work

### 1.5.1 Overview of Spacecraft Propellant Gauging Methods

Propellant gauging on spacecraft has historically been accomplished by utilizing one or a combination of three main methods: Book Keeping (BKM), Pressure-Volume-Temperature (PVT) and Thermal Capacitance (TCM). Each of these methods has their own advantages, disadvantages and levels of uncertainty associated with estimating the remaining amount of propellant contained in the spacecraft's

propellant tanks.

The goal of all propellant gauging methods is to estimate the amount of propellant remaining within the propellant tanks to the smallest level of uncertainty as possible. Less uncertainty in the propellant estimation means that spacecraft operators can potentially continue mission operations longer, increasing the amount of time scientists can obtain data from their instruments on the spacecraft. Reduced uncertainty also means that operators have better knowledge about the amount of propellant left to safely decommission the spacecraft.

Decommissioning is accomplished by either placing the spacecraft into an orbit that will pose little risk to other spacecraft, or purposely re-entering the spacecraft into Earth's or another planet's atmosphere so the spacecraft can demise. In the latter method, propellant estimates with little uncertainty are critical to ensure that the safety of both the general population and property is maintained.

#### 1.5.1.1 Book Keeping Method

The Book Keeping Method (BKM) involves tracking propellant mass based upon the known (from ground test) thruster performance associated with each maneuver performed. Book keeping, like PVT, is one of the simpler methods to estimate propellant load. The method primarily relies upon accurate knowledge of how a thruster performs and the pressure of the tank. Knowing how much thrust is produced and the associated specific impulse ( $I_{sp}$ ) at a given thruster inlet pressure

allows for the mass flow rate to be calculated per Eq. 1.1.

$$\dot{m} = \frac{F}{I_{sp}} \quad (1.1)$$

Combing this relation with the known duration of each burn allows for the total propellant mass consumed per maneuver to be calculated (Eq. 1.2). This amount of propellant is tabulated for each maneuver until end of life (EOL).

$$m_p = \dot{m}t_m \quad (1.2)$$

The thrust and Isp of a given thruster is primarily determined using models that are correlated to thruster acceptance test data. These models relate the thruster inlet pressure to both thrust and specific impulse. The pressure within the propulsion system, however, is typically only measured at the propellant tank(s). This means that a pressure drop model of the propulsion system must be used to determine the pressure at the thruster inlet. This model is correlated with flow vs. pressure drop data gathered during ground testing of each major component within the system (such as filters, latch valves, venturis, etc.). Once the pressure drop model has been made and correlated, an analytical equation relating tank pressure to thruster inlet pressure is found and then used to determine the thruster performance at any given measured tank pressure.

The BKM has a small uncertainty or error in propellant estimates at Beginning of Life (BOL) due to the fact that fewer completed maneuvers limits the build-up of estimation error. However, as the mission progresses and more maneuvers are performed, these errors compound, ultimately resulting in EOL propellant estimates

that are typically much different from actuals. Estimates of BKM error at EOL have been reported in the literature to be as low as 5% [8] to as high as 76% [9].

These estimates come from comparing the estimated propellant load using BKM with an estimate of propellant load determined from expelling all of the remaining propellant and pressure from the spacecraft propulsion system during the final phase of spacecraft decommissioning. One method involves pulsing thrusters on a single axis until the tank pressure sensors read 0 psia pressure. As the thrusters are pulsed, the angular rate of the spacecraft is sensed using a gyro or other rate-sensing device. Knowing the lever arm between the spacecraft center of mass and where the thruster is mounted, the thruster force can be determined. Once all propellant has been expelled, the magnitude of the angular acceleration will go to zero. The number of pulses to deplete all of the propellant and associated thruster force per pulse are tabulated, which in turn allows for the amount expelled propellant to be estimated [10].

BKM and PVT estimates tend to bracket the true propellant load, with BKM tending to over-estimate the remaining mass and PVT underestimating the mass. This is shown in Figure 1.5, which illustrates the estimated percent of propellant remaining within NASA's Tropical Rainfall Measurement Mission (TRMM) propellant tanks versus the maneuver number relative to the start of blowdown operation after the transition from regulated pressure operation [11].

The wide range of BKM estimation errors can be partially explained by the degradation of component performance over time, particularly filters, thrusters and pressure transducers. Filter performance typically changes over time as it entrains

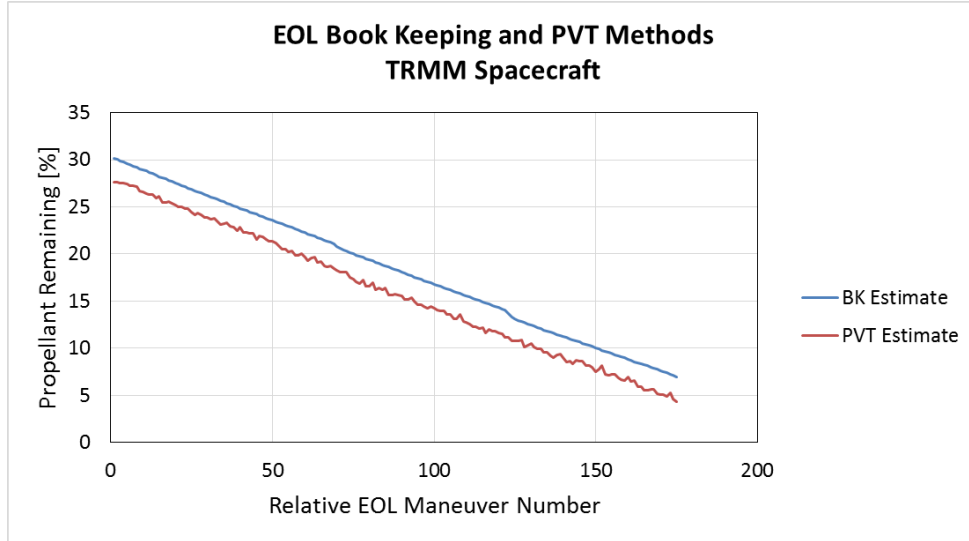


Figure 1.5: Book Keeping (blue line) and PVT (orange line) estimates for NASA’s TRMM spacecraft. Book keeping tends to estimate larger amounts of remaining propellant than predictions made by PVT. The maneuver number is relative to the start of blowdown operation of the propulsion system. (Image adapted from [11])

more particulate, increasing the pressure drop. This reduces thruster inlet pressure and therefore thruster performance. Such effects can also invalidate the pressure drop models developed prior to the launch of the spacecraft.

As an example, the pressure drop model developed prior to the mission typically does account for increases in filter pressure drop based upon worst-case particulate loads within the filter. However, the actual amount of particulate buildup within the filter (or any other part of the propellant feed system), and the effect that buildup has on component performance, is not precisely known over the life of the mission. This means that the correlation between tank pressure and thruster inlet pressure predicted on the ground by the pressure drop model will deviate from the actual relation between tank and thruster inlet pressure on the actual propulsion

system after years of operation.

Pressure transducers—particularly those exposed to large amounts of radiation as typically found in geostationary orbits—can experience significant drift and bit errors due to degraded electrical components. These factors and others act in combination over the life of a mission to change the thruster performance in ways that are not always captured in the underlying models that the BKM relies upon.

More sophisticated book keeping techniques have been developed by spacecraft operators to reduce errors in the EOL propellant estimates. One technique employs a Thrust Scale Factor (TSF) [12]. Applied before and after each maneuver, the TSF acts as a learning variable that tries to better estimate the actual thruster performance post-maneuver based upon pre- and post- maneuver variables that are measured independently of pressure and modeled thruster performance. The TSF corrects for differences in thruster performance from maneuver to maneuver based upon the predicted and actual final semi-major axis of the spacecraft orbit. This method was employed on TRMM, with uncertainty estimates that were marginally lower than those from other book keeping predictions [11]. However, the estimates still had large uncertainties in remaining propellant [11].

#### 1.5.1.2 Pressure-Volume-Temperature

The Pressure-Volume-Temperature (PVT) method involves estimating propellant mass by calculating the volume of propellant—and therefore mass—remaining in the tank based upon the measured tank temperature and pressure. Like BKM,



the PVT method is accurate at BOL and is simple to implement because it does not require overly complicated models. The PVT method relies upon knowledge of five key parameters: the mass of propellant initially loaded, the volume and expansion—or “stretching”—of the propellant tank(s), the tank pressure, and the tank temperature.

The mass of propellant remaining within the tank is determined from measuring tank temperature and pressure using temperature sensors installed on and pressure transducers plumbed inline with the tank. The mass of propellant is found from calculating the volume of propellant within the tank. The propellant volume remaining in the tank is determined from Eq. 1.3, where  $V_T$  is the volume of the propellant tank and  $V_g$  is the volume of the pressurant gas. The volume of the tank is a function of pressure and temperature since the physical tank expands or contracts (i.e. “stretching”) as temperature or pressure changes within the tank.

$$V_{prop} = V_T(P, T) - V_g(P, T) \quad (1.3)$$

The volume of the gas (or ullage volume) is determined using an ideal or real equation of state (Eq. 1.4) and is also a function of pressure and temperature. The leak rate,  $n_{leak}$ , is typically taken as the worst-case leakage rate of the propulsion system over the life of the mission.

$$PV_g = (n_{init} - n_{leak})RT \quad (1.4)$$

Multiplying by the propellant density approximated at the temperature of the propellant tank gives the remaining propellant mass (Eq. 1.5).

$$m_p = \rho_p(T)V_{prop} \quad (1.5)$$

Unlike the BKM, where errors compound from maneuver to maneuver, the PVT method provides propellant estimates that are independent of previous maneuvers and typically produces lower estimates of remaining propellant, as shown in Figure 1.5 [11].

The PVT method produces propellant estimates with lower uncertainty at BOL because the propellant tank exhibits a larger change in pressure as the propellant is expelled. At EOL, the change in propellant tank pressure is small compared to the amount of propellant expelled. This leads to greater uncertainties in propellant estimates. Estimate uncertainties are further compounded by degradation of the pressure transducer electronics caused by radiation accumulated over the life of the mission.

Contributors to the overall error in PVT are from uncertainties in propellant tank volume and stretch, temperature and pressure measurements from the pressure transducer. The effect of the uncertainty in each of these parameters on the calculation of the amount of propellant volume remaining in the tank was studied using statistical and Monte Carlo methods by Lal and Raghunandan [13]. The authors ultimately found that uncertainty in tank pressure measurements were the single largest cause of errors in propellant estimates made by the PVT method.

The statistical analysis conducted by Lal and Raghunandan was based on from propellant estimation methods developed by Chobotov and Purohit [14], in which remaining propellant was estimated by re-pressurizing propellant tanks using high pressure storage tanks. As the low pressure propellant tanks were re-pressurized, the tanks physically deformed a small amount, changing their volumes. At the same

time, the high pressure tanks also deformed, contracting slightly as the pressure within them decreased. Chobotov and Purohit developed an equation (Eq. 1.6) to estimate the propellant volume ( $V_L$ ) based upon these physical changes within the tanks, as well as the pressures and temperatures of the propellant and pressurant tanks before and after the re-pressurization.

$$V_L = \left[ V_T + (P_u)_f \left( \frac{dV_T}{dP_u} \right) \right] - \left[ V_p + (P_p)_f \left( \frac{dV_p}{dP_p} \right) \right] \left( \frac{T_u}{T_p} \right) \left( \frac{\Delta P_p}{\Delta P_u} \right) \quad (1.6)$$

Where:

$V_L$ : Estimated mean propellant volume present

$V_T$ : Propellant tank volume

$V_p$ : Pressurant tank volume

$T_u$ : Propellant tank temperature

$T_p$ : Pressurant tank temperature

$(P_u)_f$ : Propellant tank pressure after re-pressurization

$(P_p)_f$ : Pressurant tank pressure after re-pressurization

$\frac{dV_p}{dP_p}$ : Pressurant tank stretch coefficient

$\frac{dV_T}{dP_u}$ : Propellant tank stretch coefficient

$\Delta P_p$ : Pressurant tank pressure decrease due to re-pressurization

$\Delta P_u$ : Propellant tank pressure increase due to re-pressurization

It is noted by Lal and Raghunandan that Eq. 1.6 does not account for gas solubility or compressibility, and assumes adiabatic conditions, but is sufficient to study the effects of uncertainty in temperature, volume and pressure effects on the

estimated propellant volume [13].

Lal and Raghunandan used a Monte-Carlo simulation to simultaneously vary the parameters of pressure, volume, temperature and stretch for both the pressurant and propellant tanks modeled by Chobotov and Purohit to study how each affected the estimated propellant volume,  $V_L$ . The sensitivity, defined as the ratio of uncertainty in  $V_L$  to the corresponding parameter studied, was measured for each parameter [13]. This sensitivity study showed that the estimated propellant volume,  $V_L$ , was most sensitive to uncertainties in tank pressure measurements and relatively insensitive to uncertainties in temperature, volume and tank stretch (see Table 1.1 [13]).

Table 1.1: Sensitivity factor of the estimated propellant tank volume  $V_L$  to uncertainties in different parameters. The estimated propellant volume is the most sensitive to uncertainties in pressure sensor readings compared to all other parameters. (Data from [13])

<b>Parameter</b>	<b>Sensitivity</b>
Propellant tank pressure sensor	125
Pressurant tank pressure sensor	20.2
Propellant tank volume	1.84
Pressurant tank volume	0.852
Pressurant tank temperature sensor	0.854
Propellant tank temperature sensor	0.854
Pressurant tank stretch	0.0330
Propellant tank stretch	0.0120

The reason for the insensitivity to temperature was due to the fact that measured temperatures of tanks ( $T_P$ ) are typically far from zero (typical propellant tanks

are kept at 293-300 K), which means that the  $(\frac{T_u}{T_p})$  term in Eq. 1.6 will remain near unity. The insensitivity to tank stretch  $(\frac{dV_i}{dP_u})$  and  $(\frac{dV_p}{dP_p})$  is due to the fact that the tank is designed to withstand high pressures and not yield or plastically deform. Therefore, these derivatives will not tend toward large values, and remain at nearly constant values close to zero. Both uncertainties in temperature and tank stretch cause the two terms in the left-hand-side of Eq. 1.6 to vary only slightly as these quantities change, ultimately having limited impact on the estimated propellant volume.

The high sensitivity to uncertainties in pressure readings was investigated further by Lal and Raghunandan by using another Monte-Carlo simulation to investigate the change in estimated propellant volume with increasing uncertainty in pressure readings. The result of this analysis is presented in Figure 1.6 [13], which shows the estimated propellant volume ( $V_L$ ) compared to the calculated propellant volume ( $V_{L0}$ ), which was based upon measurements of all parameters. It can be seen from Figure 1.6 that an uncertainty of as little as 0.6% in the pressure transducer reading can impact the propellant volume ( $V_L$ ) estimation as much as 10%.

This high error in  $V_L$  relative to  $V_{L0}$  for such a small uncertainty in tank pressure measurement was explained by Lal and Raghunandan using primarily statistical reasoning. The parameter of propellant tank pressure increase due to re-pressurization ( $\Delta P_u$ ) and the pressure of the tank before and after the re-pressurization ( $P_{u_i}$  and  $P_{u_f}$ , respectively) are both normally distributed about their mean values. This means that as the uncertainty in the pressure measurement increases, the second term in Eq. 1.6 increases faster than the first term. This results in the estimated

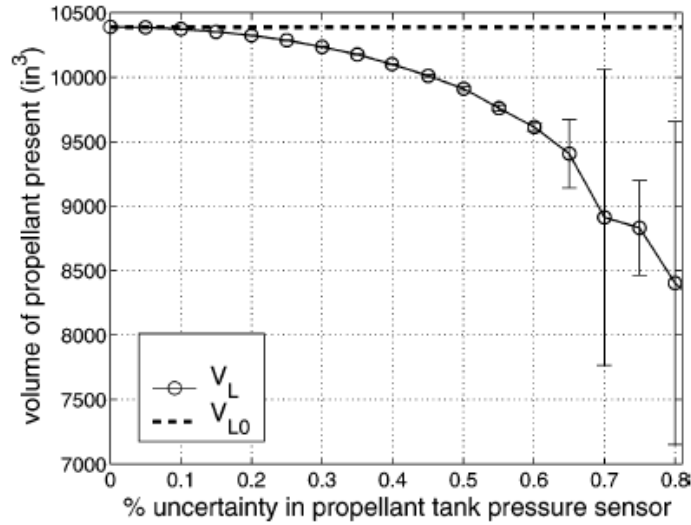


Figure 1.6: Variation of estimated propellant volume ( $V_L$ ) with uncertainty in tank pressure sensor. The estimated propellant volume  $V_L$  changes greatly from the measured volume  $V_{L0}$  with small increases in pressure transducer uncertainty. (Image adapted from [13])

propellant volume decreasing away from the measured, or true, value of propellant volume ( $V_{L0}$ ). This behavior is shown in Figure 1.6.

The higher variations in estimated propellant volume beyond an uncertainty of 0.6% (Figure 1.6, shown by error bars) were also explained by Lal and Raghunandan, who looked at the behavior of  $\Delta P_u$  in the second term of Eq. 1.6. Since the mean value of  $\Delta P_u$  is small (on the order of 1 psia), and because the term appears in the denominator, the probability of the term falling close to zero increases as the uncertainty in the tank pressure sensor measurement increases, thus causing the higher variations in estimated propellant volume [13].

The statistical explanations for increasing error due to decreasing predictions of propellant volume as uncertainties in pressure readings agree with the behav-

ior of the pressure transducers over the life of a typical mission. As the pressure transducers age, the uncertainty in readings grows due to degradation of electrical components within the transducer. This degradation is typically caused by increasing doses of radiation exposure throughout the life of the mission. The propellant estimations from the PVT method gradually diverge from those made with the BKM over the course of the mission as the uncertainty in the pressure measurements increase as the pressure transducer ages and the electronics become more degraded. The divergent estimates between BKM and PVT methods can be seen in in Figure 1.5.

### 1.5.1.3 Thermal Capacitance Methods

The Thermal Capacitance Method involves estimating propellant load by measuring the thermal response of the propellant tank to a known heat input over time,  $\dot{Q}_{in}(t)$ . A simple, lumped capacitance model of the system is given by Eq. 1.7, where  $m$  is the tank mass,  $c$  is its heat capacity,  $T$  is the temperature,  $t$  is time and  $\dot{Q}_{loss}(T)$  are losses to the environment. This model, however, is unrealistically simple. A useful predictive model needs to account for spatially varying material properties of the tank and surrounding structure, conduction between thermal interfaces, and the specific geometry of the components within the system.

$$\dot{Q}_{in}(t) - \dot{Q}_{loss}(T) = mc \frac{dT}{dt} \quad (1.7)$$

Once this sophisticated thermal model of the propellant tank(s) and surrounding structure has been created, propellant estimations are made by comparing tem-

perature vs. time curves for different propellant masses generated by the thermal model with flight data recorded from spacecraft telemetry when the tank's heaters are turned on for a period of time. The result of this process is shown in Figure 1.7, which depicts an illustrative example of how TCM would be applied to a hypothetical spacecraft. As seen in the figure, different propellant loads are simulated in the thermal model to produce different temperature vs. time curves (solid lines). Those curves are then plotted with flight data (symbols) recorded from the spacecraft tank temperature sensors during heating of the flight tank. The time axis is relative to the point when the tank heaters are turned on.

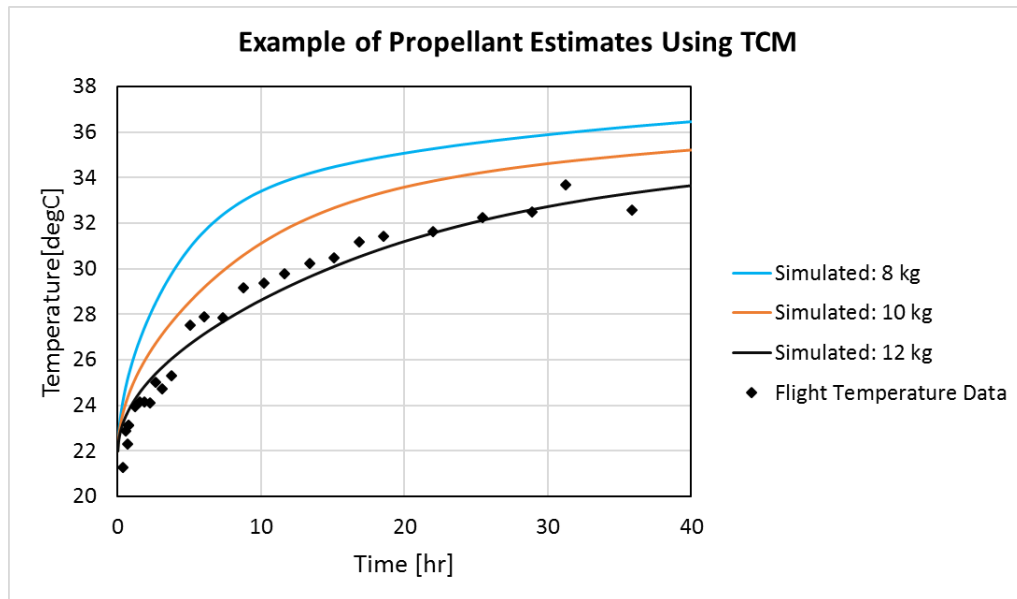


Figure 1.7: Simulated TCM results (solid lines) for different propellant masses are compared to flight telemetry values (symbols) to obtain a propellant estimate.

The simulated temperature curves are then compared with temperature data taken from the spacecraft once the tank heaters have been turned on for a period



of time to determine the propellant load in the tank. These steps have been generalized [5], and can be applied to any spacecraft that has an active heater control system.

Unlike the BKM and PVT methods described previously, the thermal capacitance method is complicated to implement since it requires a complex thermal model to make the propellant estimates. It also has greater uncertainties in propellant estimates at BOL. The advantage of TCM, however, is that uncertainties in propellant estimates decrease throughout the life of the spacecraft, reaching a minimum at EOL [5]. This reduction in uncertainty directly ties to the physics explained in Eq. 1.7.

At BOL, the large mass of propellant in the tank causes a smaller change in temperature when the tank heaters are turned on. The opposite effect occurs at EOL, where the tank temperature changes are larger because a greater volume of the tank is occupied by the less massive pressurant gas instead of the more massive propellant. More pronounced temperature changes in the tank therefore decrease the uncertainty in propellant estimates made using TCM. Because of this, estimates made by the TCM are typically much better than those made with BKM. Yendler, et al reported errors in propellant estimates made on the GEOSTAR 1 missions to be as low as 1% to as high as 11%, as compared to those taken using the BKM, which had errors that ranged between 95% to over 300% [9].

## 1.5.2 Applications of the Thermal Capacitance Method

The thermal capacitance method has been successfully implemented on a number of spacecraft over the past decade-and-a-half, although few detailed discussions have been published in the open literature. Most of the publicly available reports on TCM have been written or co-authored by Boris Yendler, CEO of YSPM, LLC, a company that specializes in TCM propellant gauging [15]. As described in papers published through AIAA, Yendler has applied TCM to a number of spacecraft and platforms, a sampling of publicly disclosed applications of which is listed in Table 1.2.

Table 1.2: Applications of TCM to Flight Missions: 2007-2014

<b>Spacecraft/System</b>	<b>Year</b>	<b>Ref.</b>
SkyPerfect (JSAT) / Boeing BSS 601 Bus	2007	[16], [17]
Telstar 11	2008	[5]
Turksat 1C / SpaceBus 2000	2008	[18]
Arabsat 2B / SpaceBus 3000A	2012	[19]
GEOSTar 1A & 1B	2013, 2014	[9], [20]

Yendler’s published work outlines the general process of implementing the TCM method and the results obtained from the different spacecraft on which it was implemented. This work documents application of TCM almost exclusively to spacecraft that use propellant tanks with propellant management devices (PMDs), rather than diaphragms or bellows. The published material also provides general descriptions of the different software tools used to implement the thermal and finite

element modeling of the propellant tank and spacecraft.

The general process as documented by Yendler to perform a TCM propellant estimation for any spacecraft has largely stayed the same since the early 2000s. That process is as follows [5], [20]:

1. Develop thermal models of the propellant tank(s) and surrounding satellite structure
2. Conduct flight tests on the spacecraft by raising the tank temperature and allowing it to cool, monitoring the temperature profiles
3. Calibrate the thermal models using the flight temperature data
4. Simulate the heating of the tank(s) in the thermal model
5. Estimate the propellant load based upon the comparison of simulated and flight data
6. Evaluate the accuracy and uncertainty of the propellant estimates

While the fundamental physics and general process for implementing the TCM have remained the same, Yendler's team and co-authors have been refining the different software tools used to implement TCM. In the mid-2000's, tank finite element models were made with a combination of different programs, focusing primarily on the propellant tank. The fluid interaction with the tank and the PMD surfaces were modeled using Surface Evolver [21], a software tool that models the shape of a fluid based upon the forces and constraints that act upon it. The tank structure and

PMD were meshed using GridPro, a CFD mesh generation tool [16], [17]. Other software tools were developed in-house by Yendler to help address meshing problems presented by complicated tank and PMD geometries, but specifics on what these tools are and how they work have not been published [16], [17].

By the 2010's, the tank and spacecraft thermal models developed by Yendler's team were made using Thermal Desktop by C&R Technologies [22]. Thermal Desktop creates a thermal model by allowing users to import a CAD representation of a device or structure. The software can model contact conductance, heat loads, and effects of insulation on that imported CAD model. Yendler's group continued to use Surface Evolver to model the liquid distribution within the PMD tank [20]. Other tools were developed including software to filter spikes in flight telemetry, remove diurnal variations of temperatures, interpret Surface Evolver results, and optimize curve fitting for simulated and flight temperature vs. time curves [20].

Yendler's team has also worked to advance the state of the art of TCM by developing a "Rapid Propellant Gauging" (RPG) technique, which provides a quick estimate of propellant load with little knowledge of the thermal configuration of the tank. The RPG accomplishes the estimation by exposing the tank to an "effective" thermal environment that mimics the "true" thermal environment around the tank [23]. Propellant estimation errors of the RPG method as applied to Orbital Sciences Corporation GEOSar 1A and 1B have been shown to range from as little as 6% to as much as 54% [9]. Further details about how the RPG method is implemented are not available in the published literature.

Despite the large volume of published work describing Yendler's implemen-

tation of TCM, the discussions are highly generalized, and critical details on how to practically implement the TCM process on a spacecraft are omitted. Examples include how to create the FE models of the tank and spacecraft, as well as how to correlate and interpret the output of the thermal system model. The specific steps and process of implementing the TCM methodology are also not described. This leaves the reader to determine those details on their own or to contract those services out of house. Therefore, an important goal of this project is to uncover the details of implementing the TCM in order to make it more accessible to the propulsion community.

## 1.6 Overall Approach to TCM Model Development

A three-phase approach is taken to develop a propellant estimator for the MMS spacecraft based on the TCM method. Each Phase has its own set of tasks and objectives that provide the foundation for the next Phase. We will see below that this thesis fits into Phase II.

Each Phase of the TCM development project corresponds to stages in the development of the MMS spacecraft as illustrated in Figure 1.8. Phase I of the TCM development was completed when the MMS spacecraft were being designed and built. Phase II was undertaken when the MMS spacecraft were finishing environmental testing until the post-launch and commissioning stage. Phase III of TCM development will occur at the end of the MMS primary mission life and continue through the EOL and decommissioning stages.

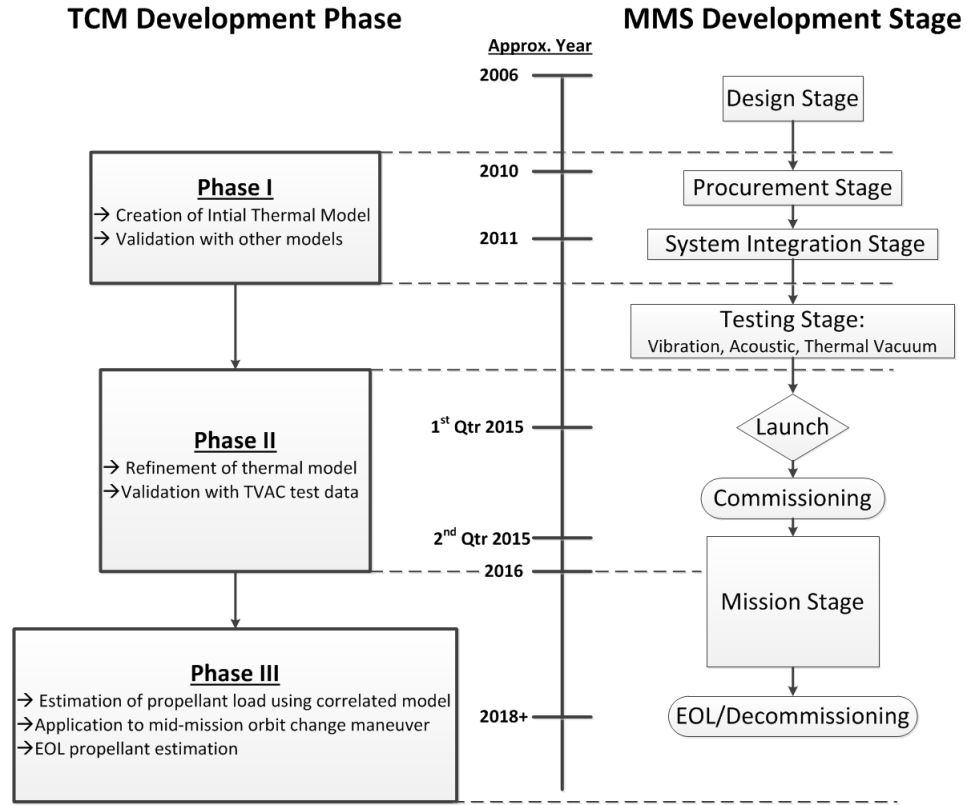


Figure 1.8: The development phases of the TCM propellant estimator roughly coincide with the development stages of the MMS Mission.

### 1.6.1 TCM Phase I

Phase I focused on developing a thermal capacitance model of the MMS propellant tank in ANSYS 13.0 [24] that was validated via comparison with other thermal models because the spacecraft was still being built and thermal vacuum testing had yet to occur. Boundary and initial conditions were assigned based upon predictions made by the MMS Thermal Subsystem’s preliminary thermal model of the spacecraft. Results from the ANSYS 13.0 model were validated by comparing output with the Thermal Subsystem model, as well as through hand and spreadsheet

calculations. Chapter 3 provides details of the Phase I development effort.

### 1.6.2 TCM Phase II

Phase II is the focus of this thesis and is described in detail in Chapter 4. The objective of Phase II is to refine the Phase I thermal model and correlate it with thermal vacuum test data. This Phase began when MMS had finished environmental testing, and continued through the Launch and Commissioning phases of MMS. Boundary and initial conditions were matched to those during the thermal vacuum test, and the model was refined such that its output matched the temperature data measured during the test.

### 1.6.3 TCM Phase III

Phase III is the final phase of the MMS TCM development, and its final outcome is a propellant load estimator that has been correlated with thermal vacuum test data and calibrated with flight data. Phase III builds on the thermal model that was developed in Phase II and is the subject of this thesis.

Phase III will encompass three main parts: calibrating the thermal model with flight data, estimating propellant after the mid-mission orbit change, and estimating propellant at the beginning of the EOL/Decommissioning phase. The estimator will be calibrated using temperature data recorded from the heating of the fully loaded propellant tanks taken during the commissioning stage of the MMS mission. The estimator will then be used to estimate propellant after the mid-mission burn, which

changes the orbit of the MMS spacecraft from one that allows observations of the magnetopause, to one that enables observation of the magnetotail (see Figure 1.2).

The next estimation will occur at the beginning of the EOL/Decommission phase (see Figure 1.8). Propellant estimates at this stage of the MMS mission will be critical to help determine how much propellant is left, which directly impacts how long the propulsion system can maintain MMS constellation and orbit, enabling useful science data to be gathered. Phase III of the project has yet to be started, and will be the subject of future work.

## 1.7 Structure of the Thesis

The structure of the remaining chapters of this thesis are as follows. Chapter 2 describes the theory and application of the TCM. Chapter 3 summarizes the work completed in development of the initial thermal model created as part of Phase I. Chapter 4 covers in extensive detail the development of a thermal model and its subsequent correlation with thermal vacuum test data as part of Phase II. Chapter 4 is the heart of this thesis. Chapter 5 summarizes the future use of the propellant estimator that makes up Phase III of the project. Finally, Chapter 6 states the conclusions made from the model creation and correlation of Phase II, and presents areas of future work.



## Chapter 2: TCM: Theory and Application

### 2.1 Thermal Capacitance Gauging Concept & Theory

The concept of estimating propellant load using thermal capacitance methods is based on the ability of matter, be it a fluid or a solid, to store thermal energy. Thermal energy storage is modeled via Eq. 2.1. This equation relates the rate of temperature change over time of a given quantity of mass to the net rate of energy input.

$$cm \frac{\partial T}{\partial t} = \dot{Q}_{in} - \dot{Q}_{loss} \quad (2.1)$$

Where:

$\dot{Q}$ : Rate of energy input or loss

$c$ : Specific heat

$m$ : Mass

$\frac{\partial T}{\partial t}$ : Time rate of change of temperature

Equation 2.1 shows that if the rate of energy input and specific heat of a given material were constant, the amount of time it would take to change the temperature of a fixed amount of matter would change as a function of the mass of the matter. This can be seen in Figure 2.1, which shows the temperature vs. time curves for a

uniform block of material of different prescribed masses. As the mass of the block increases, the amount of time required to reach equilibrium also increases for a given heat load.

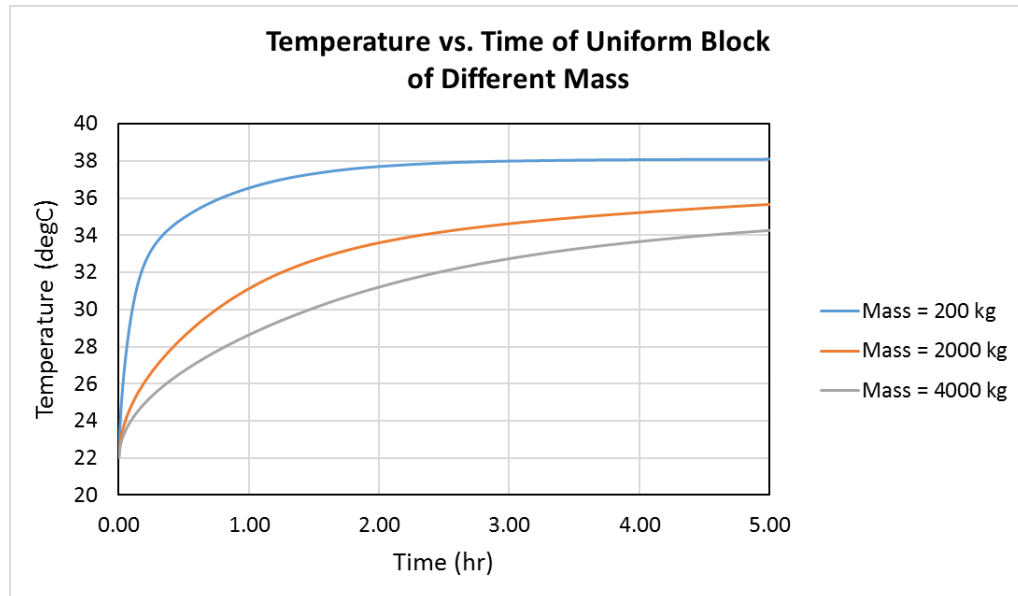


Figure 2.1: Temperature vs. time behavior for a block of different mass. The temperature rise in time decreases as the mass increases.

This concept is used to estimate the amount of propellant remaining in a tank. On orbit, the propellant tank within the spacecraft is heated by turning on the tank heaters. The temperature vs. time information from the tank's temperature sensors is recording during this heating. This curve is then compared to temperature vs. time curves that were produced using a thermal model of the tank with different propellant loads.

Heat input into the tank is provided by the tank heaters. The heat losses from the tank system are conductive and radiative. These are modeled by the Fourier

and Stefan-Boltzmann laws, respectively. Thus,

$$\dot{Q}_{in} = Q_{heaters} \quad (2.2)$$

$$\dot{Q}_{loss} = Q_{cond} + Q_{rad} \quad (2.3)$$

$$Q_{cond} = -kA \frac{dT}{dx} \quad (2.4)$$

$$Q_{rad} = \mathcal{F} \sigma A (T_i^4 - T_j^4) \quad (2.5)$$

In these expressions,  $\mathcal{F}$  is the radiation view factor. For radiation between  $i$  and  $j$  surfaces,  $\mathcal{F}$  is defined as:

$$\mathcal{F} = \frac{1}{\frac{1-\epsilon_i}{\epsilon_i A_i} + \frac{1}{A_i F_{ij}} + \frac{1-\epsilon_j}{\epsilon_j A_j}} \quad (2.6)$$

## 2.2 Implementation

Previous implementations of the TCM on a spacecraft have been accomplished by following the general process documented by Yendler (see Chapter 1, Section 1.5.2). That process is repeated here for convenience:

1. Develop thermal models of the propellant tank(s) and surrounding satellite structure
2. Conduct flight tests on the spacecraft by raising the tank temperature and allowing it to cool, monitoring the temperature profiles
3. Calibrate the thermal models using the flight temperature data
4. Simulate the heating of the tank(s) in the thermal model

5. Estimate the propellant load based upon the comparison of simulated and flight data
6. Evaluate the accuracy and uncertainty of the propellant estimates

For the project described herein, the above general process will be modified to include the validation of the model (Phase II of this project, see Chapter 4) using thermal vacuum test data (see Section 4.1) prior to conducting flight tests on the spacecraft. This step is unique since the MMS spacecraft’s usable life is short—two to three years—meaning that data taken during thermal vacuum testing will still accurately represent the spacecraft on orbit. This is because the optical properties of the materials in the spacecraft will not have degraded as much as those on spacecraft operating for decades due to the space environment, so the heat transfer within the spacecraft will still match what was tested on the ground. This will allow for a tank thermal model correlated with thermal vacuum data to more accurately model the real tank system on the operating spacecraft, leading to potentially more accurate propellant estimations.

Yendler’s process will further be modified in Phase III (see Chapter 5), since calibration of the thermal models using flight data will take place at three different points: at the beginning of life, middle of life, and end of life. At beginning of life, flight tests were conducted during commissioning of the MMS spacecraft immediately after launch, when the propellant mass was known with great accuracy. The mid-life course correction maneuver will allow for additional flight tests to be conducted when approximately half of the propellant remains. Following Step 3

noted above, calibrations of the thermal model with flight data at this point can be compared to both book keeping and PVT methods, which will still be relatively accurate. Finally, the EOL propellant gauging will allow for a final calibration with flight data to be completed. All three calibrations of the model with flight data will allow for trends in propellant estimation throughout the life of the spacecraft to be established, providing for a higher accuracy EOL propellant estimation using TCM.

## Chapter 3: Phase I: Initial Thermal Model Development and Validation

Phase I focused primarily upon developing the initial thermal model to predict the propellant load in the MMS spacecraft propellant tank. Prior to Phase I, no thermal model had been created for predicting propellant load. Therefore, the tank thermal model in Phase I was developed from scratch using ANSYS 13.0 finite element software.

Another primary goal of Phase I was to determine the process of developing a TCM, since published literature on the topic of thermal capacitance methods provided little to no detail about actually making a thermal capacitance model (see Section 1.5.2). Emphasis was placed on developing the tank thermal model.

Understanding the physics of how the model responded to different propellant loads was another major part of the effort. Since heat transfer in the space environment is mostly dominated by radiation and conduction, emphasis was placed on how these modes of heat transfer affected the tank thermal model. Convective heat transfer, which does occur within the propellant and gas parts of the tank, was therefore neglected, since this effect was of second order nature as compared to the radiative, conductive, and capacitive mechanisms that dominated the overall heat

transfer of the tank system.

Validation of the thermal model developed in ANSYS was accomplished by comparing its output with the thermal subsystem's spacecraft thermal model created in Thermal Desktop [22], as well as with basic heat transfer equations. Validation with test data was not possible during Phase I, since the MMS spacecraft thermal vacuum testing had not yet occurred.

Once the thermal model was created, temperature vs. time curves for different propellant loads were simulated. These simulations allowed for a physical understanding of how the system would react, as well as serve as a foundation for Phase II, where the thermal model would eventually be correlated with thermal vacuum test data. The following sections briefly review the work done on this previous model. Details of the effort can be found in McKim [25], [26].

### 3.1 Description of Initial Thermal Model

#### 3.1.1 Analytical & Solid Model Description

A transient thermal analysis model of the propellant tank was created in ANSYS 13.0 finite element analysis software. A transient, rather than a steady-state, analysis was necessary since the heating of the propellant tank is a function of time-varying thermal loads and temperature-varying material properties. The inclusion of radiation boundary conditions also makes the problem non-linear. The ANSYS 13.0 software provides tools that simplify solving this problem by allowing the analyst to input time-varying loads and properties. The ANSYS solver then iteratively

solves the energy equation (see Chapter 2) over discrete time steps, which results in a thermal solution at each time step within the analysis.

A Pro-Engineer solid model of the MMS propellant tank was imported into the ANSYS 13.0 solver. This tank model was highly detailed and reflected the as-designed flight configuration of the MMS propellant tank. The model included all flight and non-flight hardware integrated on the tank, such as bolts, washers, lock-wire, thermostats, 1-wire sensors, etc. The model was simplified by removing unnecessary geometry to reduce mesh complexity and save computation time. Examples of items that were removed included redundant temperature sensors, bolts, washers, and other small parts that had little effect on the overall heat transfer. Where necessary, sensors at locations necessary for analysis results were left in place.

Since a license of ANSYS, Inc.'s solid model pre-processor, Design Modeler, was not available at the time of Phase I, the solid model of the tank could only be simplified by suppressing extraneous geometry, instead of removing them. This meant that items such as bolt holes could not be filled, and problematic geometry, such as slivers, small edges, and other CAD import errors could not be removed or corrected.

### 3.1.2 Mesh

Meshing was accomplished using the integrated meshing tools within ANSYS. Suppression, rather than correction/removal of extraneous and problematic geom-



etry as described above resulted in meshing difficulties. Extraneous model detail, such as bolt holes, also increased mesh density. This denser mesh increased the number of nodes, significantly increasing solve time. Nevertheless, a sufficient mesh which reduced thermal errors was generated. The overall resulting mesh contained over 356,000 nodes.

### 3.1.3 Assumptions

Since the purpose of the Phase I model was to get an order of magnitude understanding of the system, a number of simplifying assumptions were made during the development of the tank thermal model in Phase I. The main assumptions used are listed as follows:

- Convection within the pressurant gas and propellant was neglected. This assumption was made during Phase I since it was reasoned that convection would have a negligible impact on the time constant of the system compared to the effect the far more massive propellant would have in the system. In other words, the large mass of propellant would drive the system, rather than the effect of convection within the propellant or pressurant gas. In order for the ANSYS model to close, the fluid was treated as a solid that conducts and stores heat.
- Fluid shapes were specified and did not change due to temperature effects (no migration). This assumption was made since the diaphragm is effectively non-permeable and will keep the shape of the fluids within the tank constant.

- Heater power input was constant. This approximated the nominal operation of the heaters when turned on.
- Boundary conditions were based upon the average temperature of the tank/spacecraft interface location, and assumed constant over time. This was based upon the Thermal Branch’s analysis at the time, as well as the fact that the spacecraft has an active thermal control system to maintain the temperature of key parts of the system.

### 3.1.4 Material Properties

Each part of the Pro-Engineer solid tank model was assigned its own unique material within ANSYS, which in turn was mapped to a database of material properties within the ANSYS Workbench interface. The primary materials used in the model were titanium 6Al-4V, helium, hydrazine, 304L stainless steel, and Kapton polyimide film.

Material properties were found through industry standard sources, such as the Aerospace Structural Metals Handbook and Eckart Schmidt’s “Hydrazine and its Derivatives.” Material properties not published in these sources were found using vendor-supplied material data, such as for Kapton polyimide film made by Honeywell.

### 3.1.5 Boundary Conditions

Boundary conditions of radiation, temperature and heat input were applied to the model, as shown in Figure 3.1 [25]. Radiation was applied to all tank surfaces using the effective emissivity of the tank blanket, as well as the emissivity for other materials on the tank. Temperature boundary conditions were set at the end of each of the tank's four mounting struts, and at the axial pin located at the middle-bottom of the tank.

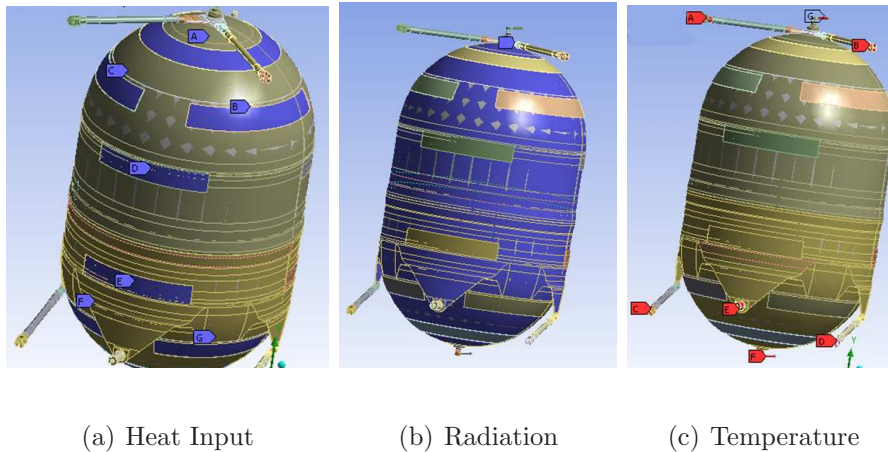


Figure 3.1: Heat input, radiation and temperature boundary conditions as applied to the Phase I thermal model. (Figure adapted from [25])

Heat input to the tank was modeled based upon the heater circuits integrated onto the flight tank. The tank contained two heater circuits, each in parallel: one on the gas side and the other on the liquid side. Each circuit is controlled by an over-temperature thermostat, which provides a safety mechanism to ensure the tank does not overheat if the heaters are powered on too long. The model did not account for thermostat operation, so both liquid and gas sides could exceed the

over-temperature thermostat set point during the simulation. Since the gas circuit exceeded the over-temperature thermostat set point early in the simulated heating period, only heat from the liquid side heaters were applied to the tank within the model. This allowed for the thermostat operation to be partially modeled.

### 3.1.6 Test Cases

Three different propellant load test cases were simulated, each of which were representative of EOL propellant load fractions that were predicted for the MMS spacecraft. The load cases were 10%, 15%, and 20% propellant loads. The thermal model for each test case was the same, but the respective volumes of the propellant and gas were updated to reflect the propellant mass simulated.

## 3.2 Model Validation

The Phase I ANSYS thermal model was validated using analytical methods and by comparison with other thermal model programs since test data did not exist. Three means of verification were employed: hand calculations, spreadsheet calculations to numerically validate the ANSYS output, and validation with output from Thermal Desktop.

### 3.2.1 Hand Calculations

Basic 1D heat transfer equations for conduction (Eq. 3.1) and radiation (Eq. 3.2) were used to spot check the output from the Phase I ANSYS thermal model.

$$Q = \frac{kA}{L} (T_2 - T_1) \quad (3.1)$$

$$Q = A\epsilon\sigma (T_{tank}^4 - T_{envr}^4) \quad (3.2)$$

Verification calculations focused on the main routes of heat loss due to conduction and radiation. These routes were conductive losses through the struts and radiative losses from the tank wall. Results from hand calculations using Eq 3.1 and Eq. 3.2 compared well with the ANSYS output. For conductive losses on the struts, hand calculations were within 4% of the ANSYS model. For radiative losses from the tank, hand calculations were with 2% of the ANSYS model [25].

### 3.2.2 Spreadsheet Calculations

Spreadsheet calculations were preformed to numerically verify that the ANSYS model was following the conservation of energy. This verification was accomplished by calculating propellant mass via Eq. 2.1 for each time step of the ANSYS simulation. The  $\frac{dT}{dt}$  derivative used in Eq. 2.1 was found from the temperature output from ANSYS at each time step via a 3-point centered difference equation [25]. Mass vs. time step were calculated for each test case, and compared with the mass value programmed into the ANSYS model.

Convergence was achieved if the calculated value of mass equaled the programmed value. Results from this verification showed that the converged value of calculated mass was within 1.5% or less of the programmed mass, meaning that the ANSYS model was following the conservation of energy, and that the thermal capacitance of the propellant was properly being modeled (see Table 3.1) [25].

Table 3.1: Percent Difference in Modeled vs. Calculated Mass. (Data from [25])

Case	Percent Difference
10% Load	1.16
15% Load	0.40
20% Load	0.10

### 3.2.3 Thermal Desktop Verification

Validation of the ANSYS model was accomplished by comparing temperature-time results for a given propellant load case with temperature results from Thermal Desktop. The Thermal Desktop model of the MMS propellant tank was independently created by MMS's thermal subsystem team. This model accounted for not only the heat transfer of the tank, but of the rest of the MMS spacecraft. Comparison of the ANSYS and Thermal Desktop models of the propellant tanks showed good agreement for the 20% load case, with a maximum percent difference in temperatures of less than 5% (see Figure 3.2) [25].

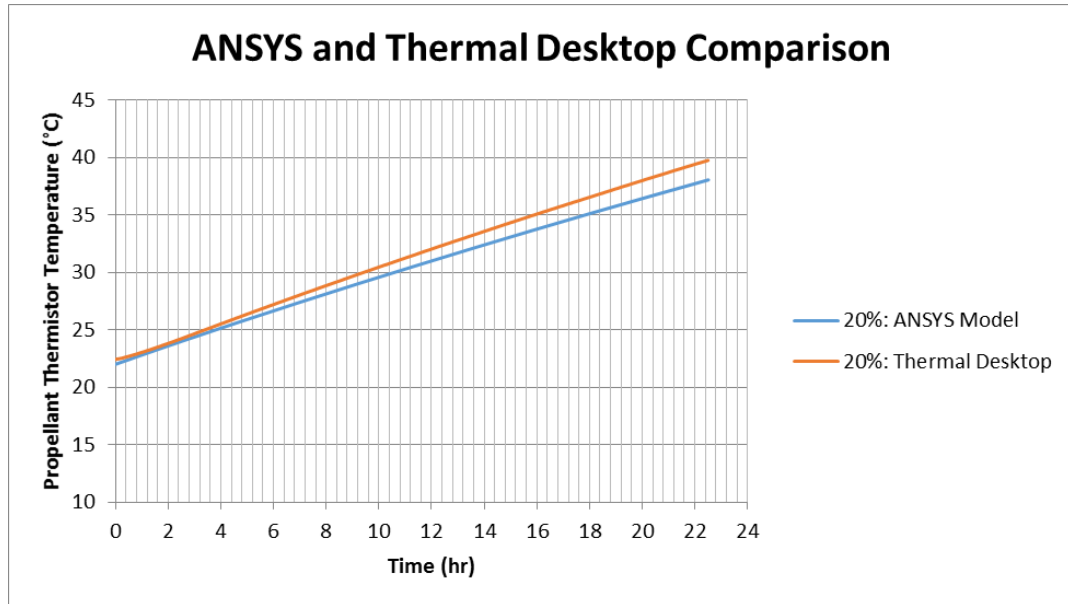


Figure 3.2: Comparison between ANSYS (blue line) and Thermal Desktop (orange line) temperature results for the 20% propellant load case. The maximum difference between the two estimates was found to be 5% between the two models. (Image adapted from [25])

### 3.3 Thermal Model Results

The three load cases were simulated in the ANSYS thermal model. Each case simulated a 55 hour heating of the tank using the liquid side heaters. Figure 3.3 [26] shows the results of this simulation. The point at which the over-temperature thermostat would activate is noted. Since the ANSYS model did not account for thermostatically controlled heaters, simulation results beyond the thermostat temperature limit do not hold any physical meaning for the real tank system.

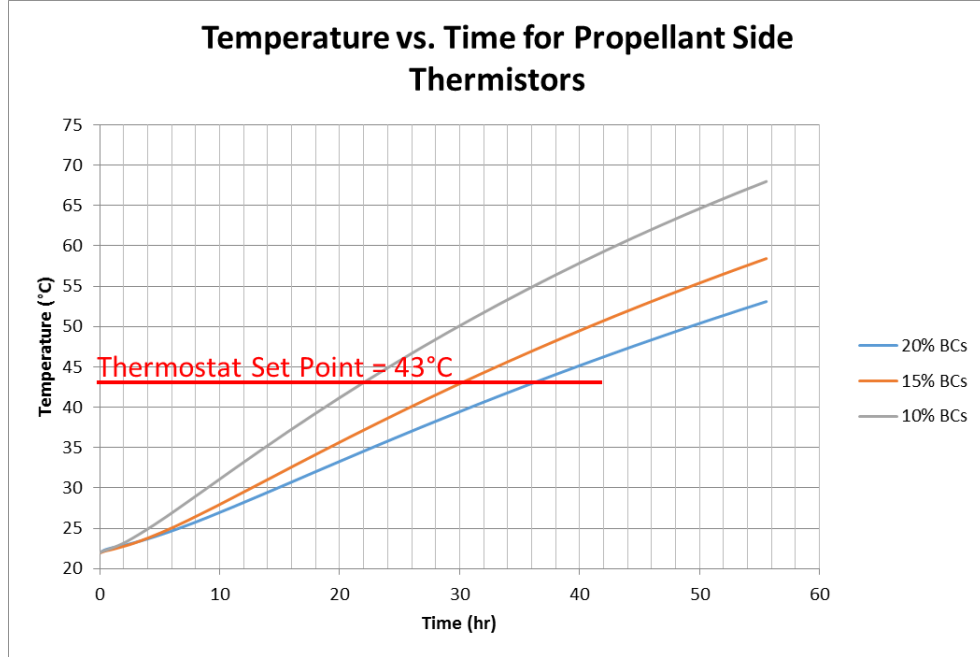


Figure 3.3: Results from the Phase I thermal model for 10, 15, & 20% load cases. Note that after the thermostat set-point is reached, temperature results are not valid since in reality the thermostat would have been activated, turning off the heaters. This behavior was not modeled in Phase I. In the figure legend, “20% BCS” corresponds to the 20% load case, “15% BCS” corresponds to the 15% load case, etc. (Image adapted from [25])

### 3.4 Preliminary Error Estimation

The results from the Phase I tank thermal model allowed for a preliminary estimation of mass estimate uncertainty. Using the temperature vs. time results, mass vs.  $\frac{dT}{dt}$  derivative relations could be found, allowing for a mass percentage estimation to be derived [25]. Equation 3.3 shows the result of this derivation.

$$\Delta m = \frac{-0.81}{t} \left( \frac{T - 22.85}{2.51t} \right)^{-3.04} \Delta T \quad (3.3)$$

As an illustrative example, a 1°C error in temperature at a reading of 37°C



after 20 hours of tank heating yields a mass uncertainty of 1.9%. Improvements in this error estimation can be made by running more propellant loading cases and correlating the results with test data obtained either from the spacecraft or through other ground testing.

The methods applied and process used to develop the Phase I tank thermal model formed the basis for correlating the model with thermal vacuum test data in Phase II. In the following Chapter, extensive details and explanations into the correlation of the tank thermal model and the correlation methods used will be presented. Detailed discussions—particularly of the assumptions used, configuration of the tank, and boundary conditions—will be made. Finally, correlated model results will be presented, along with uncertainty analysis results from varying key input parameters.

## Chapter 4: Phase II: ANSYS Model Development & Correlation Using Thermal Vacuum Test Data

The following sections describe the details of developing the ANSYS thermal model and correlation of that model using thermal vacuum test data. This chapter is divided into five main sections: Thermal Vacuum Test Overview, Model Development, Final Results, Uncertainty and Uncertainty Analysis Results. The Model Development section contains details regarding the assumptions used, material properties, boundary conditions, solid model, correlation process, etc. The Final Results section provides the results of the correlation, and the Uncertainty Analysis section provides details on the effects of varying different parameters, such as mass and heater power, on the correlated model.

### 4.1 Thermal Vacuum Test Overview

The thermal vacuum (TVAC) test seeks to test the entire spacecraft in a space-like environment. The test duplicates both the vacuum of space and the temperatures seen by the spacecraft during its mission. One of many tests completed during MMS TVAC was the tank heater circuit over-temperature thermostat validation test.

This test served to verify the operation of the two thermostats that control two sets of heater circuits on the tank: the gas side and liquid side heaters. The test also duplicates the conditions of an actual thermal capacitance gauging operation on orbit. The TVAC test did not duplicate the propellant load in the tank. The tank was filled with an Argon and Nitrogen gas mixture, rather than propellant or another liquid simulant. This meant that there was gas on both sides of the diaphragm within the tank. This differs from the flight condition of the tank, where the diaphragm will separate the pressurant gas from the liquid propellant.

Once thermal steady-state has been reached, the test is conducted by turning both liquid and gas heaters on. This heats the tank until the over-temperature thermostat set point—43°C—is reached. Once the set point within the thermostat's tolerance is reached, the thermostat opens, shutting off power to the heater circuit. The total test took approximately 6900s from heater circuit turn-on until the last over-temperature thermostat had activated.

The thermal model developed for Phase II was correlated using the data from the over-temperature thermostat test. Heater current and temperature data from the test were fed into the thermal model. The resulting model output was compared with temperature data recorded during the test by multiple 1-wire temperature sensors placed at different parts of the tank.

## 4.2 Model Development

### 4.2.1 Description of Tank System

The propellant tank modeled is one of four tanks installed in a cruciform configuration within the MMS spacecraft as shown in Figure 4.1 [27]. Figures 4.2(a)-4.2(c) show the overall solid model of the propellant tank with annotations to the key parts listed in Table 4.1 and referred to throughout Chapter 4.

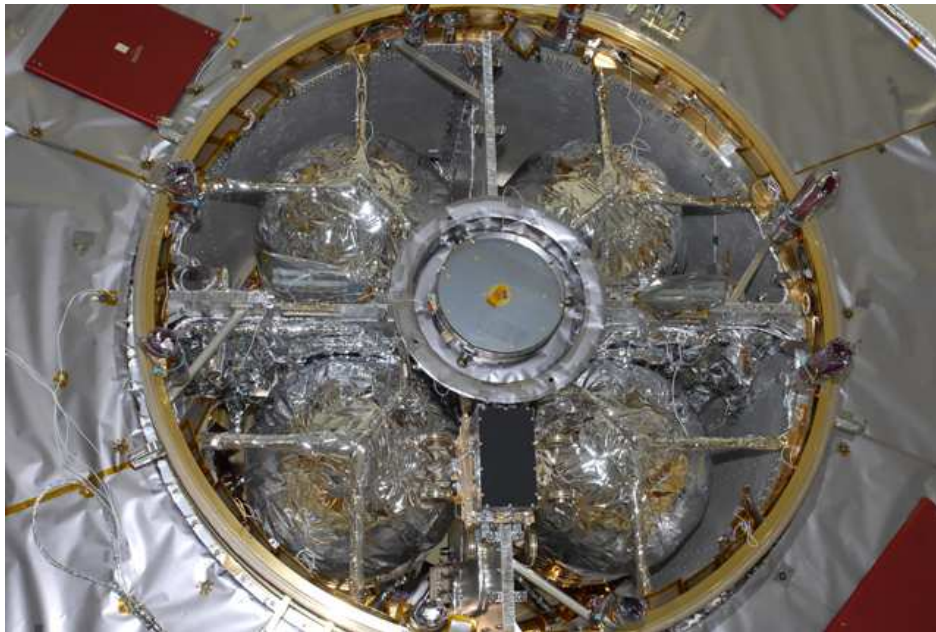


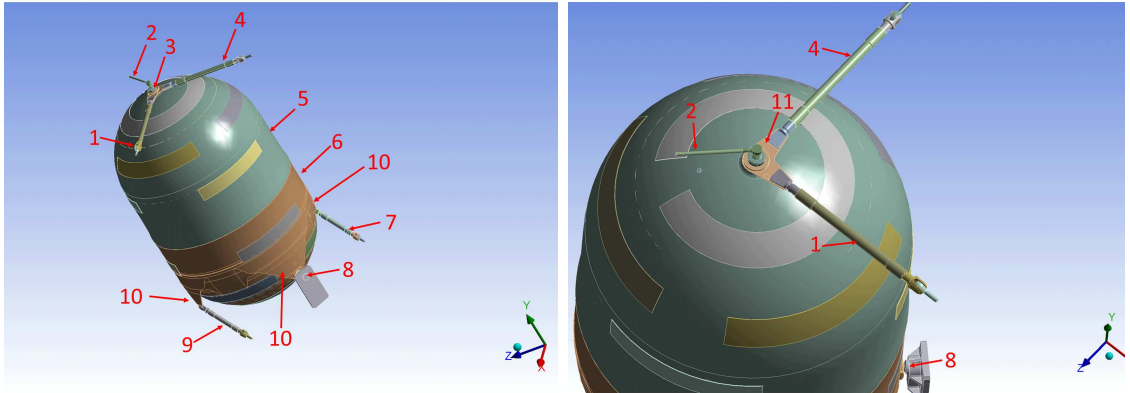
Figure 4.1: Flight configuration of the propellant tanks on MMS. Tanks are mounted in a cruciform configuration and attached to two rings (gold-colored structure in photo), one ring on the top and other on the bottom of the tank. All tanks and surrounding hardware are blanketed. (Image from [27])

Each tank is attached to two structural rings inside of the spacecraft via four struts (#1, 4, 7, 9) and an axial pin (#8). The upper struts of the tank are attached

to the boomerang (#11), which is attached to the gas side tank boss (#3). The lower struts and axial pin are attached to tabs (#10) on the liquid side of the tank. Since the tank contains a diaphragm that separates liquid from gas within the tank, fluid enters the tank via the liquid feed tube (#14) during propellant loading and leaves through the same tube during flight. Pressurant gas enters the tank via the gas feed tube (#2) and then expands within the tank during flight.

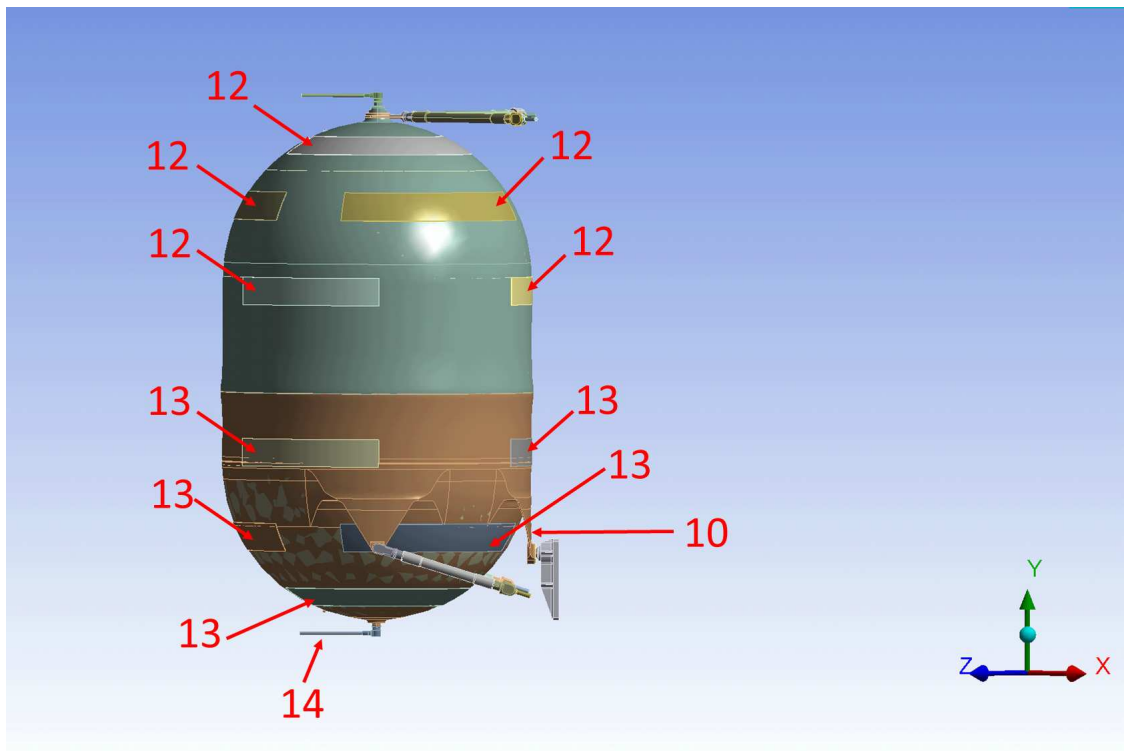
The tank itself is divided into two general regions: the gas and liquid sides (#5 & #6). These regions correspond to how the fluid within the tank is separated by the diaphragm. As discussed in Section 4.1, the tank was completely filled with an Argon and Nitrogen gas mixture, so both gas and liquid sides of the tank were occupied by pressurant gas. To keep with the flight configuration naming conventions, the nomenclature of “gas side” and “liquid side” was maintained.

Both regions of the tank contain a total of 14 heaters: 7 gas and liquid side heaters (#12 & #13). The gas and liquid heaters are each on their own circuit and can be turned off and on independently. To protect the tank against over-heating, each heater circuit contains an over-temperature thermostat with a set point of 43°C.



(a)

(b)



(c)

Figure 4.2: Tank model configuration with key parts labeled. See Table 4.1 for nomenclature reference.

Temperature is measured using both non-flight and flight temperature sensors. For testing, non-flight digital 1-wire temperature sensors are used. These sensors

Table 4.1: Tank Nomenclature

ID	Description	ID	Description
1	Upper Right Strut	8	Axial (Belly Button) Pin (inside of Receiver Plate)
2	Gas Inlet Tube	9	Lower Right Strut
3	Gas Side Tank Boss	10	Tank Tab (strut tabs on left/right of tank; belly button tab towards front)
4	Upper Left Strut	11	Boomerang
5	Upper Hemisphere	12	Gas Side Heater
6	Lower Hemisphere	13	Liquid Side Heater
7	Lower Left Strut	14	Liquid Outlet Tube

are located throughout the spacecraft to give detailed information to correlate the thermal model of the spacecraft. These sensors are de-activated prior to launch and are not used in flight. There are far fewer flight thermistors on the spacecraft, and are typically located on critical hardware in a few key positions. The MMS propellant tanks have two flight thermistors, one located at each pole of the tank to sense gas and propellant side temperatures. Flight thermistors are not typically used to correlate thermal models, though they will be the only means to measure temperature on the tank during the MMS mission.

#### 4.2.2 Assumptions

The following documents the assumptions that were made when developing and correlating the tank thermal model, as well as the rationale and justification for each.

- Convection within the Nitrogen/Argon mix inside of the tank was neglected. In order for the ANSYS model to close, heat transfer through the gas was modeled as conduction as if the gas were a solid. The mass of the gas was accounted for.

The propellant tank tested in the MMS TVAC test was filled with a nitrogen/argon mixture. Since the tank system was effectively closed (no valves were open and the system was all welded), the gas inside of the tank can be considered at rest and the amount (mass) to remain constant throughout the duration of the test. As heat is applied to the tank walls, natural convection of the gas inside of the tank can occur.

The Rayleigh number gives a convenient means to determine if the heat transfer within a fluid is dominated by conduction or convection. If the Rayleigh number is large ( $10^6$  to  $10^8$ ) natural convection is present in the gas. The Rayleigh number was calculated via Eq. 4.1 for the propellant tank to determine if natural convection was the dominant mode of heat transfer within the gas. The calculation was simplified by modeling the tank as a vertical flat wall, with vertical length equal to the height of the tank. This was a reasonable simplification since the MMS propellant tank is longer than it is wide.

$$Ra = \frac{g\beta(T_w - T_\infty)L^3}{\nu\alpha} \quad (4.1)$$

Where:

$g$ : Acceleration of gravity

$T_w$ : Temperature at wall



$T_\infty$ : Free stream or quiescent temperature

$L$ : Length

$\nu$ : Kinematic viscosity

$\alpha$ : Thermal diffusivity

$\beta$ : Gas thermal expansion coefficient,  $\beta = \frac{1}{T_\infty}$

The temperature at the wall,  $T_w$ , was assumed to be 43°C, which corresponds to the set point of the over-temperature thermostats. If  $T_w$  were greater, the Rayleigh number would only increase. The quiescent temperature ( $T_\infty$ ) of the tank was assumed to be 31°C, which was approximately the temperature of the tank when thermal balance (thermal steady-state) had been achieved during thermal vacuum testing.

Using the material properties evaluated at  $T_\infty$  in Appendix A, the tank height, and the values stated for  $T_w$  and  $T_\infty$ , the Rayleigh number was found to be  $1.13 \times 10^8$ , indicating that natural convection is occurring inside the tank (see Table 4.2).

The heat transfer into the tank system, however, is a composite problem as illustrated by Figure 4.3. Heat from the heaters attached to the tank wall is conducted through the heater adhesive, through the titanium tank wall, and finally transferred via natural convection into the gas within the propellant tank.

The total heat transfer from station 1 in Figure 4.3 to station 4 can be represented in circuit notation, with conduction and convection treated as resistances as illustrated in Figure 4.4 and Eq. 4.2-4.3.

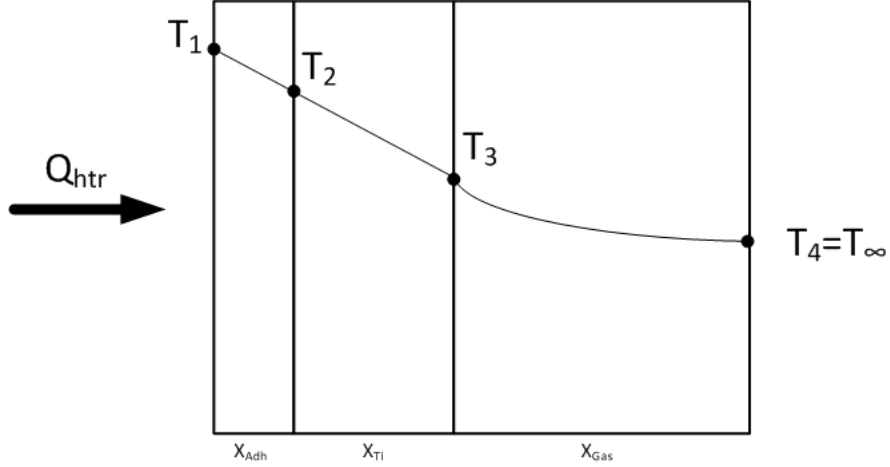


Figure 4.3: 1-D representation of heat transfer through cross-section of propellant tank. Heat travels through the heater adhesive, tank wall and then into the pressurant gas.

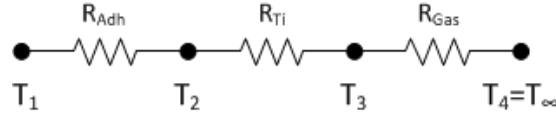


Figure 4.4: Circuit notation of the heat transfer through cross-section of propellant tank.

$$q = \frac{T_1 - T_4}{\frac{x_{adh}}{k_{adh}A} + \frac{x_{Ti}}{k_{Ti}A} + \frac{1}{h_{gas}A}} \quad (4.2)$$

Equation 4.2 can alternatively be written as:

$$q = \frac{T_1 - T_4}{R_{adh} + R_{Ti} + R_{gas}} \quad (4.3)$$

The convective heat transfer coefficient in the pressurant gas ( $h_{gas}$ ) in Eq. 4.2 was estimated by again treating the tank as a vertical wall and calculating the Grashof and Prandtl numbers via Eqs 4.4-4.5. These parameters can be used to

determine the Nusselt number and ultimately the convective heat transfer coefficient.

$$Gr_L = \frac{g\beta(T_w - T_\infty)L^3}{\nu^2} \quad (4.4)$$

$$Pr = \frac{C_p\mu}{k} \quad (4.5)$$

The definition of Nusselt number can be rearranged to give:

$$h_{gas} = \frac{kNu}{L} \quad (4.6)$$

The estimated heat transfer coefficient was checked using two different equations for the Nusselt number as derived for vertical flat plates. Equation 4.7, the Squire-Eckert result for heat transfer at a vertical wall, is derived by Lienhard [28] and Eq. 4.8 by Rohsenow [29]. The results of these calculations are shown in Table 4.2.

$$Nu = 0.678Ra^{\frac{1}{4}} \left( \frac{Pr}{0.952 + Pr} \right) \quad (4.7)$$

$$Nu = \frac{0.508Pr^{\frac{1}{2}}Gr^{\frac{1}{4}}}{(0.952 + Pr)^{\frac{1}{4}}} \quad (4.8)$$

The calculated convective heat transfer coefficients using Nu from both Eq. 4.7 and 4.8 are within the same order of magnitude, which is expected and sufficient for this exercise.

Table 4.2 also shows the total conductive resistance of the heater adhesive and the titanium calculated, and the convective resistance of the gas (Eq. 4.2-4.3). These were calculated using representative values of thermal conductivity and tank geometry to obtain an order of magnitude solution. The resulting convective

Table 4.2: Calculated Thermal Quantities

Quantity	Calculated Value
Rayleigh, Number, $R_a$	1.13e8
Grashof Number, $Gr_L$	1.7e8
Prandtl Number, $Pr$	0.663
Nusselt Number, $Nu$ , via Eq. 4.7	56.0
Nusselt Number, $Nu$ , via Eq. 4.8	41.9
<b>Convection Coef. <math>h_{gas}</math> (<math>Nu</math> via Eq. 4.7)</b>	$9.8 \frac{W}{m^2K}$
<b>Convection Coef. <math>h_{gas}</math> (<math>Nu</math> via Eq. 4.8)</b>	$7.4 \frac{W}{m^2K}$
Gas thermal resistance, $R_{gas}$	$5.0 \frac{K}{W}$
Conductive thermal resistance, $R_{cond} = R_{Adh} + R_{Ti}$	$0.03 \frac{K}{W}$
Heat Capacitance Ratio of Ti:N2 + Ar Mix, $\psi$	9

resistance using either value of convection coefficient is two orders of magnitude greater than the combined thermal resistance due to conduction through the solid materials.

This means that heat will tend to flow within the heater adhesive and tank wall much more easily than through the pressurant gas. The flight thermistors on the tank will see temperatures that are representative of the tank wall, rather than the gas. The convection within the gas is therefore not the primary driver in affecting the temperature of the tank.

This result is significant because the thermal analysis of the tank itself, as well as the ultimate propellant gauging estimates made on the flight propulsion system, are concerned primarily with the temperature of the tank wall, not the specific temperature of the pressurant gas or propellant. Tank temperature telemetry on

flight is only returned from thermistors located on the tank wall.

The mass of the titanium tank wall and gas also play a key role in the heat transfer dynamics of the system. A ratio of volumetric heat capacities of the titanium composing the tank wall and the Argon and Nitrogen gas mix can be easily derived. Assuming the same, constant heat input into both materials, the following ratio can be found:

$$\psi = \frac{mc|_{Ti}}{mC_p|_{AR+N_2}} \quad (4.9)$$

If  $\psi$  is greater than 1, then the thermal response of the system will be dominated by the titanium. If  $\psi$  is less than 1, then the overall heat transfer is dominated by the pressurant gas. Using representative properties at  $T_\infty$  and approximate values of the mass of the titanium and the  $N_2+Ar$  gas mix within the propellant tank,  $\psi = 9$  (Table 4.2). Thus, the thermal response is dominated by the mass of the titanium. Even though the gas mixture has a higher specific heat ( $580 \frac{J}{kgK}$ ) than the titanium ( $553 \frac{J}{kgK}$ ), the gas is far less massive than the tank wall, meaning that less energy is stored in the gas and more is stored in the titanium.

As an additional verification of the above reasoning, simulations varying the conductivity of the gas solid model in the tank were run using the Phase I tank thermal model. Two simulations were performed: one in which the conductivity of the gas was left at the nominal value (see Appendix A), and the second in which the gas conductivity was increased 1000x to simulate the more rapid heat transfer one would expect in a gas that is well stirred. Both simulations had identical boundary and initial conditions and heat input. The average temperature of the tank wall

(calculated using a volume-weighted average of all elements in the tank wall solid model) vs. time, and the average gas temperature vs. time are shown in Figures 4.5 and 4.6.

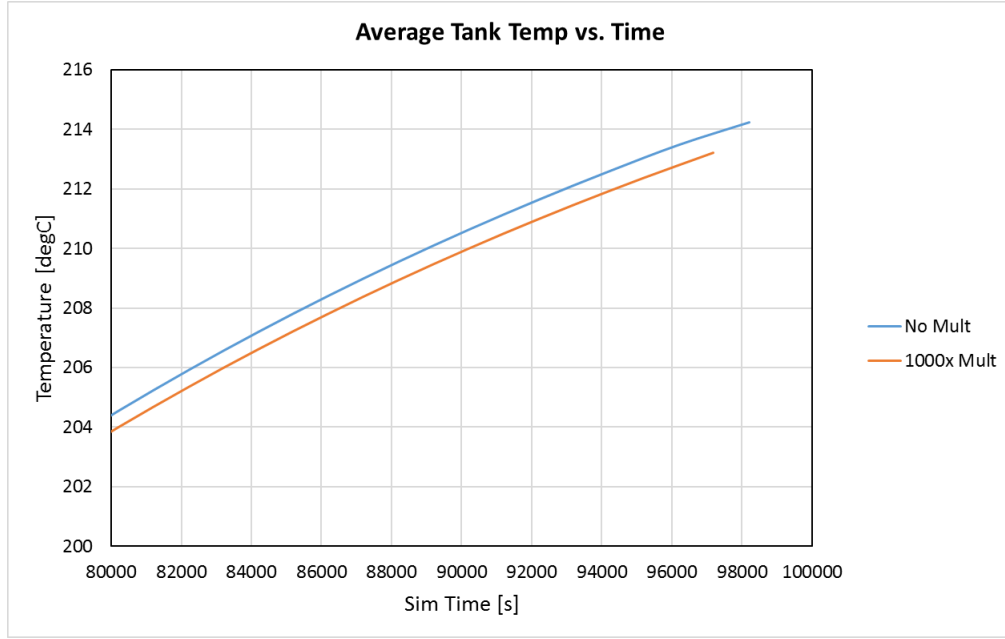


Figure 4.5: Average temperature of the tank wall vs. time for gas conductivity at baseline (blue line) and multiplied 1000x (orange line). Difference in temperatures between cases is approximately  $0.5^{\circ}\text{C}$ .

The difference in average tank temperatures reach a maximum of  $\sim 0.5^{\circ}\text{C}$ , while the difference in fluid temperatures is  $\sim 2.5^{\circ}\text{C}$ . Both differences are small and expected. In Figure 4.5, the difference in average wall temperatures is smaller than in the average gas temperatures (Figure 4.6) due to the larger mass of the wall compared to that of the gas (Eq. 4.9 and Table 4.2).

The higher difference in fluid temperatures between cases is a result of the higher thermal conductivity. Here, the thermal resistance of the gas portion of the

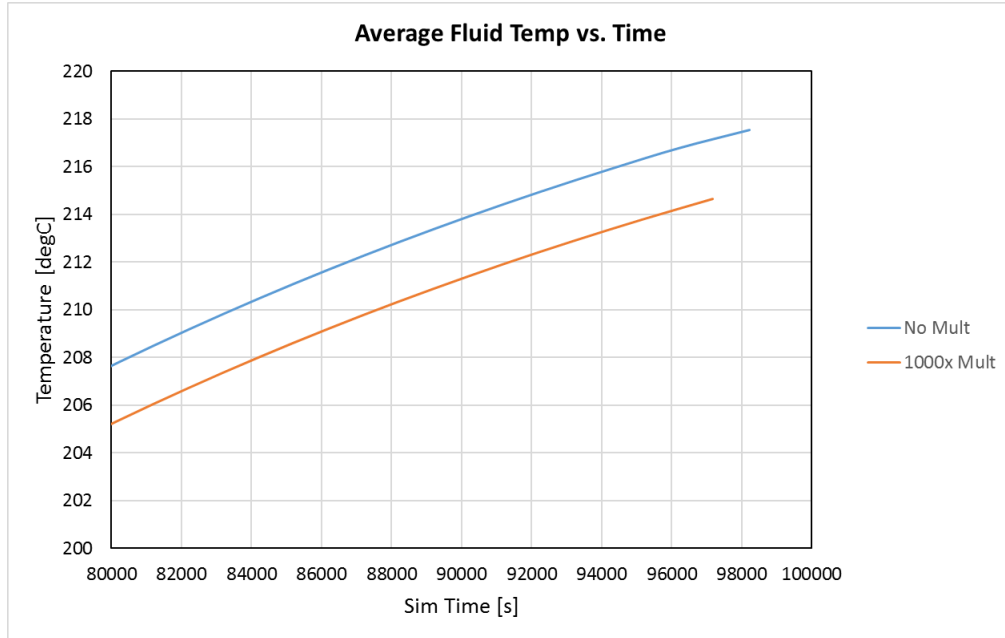


Figure 4.6: Average temperature of the gas vs. time for fluid conductivity at baseline (blue line) and multiplied by 1000x (orange line). Difference in temperatures between cases is approximately 2.5°C.

system is now much lower than that of the titanium wall and heater adhesive (as it would be if the convective heat transfer coefficient were much, much higher, as in a stirred system or tank with fuel sloshing). Thus, more heat is allowed to flow into the fluid itself, raising its relative overall temperature.

This temperature, though, is not stored as readily in the gas due to the gas' low mass. The tank wall, being more massive and therefore having an overall higher volumetric heat capacitance, has smaller differences in temperature over time between cases. The gas, with its low mass and corresponding lower volumetric heat capacitance, has greater differences in temperature over time between cases.

This means that even if the heat transfer in the fluid is modeled as conduction, the overall resulting temperatures in the tank wall are effectively the same. The critical property to account for is the mass of the gas and titanium, which is accounted for in this analysis. Given the above reasoning, the assumption of modeling the heat transfer through the gas as conduction in the ANSYS model is reasonable.

- **The diaphragm within the tank is not physically modeled, but its mass is accounted for.**

In normal operation, the diaphragm separates liquid from gas in the propellant tank, giving the propellant a specific shape, while also forcing the propellant to reside in either hemisphere of the tank. For the TVAC test, both the liquid and gas sides of the tank were filled with an argon and nitrogen mixture. Since the diaphragm separates the same material, there are no differences in the shapes of the gas. The heat transfer through the diaphragm is not a significant player in the overall heat transfer in the problem, since the majority of the heat transfer is already going into the more massive tank (diaphragm mass is on the order of kilograms, while the tank is on the order of tens of kilograms). The mass of the diaphragm was included in the model by smearing its mass within the overall tank model (see Section [4.2.3.1](#) for more details on mass smearing).

- **The tank blanket and tape were not physically modeled, but the mass and thermal properties of each were accounted for.**

Blanket effective emissivity was considered in the model, as this is the key parameter driving the radiation from the tank. The tape itself, with its conductive



adhesive and uniform application, serves to spread the heat evenly around the tank. As described in Section 4.3, the effect of the tape evenly distributing heat from the heaters around the tank was modeled. Both the mass of the tape and blanket were accounted for in the model.

- **Radiation to the average environmental temperature is modeled, but surface to surface radiation between the tank and the surrounding spacecraft enclosure was not.**

During the initial development of the thermal model, the structure surrounding the tank was modeled. As part of the TVAC test setup, both rings where the tank was attached (see Figure 4.1) were held at a near-constant temperature. Test data taken from test sensors located on other parts of the surrounding structure also showed that the temperature remained nearly constant for the duration of the over-temperature thermostat validation test. The surface temperatures of all parts in the model stay within the same magnitude (20-43°C), so radiation losses are negligible compared to conductive losses through the tank interfaces. The radiative heat transfer from the tank to an average environmental temperature was included to account for the small radiative transfer that is present.

In addition, the surface-to-surface radiation from the tank to the surrounding spacecraft was minimized by the thermal design of the tank. The tank itself and other hardware located near it were covered with blankets that had effective emissivities on the order of  $1e-4$ . The portions of the tank that were not blanketed, such as the tabs, have a small surface area compared to the rest of the tank and

therefore contributed very little to surface-to-surface radiation. Radiation transfer to the structure and vice versa was therefore minimized.

This is illustrated in Figure 4.7, which shows the heat flux of different parts of the tank for the time period of the over-temperature thermostat validation test. This data was produced using the Phase I thermal model of the tank to get an order of magnitude understanding of the heat flow distribution within the model.

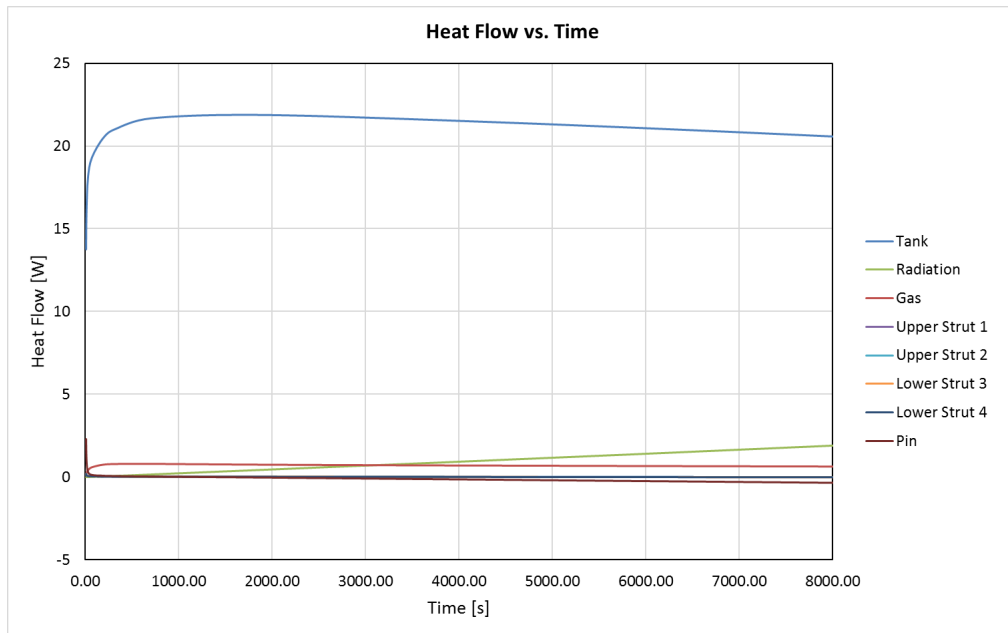


Figure 4.7: Heat flow through different parts within the tank system. The majority of the heat is flowing via conduction through the tank wall (blue line). Radiation (green line) from the tank surfaces is present, but is orders of magnitude less than conductive losses through the tank.

By 7000 seconds (approximately 100 seconds past the end of the over-temperature thermostat test), radiative heat flux is an order of magnitude lower compared to the conductive flux in the tank wall. Therefore radiation from the tank to the enclosure can be neglected with little impact on the overall heat transfer. This also reduces

the overall complexity of the model, decreasing the solve time.

- **A “perfect” bonded contact existed between all interfaces in the model.**

The assumption was made to practically implement the model in ANSYS and serve as a starting point for the correlation process. By default, all contacts are defined as “bonded,” meaning that there are no conductive losses between connected parts. ANSYS does allow for a thermal contact conductance or TCC to be defined at all contacts. A key part of the correlation process was determining how to account for contact conductance losses in the model. Therefore various TCC’s were defined (see Section 4.6) at key interfaces in the model to correlate results to the test data. However, the majority of contacts were left as bonded/perfect since detailed information on conductance for all contacts was not available.

### 4.2.3 Material Properties

Each part of the Pro-Engineer solid tank model was assigned its own material, which in turn was mapped to a database of material properties within the ANSYS Workbench interface. The key properties required in this thermal analysis are density, conductivity, specific heat and emissivity. Density is used to derive mass of a part and the conductivity, emissivity, and specific heat allow for the governing equations (see Chapter 2) to be solved. Table A.1-A.6 in Appendix A provides the master list of materials and material properties used in the analysis, as well as the source used to obtain each property.

That material properties for the tank diaphragm and nitrogen-argon gas mixture did not have properties that could be readily looked up in a table. The properties for the tank diaphragm material were not available from the manufacturer, Dow Chemical. Research into the diaphragm material, similar to AF-E-332, showed that the material had characteristics similar to Nordel 1635 and EPR [30]. The properties of the diaphragm were therefore averaged for EPDM and EPR, which are most similar to Nordel 1635 and EPR.

Properties for the nitrogen-argon gas mixture were calculated based upon the partial pressures of each gas loaded into the propellant tank prior to the TVAC test. The mixture density and specific heat were calculated using the molar fractions of the gas found via the partial pressures. The conductivity of the gas mixture was set at that of nitrogen, since over 90% of the mix was composed of this gas.

Material properties were modified in two different ways: to match the as-measured mass of a part and or to change the effective thermal conductance of a group of parts.

#### 4.2.3.1 Mass of Parts & Mass Smearing

The mass of each part of the solid model in ANSYS is found by calculating the volume that the part occupies and then multiplying that volume by the density of the material assigned to that part. Sometimes, the mass of the part in the model differed from the mass of the real, physical part. This only way to correct this difference was to modify the part's density. In a thermal analysis, density only

serves the purpose of changing a part’s mass, since the volume of the solid part in the model will not change. Table 4.3 shows a representative example of how solid part density was modified to match the actual mass of a part. Calculations like this were used throughout the model to ensure that the total mass of the solid tank model matched the measured mass of the actual tank.

Table 4.3: CAD Part Density Modifications

<b>Part: Lower Strut</b>		
Model Volume:	2.98e−05	$m^3$
Model Initial Density:	5156.05	$\frac{kg}{m^3}$
Model Initial Mass:	0.15348	$kg$
Actual Mass:	0.1746	$kg$
Modified Density:	5866	$\frac{kg}{m^3}$
New Model Mass:	0.1746	$kg$

Smearing of mass was also used to account for the mass of parts that were either distributed around the tank (e.g. the tape), parts where the mass was not known explicitly (i.e. tank diaphragm, heaters, tank blanket), and to account for small hardware that was removed during the de-featuring process (see Section 4.5.1), such as nuts, bolts, washers, and other small hardware.

Since the precise center of mass of the tank was not measured, the tank was divided into the gas and liquid sides (Figure 4.2) and a mass ratio ( $MR_{CAD}$ ) of the mass of the lower side ( $M_{CAD,Lower}$ ) to the mass of the upper side of the CAD model ( $M_{CAD,Upper}$ ) was calculated using the detailed CAD model of the completed MMS

tank (Eq. 4.10). This model included all mechanical and thermal hardware.

$$MR_{CAD} = \frac{M_{CAD,Lower}}{M_{CAD,Upper}} = 0.95 \quad (4.10)$$

The same mass ratio was calculated for the de-featured ANSYS tank thermal model (Eq. 4.11). Since the mass of the actual flight tank assembly was found via weighing the tank during installation (Figure 4.8) [31], the difference between the thermal model mass and the known mass could be calculated using Eq. 4.12 and Eq. 4.13.

$$MR_{Mod} = \frac{M_{CAD,Lower} + X_{mod}}{M_{CAD,Upper} + Y_{mod}} = 0.95 \quad (4.11)$$

$$\Delta m = m_{actual} - m_{model} \quad (4.12)$$

$$X_{mod} + Y_{mod} = \Delta m \quad (4.13)$$

Equations 4.11-4.13 were then solved simultaneously to find the amount of mass needed to be added to the upper and lower portions of the ANSYS model ( $X_{mod}$  &  $Y_{mod}$ ) to maintain the proper mass ratio. This methodology enabled mass to be proportionally “smeared” across the ANSYS thermal model.

#### 4.2.3.2 Effective Thermal Conductivity of Grouped Parts

Mass properties were also modified to model groups of parts. As elaborated on in Section 4.6 and Section 6.2.1.1, individual solid parts were grouped together to ease the correlation process and to model thermal losses through a thermal conductance coefficient (TCC). When parts are grouped in ANSYS, the software does not



Figure 4.8: The propellant tanks were installed by lowering the tank into the propulsion system structure using a crane. A load cell (not pictured) was placed above the propellant tank to determine the mass of the tank. (Image from [31])

allow for an easy way to apply a thermal conductance to the grouped part. It only allows a thermal conductance value to be assigned at a specific contact. Since the default contact type in ANSYS is a bonded contact (see Section 4.2.2), changing the thermal conductance of a strut (Figure 4.9), for example, would require setting the conductance coefficient for each contact between each of the parts. This becomes extremely cumbersome in a model containing hundreds of contacts.

This problem was alleviated by defining groups of parts that shared thermal properties that were based on the mass average of the constituent parts within the group. Table 4.4 shows an example of the thermal properties used for a tank strut, shown in Figure 4.9. The strut consists of four parts (left to right): the tab interface,

strut, clevis, and pin, each of which has its own thermal properties. These individual thermal properties were combined into a new material with thermal properties that were based upon the mass averages of each of the parts within the group. These mass-averaged properties were assigned in ANSYS to all individual parts within the group.

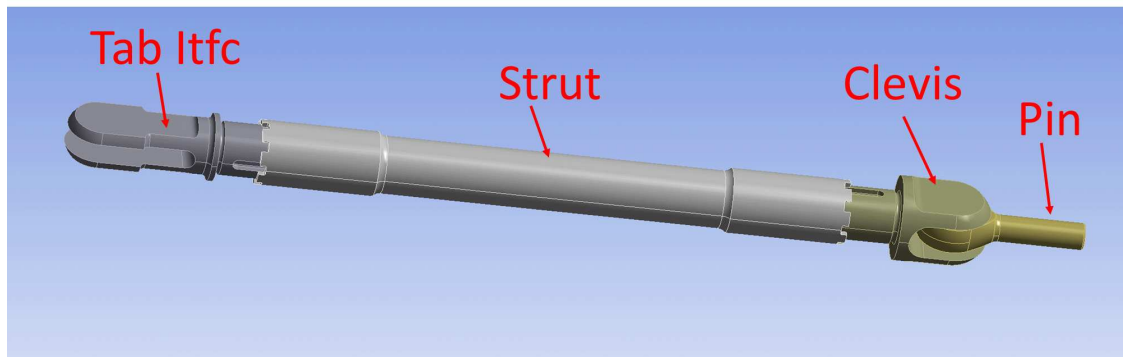


Figure 4.9: CAD model of the tank strut. These parts were grouped together to form one part with its own set of mass properties (see Table 4.4).

Table 4.4: Strut Material Properties. All parts shown in Fig. 4.9 were grouped together and assigned the material properties (labeled “Mix”) based upon the mass fraction of each sub-material.

Sub. Material	Mass Fraction	Thermal Conductivity $\left(\frac{W}{mK}\right)$	Specific Heat $\left(\frac{J}{kgK}\right)$
Pin: 17-4 PH	0.21	10.46	460.5
Tab Itfc: 6-4 Ti	0.24	7.20	554.3
Clevis: 6-4 Ti	0.22	7.20	554.3
Strut: 6-4 Ti	0.34	7.20	554.3
	<b>Mix:</b>	<b>7.91</b>	<b>534.7</b>

From a thermal perspective, the ANSYS software “sees” this as one part,



instead of multiple parts. By definition, the thermal conductance is proportional to the conductivity (see Section 4.6). Since the part cross-sectional area and length remain constant and the thermal contact between each part is bonded (see Section 4.2.2), then the conductance of the grouped part can only be increased or decreased by changing the thermal conductivity of the grouped part. This methodology was used throughout the tank. All grouped part material properties are referenced in Appendix A, Table A.1-A.6.

### 4.3 Initial & Boundary Conditions

Initial conditions, temperature, radiation and heat flux boundary conditions were applied to the tank thermal model. These conditions were based upon test data gathered during the over-temperature thermostat test taken during TVAC.

The initial temperature condition for each run was set to those shown in Table 4.5. These values were based off of 1-wire sensor readings from the over-temperature thermostat test. If no 1-wire sensor was on or near a component, the average temperature of 31°C was used. This average was based on multiple 1-wire sensor readings in the vicinity of the tank at thermal steady-state.

The following subsections will provide specifics for each of the boundary conditions used for the ANSYS thermal tank model.

Table 4.5: Applied Initial Conditions

<b>Component</b>	<b>Initial Temperature (°C)</b>
Lower Ring Pin Receiver	28.0
-Z Tab Interface	32.2
Lower Left Strut	30.7
Tank Tab by Pin	31.4
Lower Hemisphere	33.0
Upper Right Strut	33.5
Gas Inlet Tube	34.2
Liquid Outlet Tube	29.9
All other parts	31.0

### 4.3.1 Temperature Boundary Conditions

Temperature boundary conditions were applied at the interface of the upper and lower rings to the tank struts (i.e. at the strut pin, see Fig. 4.9), the receiver pin plate (also attached to the ring), and gas and liquid feed tubes, as shown in Figure 4.10. The temperatures of the rings were monitored during the TVAC test by a number of 1-wire temperature sensors placed in various spots around the ring. This meant that the temperature at the tank strut pin and ring interface, as well as the receiver pin plate and ring interface, was known. The temperature of the gas and liquid feed tubes were also known from 1-wire sensors located on the tubes.

This known temperature variation meant that the tank thermal model could be simplified by removing the solid models of the rings, and replacing them using only a prescribed temperature boundary condition. All temperature boundary conditions

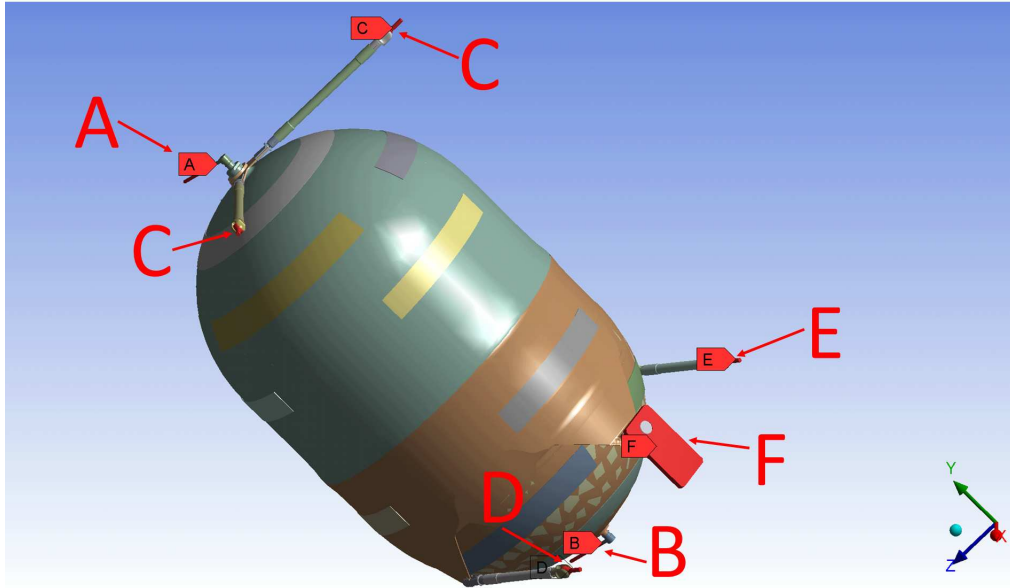


Figure 4.10: Locations of applied temperature boundary conditions (A & B: Gas and Liquid tubes; C: Upper Strut Pins; D & E: Lower Strut Pins; F: Belly Button).

varied with time. The temperature boundary conditions as applied to the tank are shown in Figure 4.10. Values of temperature vs. time for each element is listed in Appendix B, Table B.1.

### 4.3.2 Radiation Boundary Conditions

The radiation boundary conditions were applied to the model using the emissivities of the tank blanket, struts, and other exposed parts of the tank. Specific emissivities and environment temperatures used are in Appendix B, Table B.2.

Per the assumptions made in Section 4.2.2, radiation between the tank and the enclosure around it was not modeled. This was because the effective emissivity

of the tank blanket is small, the surface area of the exposed tank parts is small, and the duration of the over-temperature thermostat test is short enough that the tank doesn't get very hot and thus radiation heat transfer will be very small.

Figure 4.11 shows the locations on the tank model where radiation boundary conditions are applied. Labels shown in Figure 4.11 are defined in Table 4.6.

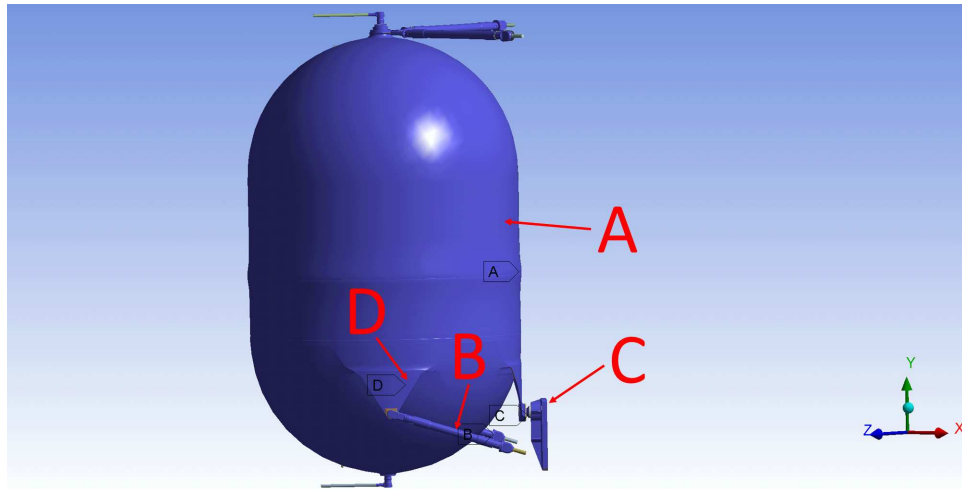


Figure 4.11: Locations of applied radiation boundary conditions (labeled A-D in Figure; see Table 4.6).

Table 4.6: Radiation Boundary Condition Locations

Label	Definition
A	Blanket
B	Struts
C	Tank Pin & Receiver Plate
D	Tank Exposed Parts (tabs, etc.)

### 4.3.3 Heat Flux Boundary Conditions

The heat addition from the tank heaters was modeled as a uniformly distributed heat flux over the entire upper and lower surfaces of the tank. This representation is justified because the tank and heaters are covered in multiple layers of aluminum tape with conductive adhesive.

The heat addition from the tank heaters was calculated from measurements of the tank heater circuit current. The time at which either the gas or liquid heater circuit thermostat activated was determined from looking at time history plots of gas and liquid side temperature and tank heater circuit current, as shown in Figure 4.12. This figure shows that the gas side circuit turns off before the liquid, as well as the time at which each respective heater circuit de-activates. Times are relative to the beginning of heater activation.

Knowing the current and when each thermostat activated for each circuit enables one to compute the power going into the gas and liquid heaters as a function of time. The total heater circuit resistance for all 14 heaters and voltage was calculated using Eqs. 4.14-4.15.

$$R_c = \left( \sum_{i=1}^{14} \frac{1}{R_{htr,i}} \right)^{-1} \quad (4.14)$$

$$V_c = R_c i_c \quad (4.15)$$

The heat flux into the gas side of the tank was calculated using Eqs. 4.16-4.17.

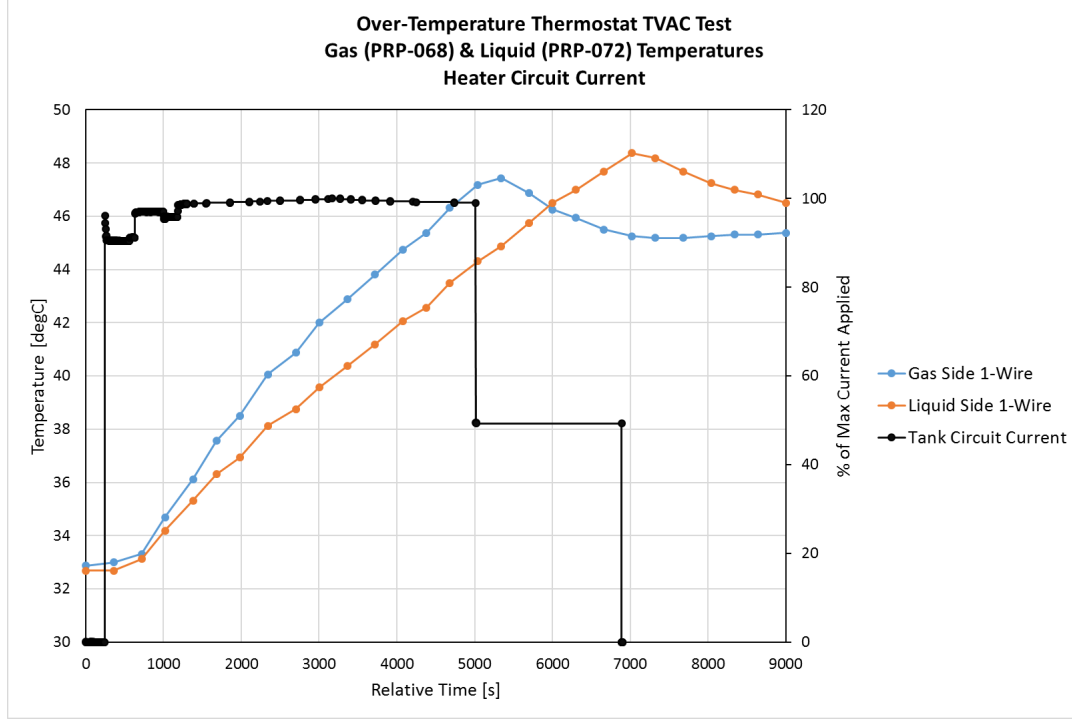


Figure 4.12: Gas and liquid side temperatures (left axis) and heater current percentage (right axis) as a function of time from the TVAC over-temperature thermostat test. The sudden drop to 50% max current at 5000s shows that the gas heater circuit reached its temperature limit and was de-activated before the liquid heater. Times are relative to beginning of heater activation.

Heat flux into the liquid side of the tank was calculated in a similar manner.

$$q_{upper} = \frac{V_c^2}{R_{gasE} A_{upper}} \quad (4.16)$$

$$R_{gasE} = \left( \sum_{i=1}^7 \frac{1}{R_{htr,i}} \right)^{-1} \quad (4.17)$$

The resulting heater heat flux per time for the gas and liquid sides of the tank is shown in Figure 4.13. These values were then applied to the solid model of the tank in ANSYS, shown in Figure 4.14(a) & 4.14(b).

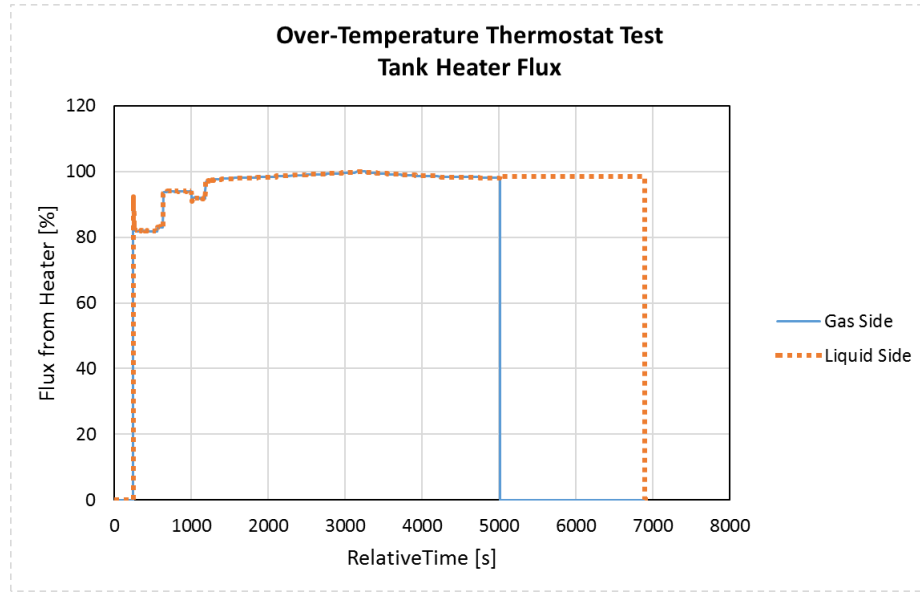
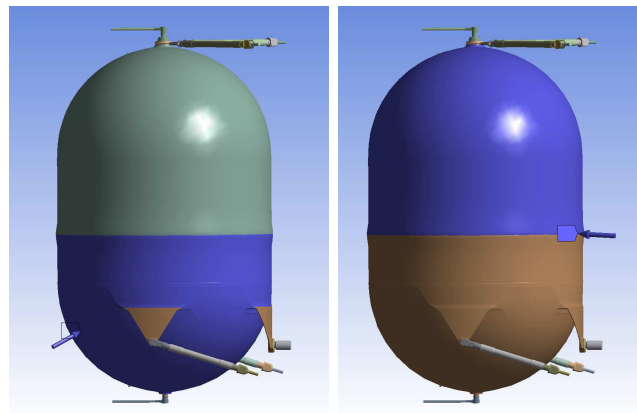


Figure 4.13: Tank heater heat flux vs. time for the gas (blue line) and liquid side (orange symbols) as calculated from recorded current vs. time history during the TVAC over-temperature thermostat test. Times are relative to beginning of heater activation.



(a) Liquid Side Heat Flux (b) Gas Side Heat Flux

Figure 4.14: Location (blue area) of the heat flux boundary conditions on the liquid side (left) and gas side (right) locations in the thermal model.

## 4.4 Sensor Locations and Test Data

Results from the ANSYS thermal model were compared to temperature measurements at seven locations on the propellant tank where 1-wire temperature sensors were available. Table 4.7 lists the sensor locations and corresponding sensor names. Appendix C provides figures of the approximate location of each 1-wire sensor.

Table 4.7: Sensor Location Nomenclature

<b>Sensor Location</b>	<b>1-Wire Sensor Designation</b>
Tank Belly Button Tab	PRP_051
Boomerang	PRP_053
Upper Right Tank Strut by Ring	PRP_054
Lower Left Tank Strut at Tank Tab	PRP_056
Lower Left Tank Strut by Ring	PRP_057
Gas Thermistor	PRP_068
Liquid Thermistor	PRP_072

## 4.5 ANSYS Model Details

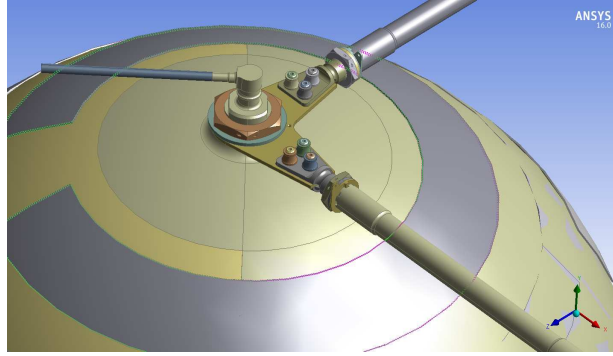
A number of pre-processing steps were completed prior to solving the ANSYS model. These steps were de-featuring the solid CAD model, meshing the model, and defining areas to query nodes to return temperature results.



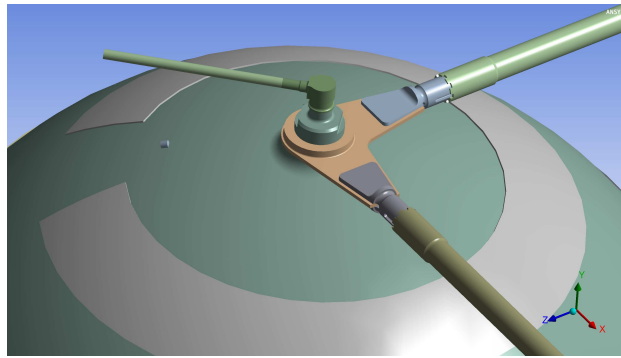
### 4.5.1 Model De-Featuring

Model de-featuring refers to removing features from the model that do not play a large role in the heat transfer but would significantly add to the size and complexity of the mesh. The Pro-Engineer model of the tank provided by the MMS propulsion designer reflected the as-built flight configuration of the tank, and included all flight and non-flight hardware, such as nuts, bolts, washers, lock-wire, thermistors, 1-wires, etc.

Design Modeler, ANSYS's CAD pre-processing tool, was used to de-feature the model. This program allowed extraneous features to be removed, rather than suppressed. Figure 4.15 and Figure 4.16 show examples of the tank before and after de-featuring. Small sensors were removed, as well as bolts, nuts and washers. Bolt holes were filled, and CAD importation errors, such as slivers and small faces, were also corrected.



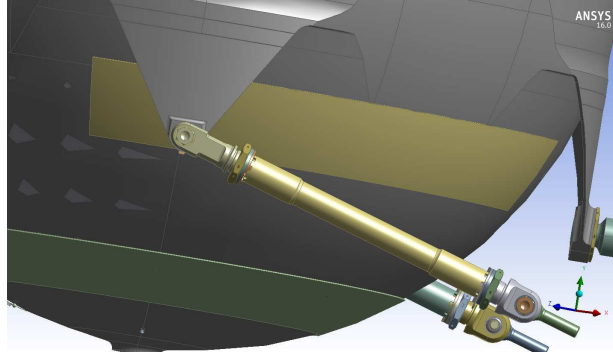
(a) Before



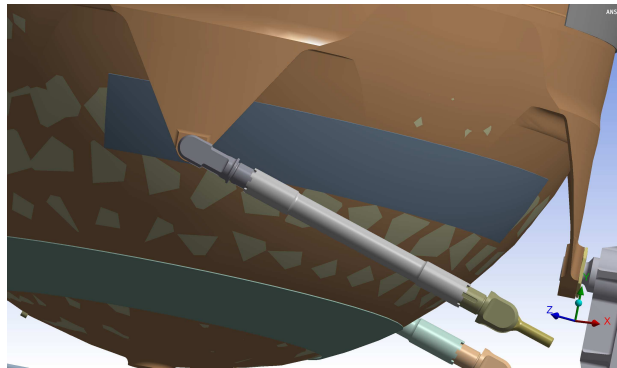
(b) After

Figure 4.15: CAD model of the upper hemisphere region of the tank before (top) & after (bottom) de-features. Small parts, such as bolts, washers and jam-nuts, are removed from the model and bolt holes are filled.

While some fidelity is lost, the smaller mesh size greatly reduces the solve time of the model. Reduced mesh complexity ensures that the model converges at each time step iteration process during the transient solution. Both of these benefits outweigh the small loss of fidelity in the model detail.



(a) Before



(b) After

Figure 4.16: CAD model of the lower hemisphere region of the tank before (top) & after (bottom) de-featuring. Small parts, such as bolts, washers and jam-nuts, are removed from the model and bolt holes are filled.

## 4.5.2 Meshing

After the de-featuring process, the solid model of the tank was meshed using the integrated meshing tools within ANSYS. The mesh was created using automatic mesh controls, generating a patch-conforming/sweeping mesh. The mesh had approximately 175,000 nodes, 88,400 elements and is shown in Figure 4.17.

The mesh was refined using an iterative process to drive thermal error to a min-

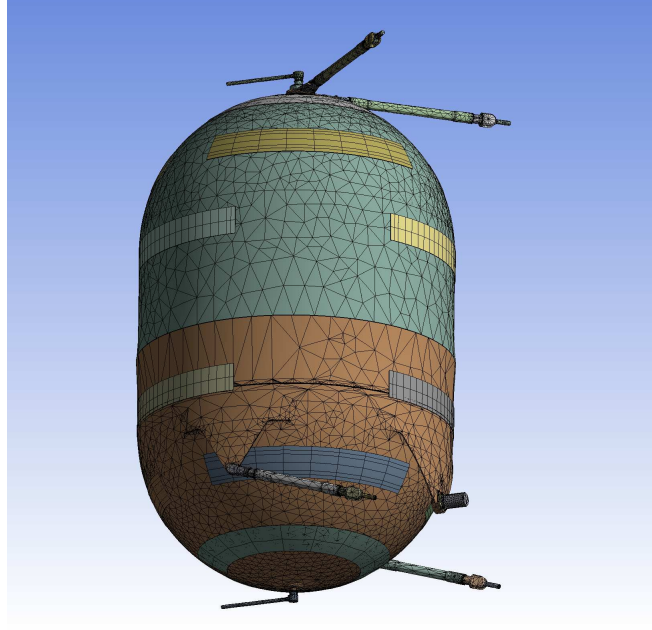


Figure 4.17: The patch-conforming/sweeping mesh generated for the tank and used in the analysis.

imum. Thermal error is a dimensionless and relative measure of differences in flux between elements. This difference in heat flux between elements is calculated [32] by subtracting the heat flux in each node at a given direction ( $\mathbf{q}^i$ ) from the average heat flux at each node ( $\mathbf{q}^a$ ), per Eq. 4.18.

$$\Delta \mathbf{q} = \mathbf{q}^a - \mathbf{q}^i \quad (4.18)$$

The dimensionless error per element is found by numerically integrating all of the nodal flux differences within the element volume, as represented by Eq. 4.19.

$$e_i \propto \int \Delta \mathbf{q} dV_{elem} \quad (4.19)$$

Finally, the total error is the sum of all the errors in each element in the model

(Eq. 4.20) [32].

$$e = \sum_i^N e_i \quad (4.20)$$

The more nodes a model has the less relative error,  $e_i$ , exists. Therefore the total error in the model is reduced. The thermal error is relative since it only compares fluxes from element to element, and does not account for all of the elements simultaneously. Thermal errors are typically small (on the order of  $1e-3$  or less), even in the coarsest of meshes.

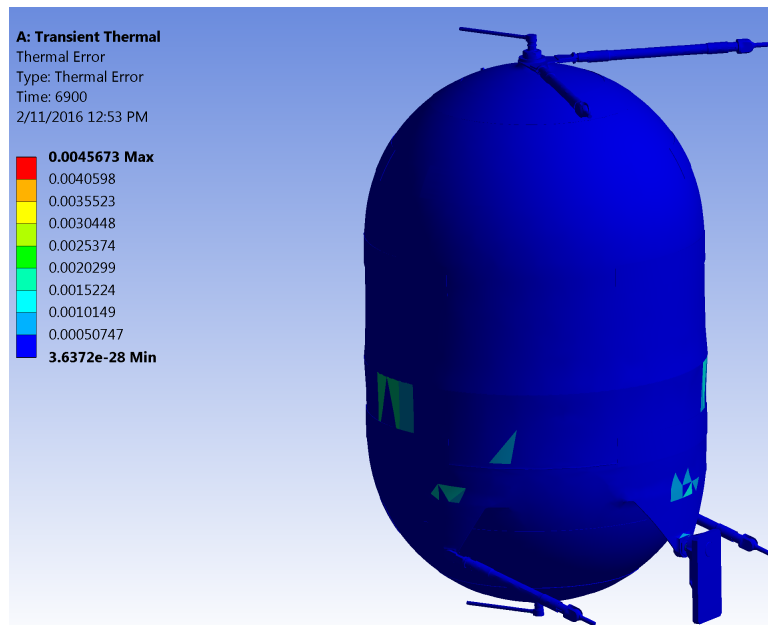


Figure 4.18: Distribution of the thermal error in the tank mesh. The vast majority of the thermal errors are between zero and  $5e-3$ . Note that thermal error is dimensionless and is a relative measure used primarily to guide mesh refinement.

According to the ANSYS training material, the thermal error is best used to show what parts of the mesh should be refined, rather than used as an absolute measure of error in the problem [33]. This guideline was applied to the tank thermal

model mesh. The thermal error for the mesh used in the model is shown in Figure 4.18. The greatest *relative* error was on the order of  $1e-3$ , with the vast majority of the mesh having a relative error of  $1e-28$ , which is effectively zero. The maximum relative error occurs in a small cell within the tank belly button tab assembly. Mesh refinement removed this error, and a subsequent sensitivity study performed (see Appendix E) showed that error magnitudes of this order or smaller had no major impacts on the results of the model.

The areas with higher relative thermal error were minimized by changing local mesh sizing during mesh refinement to the best extent possible to balance both accuracy and solve time. For example, the mesh shown in Figure 4.17 resulted in a solve time of approximately 45 minutes. A denser mesh with lower overall relative error, as shown in Appendix E, Figure E.2, resulted in a solve time of approximately 89 minutes. Differences in temperature results between both cases were negligible (see Appendix E).

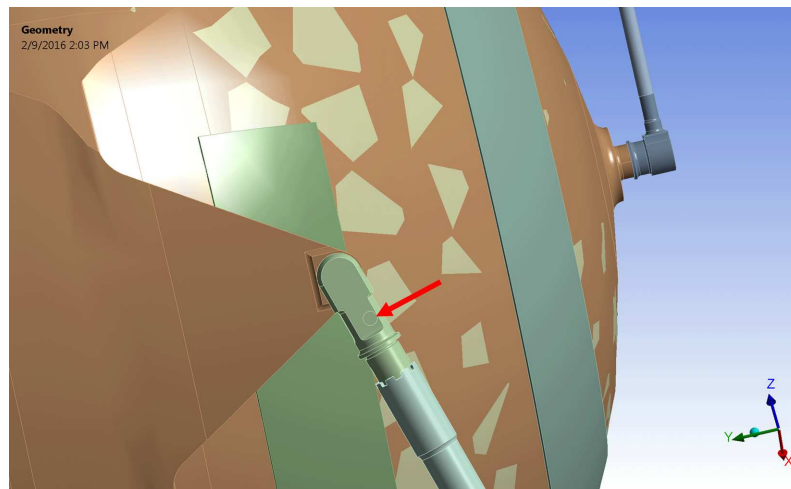
### 4.5.3 Locations to Query Results

Temperature solution results from ANSYS were returned by querying pre-defined areas on the solid model. Each of these areas approximately corresponded to the location of a 1-wire sensor used in the test, as listed in Table 4.7. The locations on the CAD model were approximated within centimeters of the actual bond location, since information of the precise bonded location of each 1-wire sensor was unknown. The location of the 1-wire sensor in the model was approximated by

referencing photos of actual installed sensors on the tank, as shown in Figure 4.19.



(a) As-Built Location



(b) CAD Model Location

Figure 4.19: Photograph of the lower left tank tab showing the location of the 1-wire temperature sensor as-built (top). CAD rendering of the lower left tank strut (bottom) with arrow showing the approximate location of the temperature sensor inferred from the photograph.

Areas were specified by creating a small circular patch area on the solid model

of the tank. This circle was imprinted onto the solid model, which created an area—or surface—from which temperature results could be queried. After the model was solved, an area-weighted average temperature was calculated from all of the nodes located on the defined surface. Appendix D describes the algorithm that was used to calculate the area-weighted average temperature at each of the defined surfaces. This methodology was used for all sensors listed in Table 4.7. All locations on the model can be seen in Appendix C.

## 4.6 Model Correlation Process

### 4.6.1 Overview & Approach

Model correlation was done using a systematic process that started with matching temperatures at locations with relatively simplistic heat transfer paths, and then broadened to areas with more complex heat paths. Correlations began with the tank struts, since the heat flow through them was almost purely conductive. After the struts were correlated, other parts of the tank, such as the tank wall and tabs, were analyzed. Finally, individual piece parts, like the boomerang, were analyzed to further refine the correlation.

Modifications to correlate the model were not made in an ad-hoc fashion, but done to reflect the as-built configuration of the tank, and capture the effects of tape, harnessing, blanketing, and other as-built features that differed from the CAD model. Modifications were made one at a time, with the model re-solved after every revision. This tedious approach was made to learn how the model responded



to changes. Temperature changes throughout the tank were monitored and noted to assess the impacts of modifications to different parts of the model. Future modifications were then based on the observed behavior. This process was iterated until the objective of correlating model temperatures to within +/- 3°C of the test temperatures was achieved. An approach utilizing a numerical optimization technique to accomplish this correlation could also be used, and is discussed in Section 6.3, Future Work.

Correlating the model involved changing the thermal conductance of different parts to match temperatures in the model to temperatures recorded by the 1-wire sensors during the over-temperature thermostat verification test during TVAC. The thermal conductance is defined from Fourier’s Law. For 1D heat flux through a block, Fourier’s Law to can be written as follows:

$$Q = -U\Delta T \tag{4.21}$$

where U is the thermal conductance defined as

$$U = \frac{kA}{L} \tag{4.22}$$

The thermal conductance is an inverse of thermal resistance, and has SI units of  $\frac{W}{K}$ . It is analogous to electrical conductance ( $\frac{A}{V}$ ) or the dimensionless loss factor,  $K$ , in component fluid flows. ANSYS designates the thermal conductance between contacts as the Thermal Contact Coefficient or TCC. As described in Section 4.2.3.2, ANSYS defines a TCC wherever there is a contact between two solid parts in the model. By default, this contact is defined as “bonded” or “perfect,” meaning that the TCC is set to a value so high that there is effectively no heat loss between parts.

This poses problems when one tries to use it to reduce temperature prediction errors since the conductance value at every contact may not be known, and defining a conductance value at every contact in a complicated model becomes overly complicated and tedious.

This problem was alleviated by defining groups of parts that shared thermal properties that were based on the mass average of the constituent parts in the group (Section 4.2.3.2). Since the model geometry within ANSYS is fixed, the grouped part's cross-sectional area and length are also fixed. Therefore, per Eq. 4.22, the only way to effectively modify the thermal conductance of a grouped part within ANSYS is to modify the conductivity material property. This is effectively the same as modifying the thermal conductance at each contact within the grouped part, however that conductance is now spread across the whole grouped part, rather than at one specific contact.

## 4.6.2 Conductance Study Results

The main conductance studies were done on the struts and on the boomerang. The primary purpose of these studies was to analyze how the model behaved when conductance at key locations in the model were changed, and how those changes effected the predicted temperatures at each of the 1-wire locations.

Changes to the model were not necessarily made in a linear fashion. Experimentation with the model, via tweaking values to understand the effects, occurred frequently. These experiments sometimes yielded important lessons, and at other

times yielded no useful results. This experimentation sometimes caused large differences in temperatures between model revisions and conductance studies. These differences were sometimes due to finding errors in modeling, such as discovering and correcting an error in mass distribution or how temperatures were queried from the model.

Results shown in the following sections provide a brief summary of the studies performed. Temperature differences were taken at the end of the simulation run, and compared to the test data. For brevity, the results shown in the following subsections only highlight some of the major studies completed. See Appendix F for the complete change logs.

#### 4.6.2.1 Lower Strut Tab Interface Conductance Study

The first conductance study focused on the lower tank strut tab interfaces. The TCC value was modified at the tank tab-strut interface as shown in Figure 4.20, as well the conductance through the strut as a whole, which was defined as a grouped part (see Table A.1, Appendix A).

Prior to beginning the lower tank strut conductance study, photographs of the as-built tank were consulted. They revealed that an electrical harness was routed along the lower right strut, providing an additional path for heat exchange that was not accounted for in the CAD model. Since the exact effect this wire would have on the overall conductance of the strut was not known, an estimate of the increase in conductivity to the strut was made. The conductivity multiplication factor (CMF)

of this strut was set at 2.0 to capture the effect of the electrical harness on the conductivity of the strut materials.

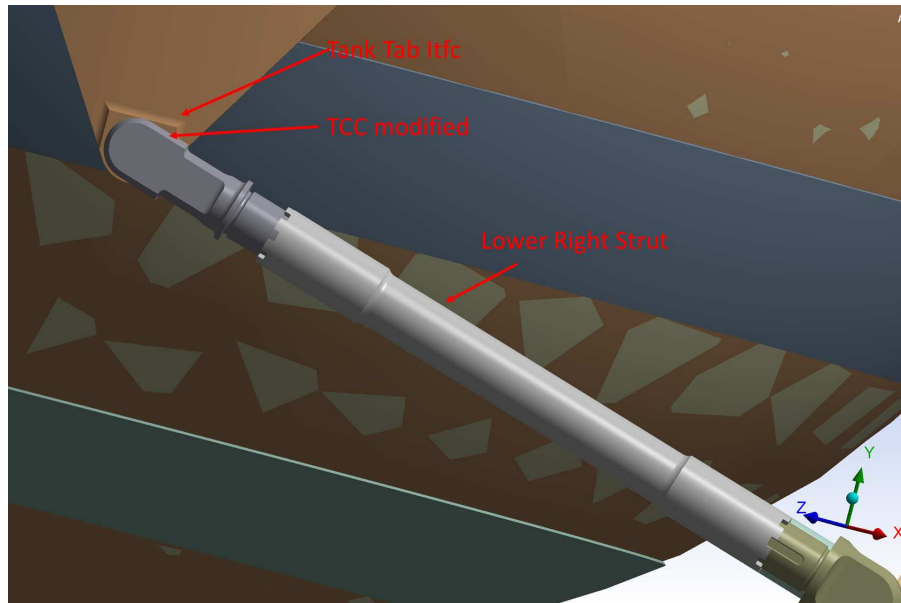


Figure 4.20: Locations on tank lower strut where conductance values were modified. Left and right lower struts are identical.

Table 4.8 shows that as the TCC at the lower strut/tab interface (see Figure 4.20) was increased (allowing more heat flow) while maintaining a constant overall grouped strut conductivity, the temperature difference at the lower left strut tab (PRP\_056) location increased. This meant that too much heat was flowing through the strut. The TCC was then reduced, resulting in smaller temperature deltas. Recall that “perfect” contact is characterized by large TCC values, so the larger the TCC, the less conductive losses there are at a contact region.

Changing the strut conductance did little to impact the temperatures at the liquid (PRP\_072) and belly button tab (PRP\_051) locations. Instead of increasing

Table 4.8: Lower Strut Tab Interface Conductance Study Results

Rev	Lower Strut TCC ( $\frac{W}{m^2K}$ ) at Tank Tabs		Lower Hemi CMF	Difference of Model Measured Temp ( $^{\circ}C$ )		
	Right TCC	Left TCC		Liq (PRP_072)	Belly Button Tab (PRP_051)	LL Strut Tab (PRP_056)
31	20	20	1.5x	3.415	3.723	1.08
29	50	50	1.5x	3.402	3.714	3.563
28	75	75	1.5x	3.397	3.711	4.363
27	127	127	1.5x	3.391	3.707	5.112
30	175	175	1.5x	3.389	3.706	5.43
32	20	20	2.0x	2.538	3.815	1.392
33	20	20	2.0x	2.439	0.473 <sup>a</sup>	1.293

<sup>a</sup>In this Rev, results were queried from a patch area instead of a full selected area as done in Rev. 32 (see Ch. 6, Section 6.2.2.)

the lower strut conductivity multiplication factor, CMF, even higher, it was postulated that the tape covering the tank wall was providing a higher conductivity on the lower portion of the tank than previously modeled. The lower hemisphere CMF was increased to 2.0, while the lower left strut conductance was reduced (Revisions 32-33). This resulted in a slight increase in temperature difference at the lower left strut location (PRP\_056), but significantly reduced the temperature difference in the liquid side (PRP\_072) and belly button tab (PRP\_051) sensor locations sensor locations.

#### 4.6.2.2 Boomerang Conductance Study

Another conductance study was undertaken at the boomerang and strut interface locations (see Figure 4.21). Values of the TCC were modified at the locations shown in the figure. This study was conducted since it was discovered that details around the tank boss and boomerang interface were not properly modeled in the CAD program. Surfaces between the tank boss and boomerang were not present in the CAD model, and the boomerang interfered with the tank boss. The interference was corrected, but the lack of surfaces between the tank boss and boomerang could not be corrected. It was suspected that these errors were causing artificially low temperatures in the upper hemisphere, boomerang, and struts.

Table 4.9 shows the results from the study. Reducing the boomerang TCC reduced the temperature difference seen from 1-wire locations at the boomerang (PRP\_053) and upper strut end (PRP\_054) locations. Since the lower tank hemi-

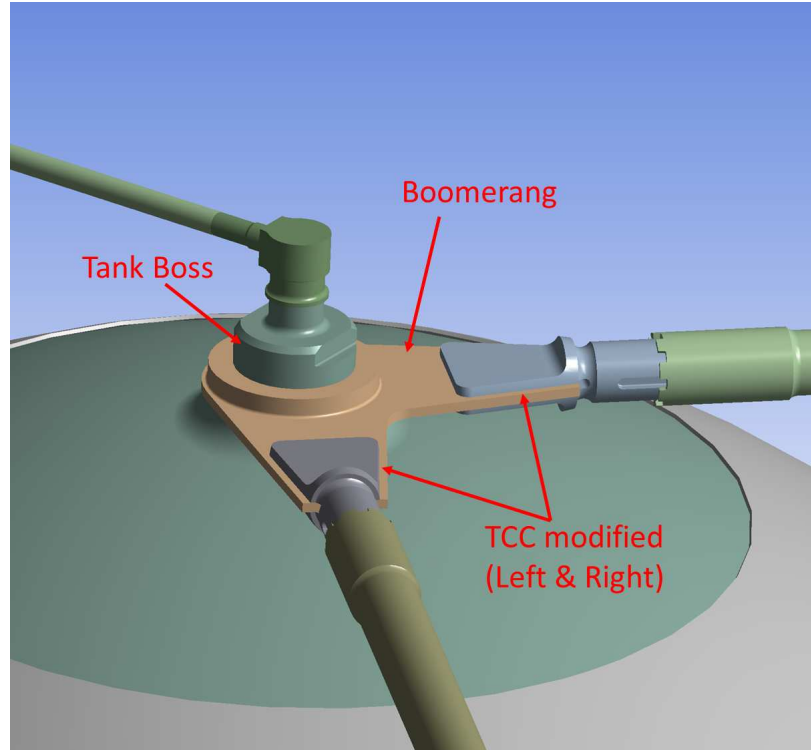


Figure 4.21: Locations near the Boomerang where conductance values (TCC) were modified.

sphere CMF was increased in the previous study (see Section 4.6.2.1), the upper hemisphere of the tank CMF was also increased. This change resulted in a lower temperature delta from the boomerang (PRP\_053).

The change in Rev. 45 also impacted behavior in other parts of the model. Slight increases in temperature deltas in the lower portion of the tank (PRP\_072, PRP\_051 and PRP\_056) were noted. This increase was due to a greater thermal resistance in the upper portion of the tank, allowing less heat to flow through the boomerang and out of the upper struts. Slightly more heat flow went to the bottom portion of the tank, slightly increasing temperature there.

Table 4.9: Boomerang Conductance Study Results

	Boomerang			Difference of Model Measured Temp (°C)				
Rev	Right TCC ( $\frac{W}{m^2K}$ )	Left TCC ( $\frac{W}{m^2K}$ )	Upper Hemi CMF	Liq (PRP_072)	Belly Button Tab (PRP_51)	Upper Strut (PRP_054)	LL Strut Tab (PRP_056)	Boomerang (PRP_053)
39	150	150	1.0x	2.47	0.471	-0.743	1.298	-2.048
40	100	100	1.0x	2.47	0.471	-0.747	1.298	-1.997
41	20	20	1.0x	2.47	0.471	-0.773	1.298	-1.584
45	20	20	1.5x	2.545	0.575	-0.756	1.365	-1.049



The results for Rev. 45 looked promising, however analyzing the temperature vs. time trends showed that the model output did not match the behavior of the test data for the upper strut (PRP\_054), as shown in Figure 4.22. The temperature calculated by the model—while within a few degrees of the test data in magnitude—did not accurately reproduce the trend shown in the test data. A final conductance study on the upper struts was completed to address this deficiency.

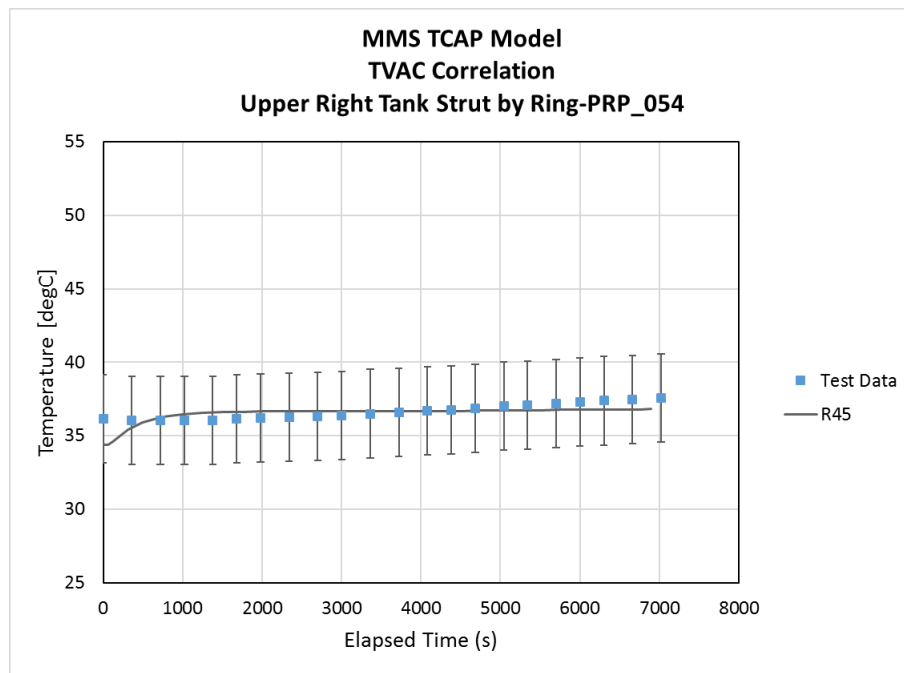


Figure 4.22: Comparison of temperature-time histories for model (line) and measurements (symbols) after Revision 45. Predicted temperature trends do not match the test data even though the magnitudes only differ a few degrees.

### 4.6.2.3 Upper Strut End Conductance Study

The final major conductance study focused on the ends of the upper struts at the interface between the strut and the temperature boundary condition set on the pin (see Figure 4.23). The goal was to address the odd behavior seen at the PRP\_054 location on the upper strut (Figure 4.22), as well as to continue to improve the correlation of the model with the test data.

Changes made to the TCC for the contact at the pin for both left and right struts were analyzed, as well as the conductance through the strut as a whole, which was defined as a grouped part (see Table A.1, Appendix A).

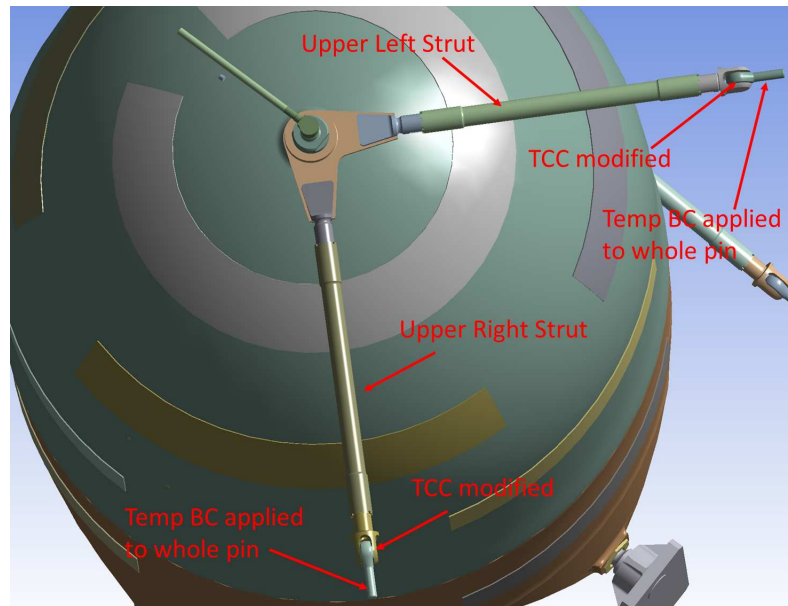


Figure 4.23: Locations on the Upper Strut Ends where conductance values (TCC) were modified.

Table 4.10 shows that as the left and right strut TCC is decreased (Rev. 42-44), the difference between the model temperature and test data at the upper right

Table 4.10: Upper Strut End Conductance Study Results

	Upper Strut TCC at Pin ( $\frac{W}{m^2K}$ )				Difference of Model Measured Temp (°C)			
Rev	Right TCC	Left TCC	Upper Right Strut CMF	Upper Hemi CMF	Liq (PRP_072)	Upper Strut (PRP_054)	LL Strut Tab (PRP_056)	Boomerang (PRP_053)
42	150	150	1.5x	1.0x	2.374	-2.482	1.315	-2.389
43	100	100	1.5x	1.0x	2.374	-2.951	1.315	-2.401
44	50	50	1.5x	1.0x	2.373	-3.757	1.315	-2.418
46	50	50	2.5x	1.5x	2.447	-3.468	1.302	-2.366
47	100	100	2.5x	1.5x	2.447	-2.686	1.302	-2.33
48	150	150	2.5x	1.5x	2.447	-2.212	1.302	-2.307

strut end location (PRP\_054) and boomerang (PRP\_053) increases. Recall that “perfect” contact is characterized by large TCC values.

This behavior means less heat is flowing through the strut in the model than in the test. Reviewing photos of the as-built tank revealed that a electrical harness was running along the upper right strut of the tank, thus providing a conductive path for heat to flow out of the tank. To account for this, the right strut conductivity was increased, and both strut TCC’s were gradually returned to their original values. At a right strut CMF of 2.5 and TCC’s set to their original, the difference in temperature at PRP\_054 and PRP\_053 was minimized (Rev. 47-48).

Table 4.10 also shows the impacts of these changes on temperatures in other places on the model. While the belly button tab (PRP\_051) was unaffected by the changes at the struts, the lower left strut tab location (PRP\_056) saw a slight decrease in temperature difference, while the liquid side location (PRP\_072) saw a slight increase. This is because slightly more heat from the bottom part of the tank is allowed to flow into the top portion of the tank and out through the upper right strut.

Analyzing the results from the study revealed that the temperature vs. time behavior shown in the test data at the Upper Strut Location (PRP\_054) could be approximated using the configuration arrived at in Rev. 48. This is shown in Figure 4.24.

While the overall temperature delta between the model output and test data is higher, the trend of the model temperature-time history is more consistent with the trend shown in the test data than in the other strut (Figure 4.22). While the

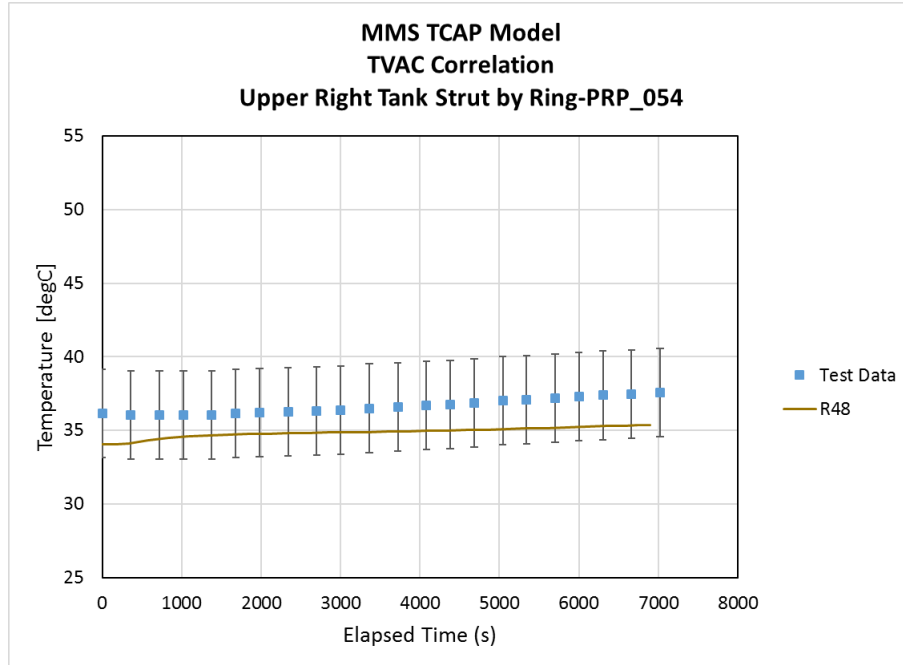


Figure 4.24: Comparison of temperature-time histories for model (line) and measurements (symbols) after Revision 48. Predicted temperature trends better match the test data even though the temperature magnitude is not in as good agreement as in Revision 45.

model still does not accurately capture the trends during the initial portion of the heating, the temperature-time trend matches the overall trend of the test data after approximately 1000s of simulation time. This result is not perfect, but adequate in that it appears to capture the major physics of the heat flux through the Upper Right Strut within the stated temperature criteria of  $\pm 3^{\circ}\text{C}$ .

#### 4.6.2.4 Final Configuration

The accepted thermal contact coefficients and conductivity multiplication factors used for the tank parts analyzed in the conductance studies are summarized

in Table 4.11. Per the log in Appendix F, additional adjustments and minor refinements/corrections were made to the thermal model, resulting in Revision 53a. This configuration of the model was accepted as the correlated thermal model. The results shown in Section 4.7 were based upon this revision and the values of TCC and CMF shown in Table 4.11.

Table 4.11: Final Conductance/Conductivity Configuration

<b>Strut Location</b>	<b>TCC (<math>\frac{W}{m^2K}</math>)</b>	<b>Location</b>	<b>CMF</b>
Upper Right at Pin	150	Upper Hemisphere	1.5x
Upper Left at Pin	150	Lower Hemisphere	2.0x
Lower Right at Tab	20	Upper Right Strut	2.5x
Lower Left at Tab	20	Upper Left Strut	1.0x
Upper Right at Boomerang	Baseline	Lower Right Strut	2.0x
Upper Left at Boomerang	Baseline	Lower Left Strut	1.0x
		Gas Inlet & Outlet Tube	1.0x
		Axial (Belly Button) Pin	1.0x

## 4.7 Final Results

The parameters identified in Table 4.11 were used to generate the following results for each of the seven locations on the propellant tank model. Figures 4.25-4.31 show the test data and model output at each sensor location. Error bars on the test data points show the envelope around the test data that indicates the  $\pm 3^{\circ}\text{C}$  acceptance criterion between measurement and prediction. Charts are organized for locations on the top to the bottom of the tank.

### 4.7.1 Gas Side Results

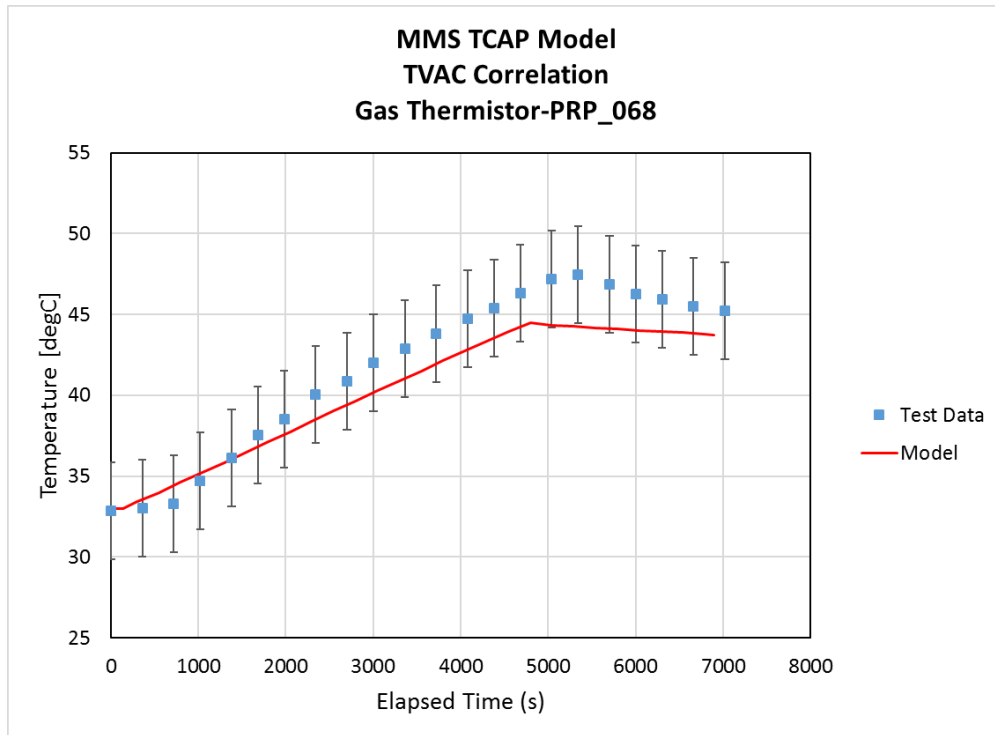


Figure 4.25: Comparison of measured (symbols) and predicted (line) temperature-time histories for the Gas thermistor location (PRP\_068). In most areas, the predicted temperature-time history lies within the acceptance criteria indicated by the ‘error bars’ on the data points.



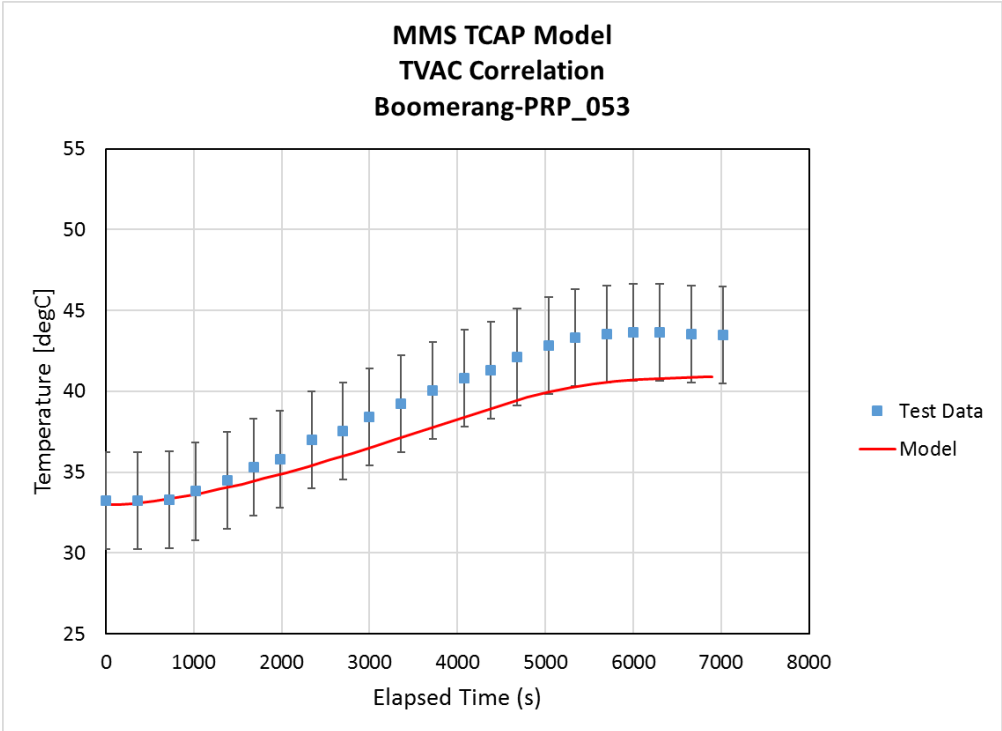


Figure 4.26: Comparison of measured (symbols) and predicted (line) temperature-time histories for the Boomerang location (PRP\_053). The predicted temperature-time history lies within the acceptance criteria indicated by the 'error bars' on the data points.

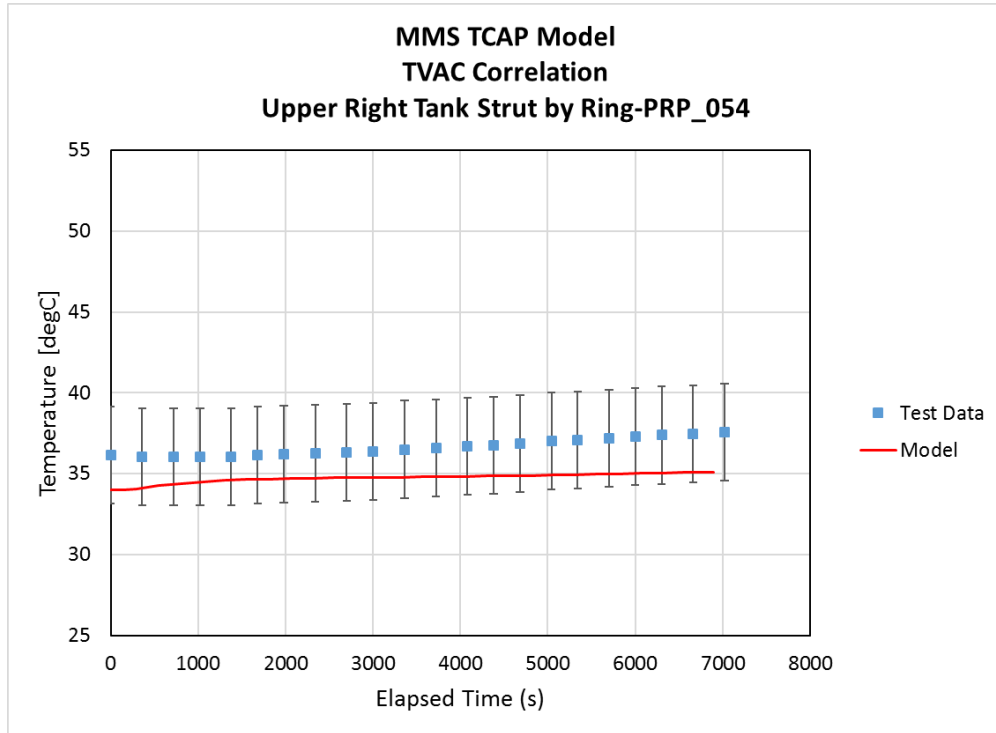


Figure 4.27: Comparison of measured (symbols) and predicted (line) temperature-time histories for the Upper Right Tank Strut location (PRP\_054). The predicted temperature-time history lies within the acceptance criteria indicated by the 'error bars' on the data points.

## 4.7.2 Liquid Side Results

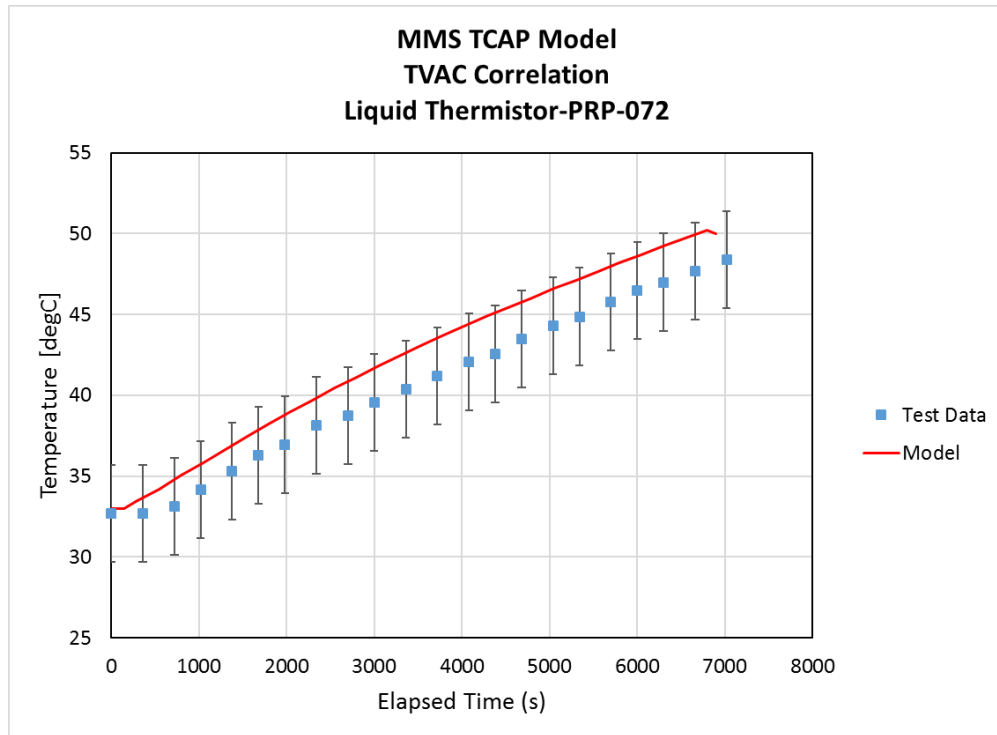


Figure 4.28: Comparison of measured (symbols) and predicted (line) temperature-time histories for the Liquid thermistor location (PRP\_072). The predicted temperature-time history lies within the acceptance criteria indicated by the ‘error bars’ on the data points.

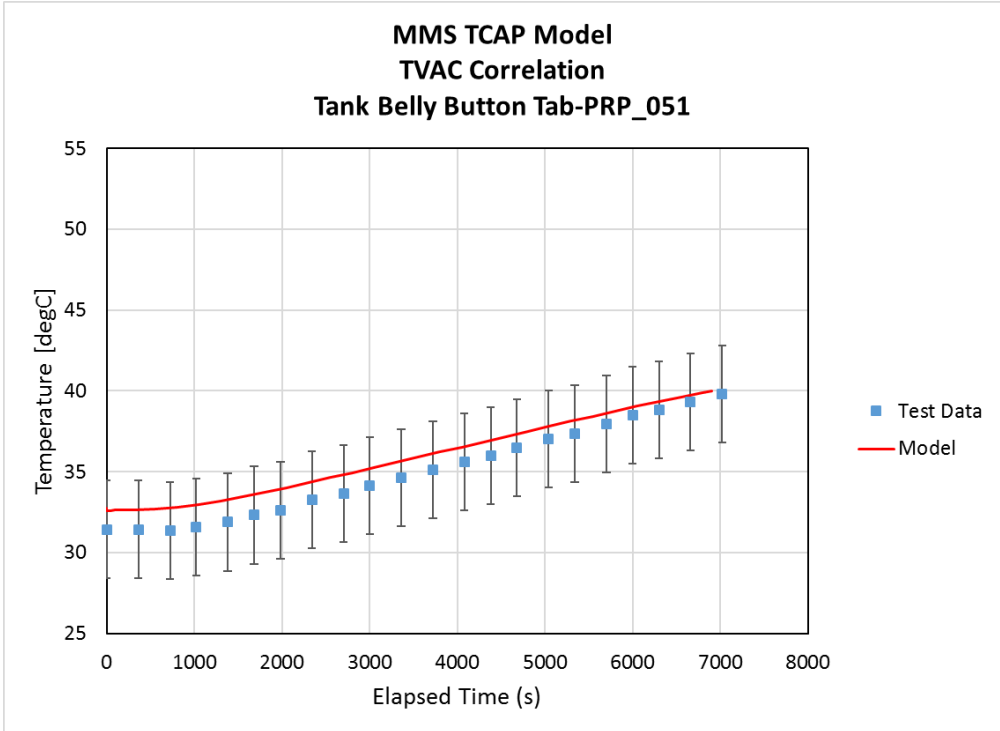


Figure 4.29: Comparison of measured (symbols) and predicted (line) temperature-time histories for the Belly Button Tab location (PRP\_051). The predicted temperature-time history lies within the acceptance criteria indicated by the 'error bars' on the data points.

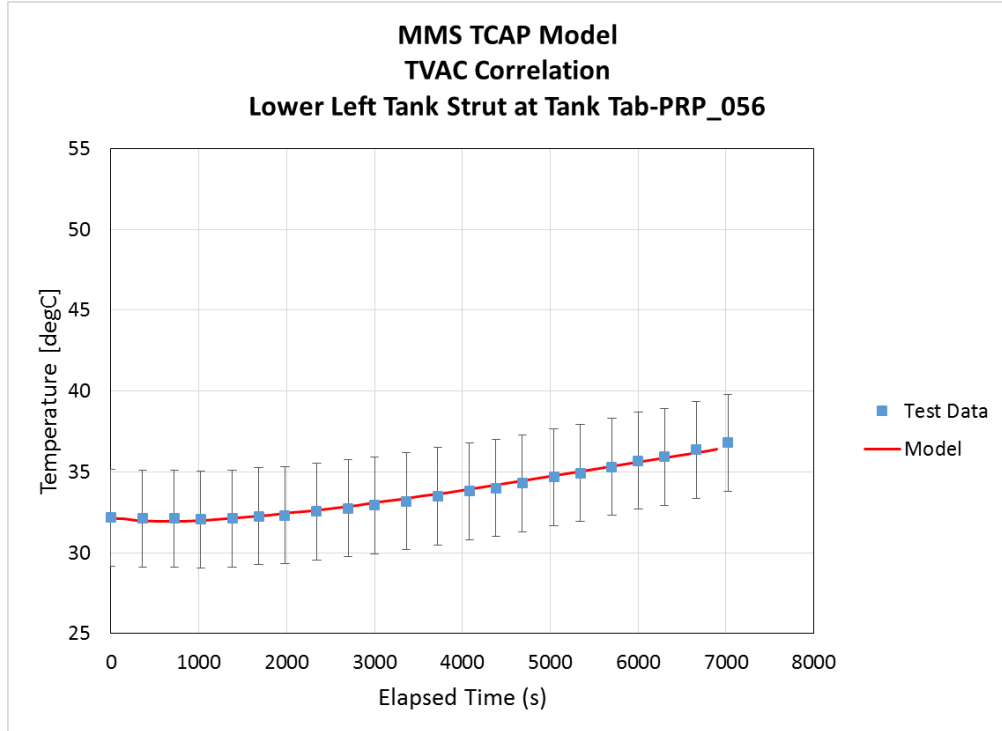


Figure 4.30: Comparison of measured (symbols) and predicted (line) temperature-time histories for the Lower Left Tank Strut at Tab location (PRP\_056). The predicted temperature-time history lies within the acceptance criteria indicated by the ‘error bars’ on the data points.

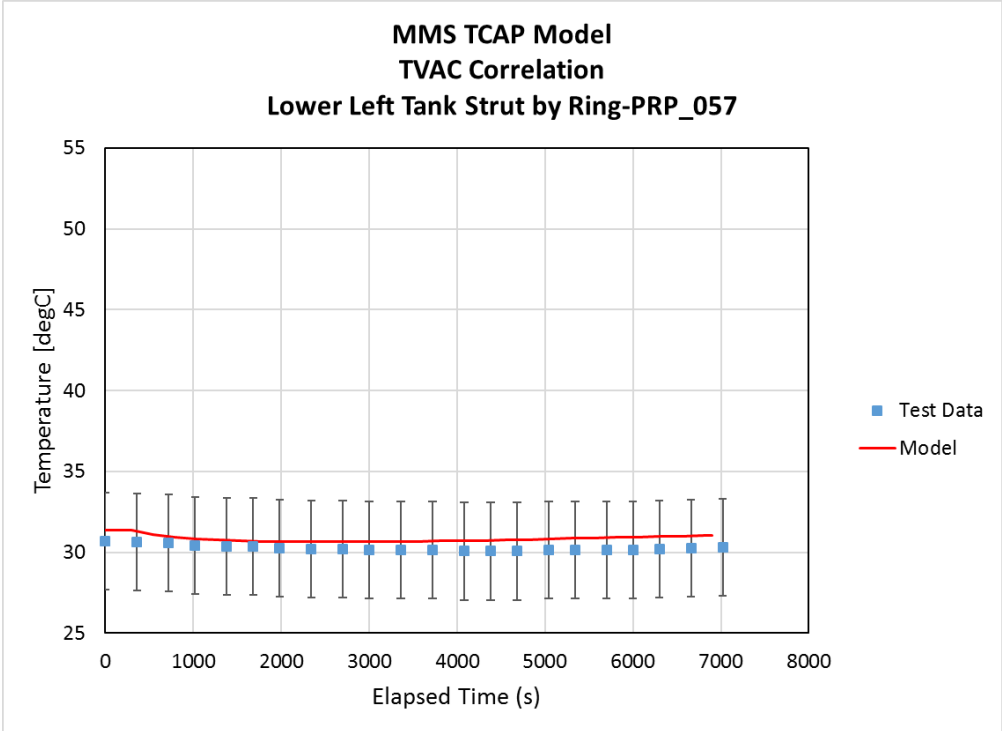


Figure 4.31: Comparison of measured (symbols) and predicted (line) temperature-time histories for the Lower Left Tank Strut by Ring location (PRP\_057). The predicted temperature-time history lies within the acceptance criteria indicated by the 'error bars' on the data points.

### 4.7.3 Discussion

#### 4.7.3.1 Gas Side Correlation Results

The model correlation to all gas side temperature locations was within the  $\pm 3^{\circ}\text{C}$  criterion. However, the gas side model results tended to under predict the TVAC test data. Reasons for this under prediction are best understood by analyzing the results for the Gas Thermistor location (PRP\_068) shown in Figure 4.25.

Predicted temperatures at the Gas Thermistor location (PRP\_068) are within the  $\pm 3^{\circ}\text{C}$  range, but slightly exceeded the limit between 5000-6000s during the model simulation. The peak temperature predicted, as well as the time of the peak, was approximately  $2.7^{\circ}\text{C}$  lower and happened approximately 900s earlier. Similar to the Gas Thermistor location, the predicted temperatures at the Boomerang (PRP\_053), shown in Figure 4.26 approached the  $-3^{\circ}\text{C}$  criterion, particularly at simulation times between 5000-6500s. Similar results are seen for the Upper Right Tank Strut by Ring (PRP\_054), shown in Figure 4.27.

Initially, this difference was thought to be due to an improperly programmed heater boundary condition, wherein the time at which the heat flux was removed in the model's programmed boundary condition did not correspond to the time the heater circuit current was removed based upon the test data. However, the boundary condition turned out to be correct.

The slopes of the temperature vs. time curve for the model and test data were also analyzed by looking at the results for PRP\_068 (Fig. 4.25). When calculated

from the beginning of the temperature rise ( $t = 500s$  of elapsed simulation time) to the peak temperature, the model had a slope of approximately  $0.15 \frac{^{\circ}C}{min}$  while the test data had a slope of approximately  $0.19 \frac{^{\circ}C}{min}$ . Slopes of all curves are lower than the test data.

The discrepancy in slope and temperature magnitudes of the predicted temperatures as compared to the test data imply that there is less heat flux in the upper hemisphere of the tank. It is thought that this lack of heat flux in the upper portion of the tank is due to the assumptions used to model the heat flux boundary condition as uniformly distributed.

Per Sections 4.3.3 and 4.6.2, the heat addition from the heater was uniformly applied to the upper and lower hemispheres of the tank and the tank CMF was increased to account for the effects of the tape covering the heaters and the tank wall. These assumptions, while sufficient to produce results that match the temperature-time behavior of the data and meet the  $\pm 3^{\circ}C$  acceptance criteria, are still approximations of the actual configuration of the tank.

The tape on the real tank, with its conductive adhesive, helps to distribute the heat from the heaters around the tank, but this distribution is not completely uniform. Heat is still localized in places near the heaters, as shown schematically in Figure 4.32(a). This means that there is a higher local heat flux near the heater and resulting temperatures at locations nearest the heaters, particularly the Gas Thermistor location (PRP\_068), will tend to be higher than at locations further away from the heaters.

The uniformly applied heat flux boundary condition, shown in Figure 4.32(b),



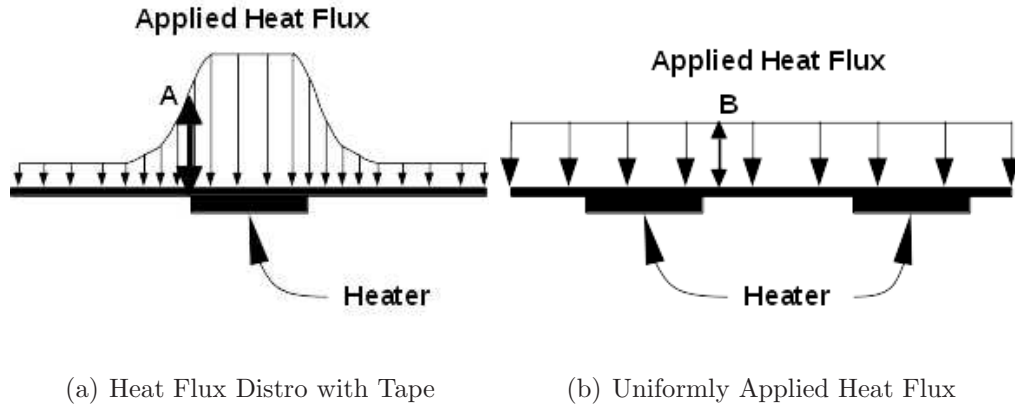


Figure 4.32: Illustrative schematics showing the heat flux from the heater covered with tape (left) compared to the uniformly applied heat flux boundary condition (right). The actual heat distribution from the heater has a higher, local heat flux (marked A) compared to the uniformly applied heat flux (marked B).

idealizes this distribution of heat, and does not account for all of the dynamics associated with the actual system of heaters and tape that exist on the real tank.

The uniformly applied heat flux boundary condition in the model removes all variation in applied heat flux magnitude around the model. This means that the heat flux near a heater location will be less than in the real case (see Figure 4.32, notations A & B), even though the magnitude of total heat flux applied to the model equals that from the heaters on the real tank.

Analyzing the physical layout of the tank, the upper hemisphere has only two conductive paths (the struts) for heat to flow from the warm tank to the cool strut interfaces, as compared to the lower hemisphere that has three conductive paths (two struts and the belly button). This means that when heat flux to the tank wall is modeled uniformly—which does not capture the affects of higher localized

heat flux as caused by patch heaters—less heat flux tends to travel out through the upper struts and instead flows toward the lower hemisphere, which contains more conductive paths to the colder tank interfaces.

The resulting temperatures at sensor locations and slope of the temperature-time curve in the upper portion of the model will therefore be lower than in the actual tank. The higher localized heat flux in the actual tank causes a larger portion of the heat flux to flow out of the struts, thus causing higher temperatures to be sensed by the 1-wire sensors and higher temperature-time slopes.

The dynamics of localized heat on the temperature results were initially considered in the model development and correlation process. As documented in Appendix F, heat flux was modeled locally from each heater for the first 26 revisions of the model. This is depicted schematically in Figure 4.33.

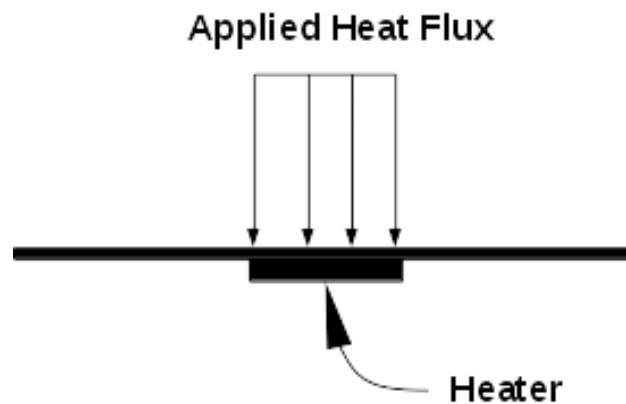


Figure 4.33: Illustrative schematic of the heat distribution initially applied to the heaters for the first 26 revisions of the model. Heat addition is only present at the heater location.

In all 26 revisions, temperature predictions at the upper and lower hemi-

spheres—particularly at PRP\_068 and PRP\_072—were much greater (5-8°C) than the test data. This was because all heat applied to the model was localized, and did not account for any distribution of heat caused by the tape. Modeling the heat flux boundary condition as discussed in Section 4.3.3 was done to better match the effect of the tape tending to distribute the heat from the heaters. Further improving how the heat addition and its interaction with the tape is modeled is the subject of future work (see Section 6.3).

#### 4.7.3.2 Liquid Side Correlation Results

The model predictions for temperature in the liquid side of the tank, like the gas side predictions, were all within the +/- 3°C criterion. The thermal model tended to over-predict the temperature results at each location, with the exception of the Lower Left Tank Strut at the Tank Tab (PRP\_056) and Lower Left Tank Strut by Ring (PRP\_057), which approximated the test data almost exactly.

Over-predictions stayed within the acceptance criterion, and temperature derivatives of the model results remained closer to those in the test data. For example, the slope of the predicted Liquid Thermistor (PRP\_072) temperatures, shown in Figure 4.28, was approximately  $0.16 \frac{^{\circ}\text{C}}{\text{min}}$ , whereas the test data had a slope of approximately  $0.15 \frac{^{\circ}\text{C}}{\text{min}}$  when calculated from the beginning of the temperature rise ( $t = 500\text{s}$  of elapsed simulation time) to the peak temperature. Figure 4.28 also shows a slight drop in predicted temperature at the last time step, meaning the model is beginning to show the effect of the heaters being turned off. This behavior, like the Gas

Thermistor (PRP\_068), happens in the model prior to when test data shows the reduction in temperature.

The model predictions of temperature at the Tank Belly Button Tab (PRP\_051), as shown in Figure 4.29, were initially higher than the model, and then gradually converged near the test data toward the end of the simulation.

Model predictions on the Lower Left Strut, both at the tab and at the Ring (PRP\_056 and PRP\_057, respectively) showed good agreement with the test data. Predictions at both locations precisely matched the slope and overall trend of the temperature vs. time curves measured by the test data.

The slightly higher temperature predictions in the liquid side temperature locations can in part be explained as an extension of the differences between how heat flux from the heaters is modeled compared to the real tank (see discussion of Gas Side Correlation results in Section 4.7.3.1). More heat flux from the upper hemisphere of the tank is moving toward the lower hemisphere since there are more conductive paths for the heat to travel out of. The greater portion of heat flux causes temperatures to be slightly higher.

Overall, the model predictions meet the acceptance criterion, indicating that the model is adequately prediction temperature-time histories on the tank.

## 4.8 Uncertainty Analysis

The temperature results predicted by the thermal model are driven by the knowledge of three main parameters: the heat flux applied to the tank via heaters,

the mass of the tank and all parts integrated on it, and the temperature boundary conditions specified at each of the strut and axial pin interfaces. An uncertainty analysis is performed to quantify and understand the impacts of each of these on the temperatures predicted by the model.

## 4.8.1 Analysis Cases

### 4.8.1.1 Heater Power

Uncertainty in the heat flux applied to the model exists due to uncertainties in the measured resistance of the heaters and the current measured by the Command and Data Handling (C&DH) computer on the spacecraft. Both the uncertainty of the measured resistance of the heaters and of the current applied to the heater circuits will impact the overall uncertainty in the heat applied to the tank.

The tank has one heater circuit that is composed of gas and liquid heater circuits that are in parallel with each other. The uncertainty in heater power going into the gas side heaters can be found as follows. Note that the same reasoning is applied to the liquid side heaters. Using Ohm's Law, the amount of heat flux ( $\frac{W}{m^2}$ ) from the gas heater can be written as:

$$q_g = \frac{(i_c R_c)^2}{R_g A} \quad (4.23)$$

Where:

$q_g$ : Heat flux into gas side of tank

$i_c$ : Current in full heater circuit

$R_c$ : Resistance of full heater circuit

$R_g$ : Resistance of gas heater circuit

$A$ : Surface area of hemisphere

The total equivalent resistance of the heater circuit is given by Eq. 4.24, which is composed of the equivalent resistance of the heaters in each individual gas  $R_g$  and liquid  $R_L$  circuit.

$$R_c = \frac{R_L R_g}{R_L + R_g} \quad (4.24)$$

Combining Eqs. 4.23-4.24 yields:

$$q_g = \frac{i_c^2 R_g R_L^2}{(R_L + R_g)^2 A} \quad (4.25)$$

Equation 4.25 is the data reduction equation for the heat flux going into the tank as supplied by the gas heater circuit. The heat flux going into the gas heaters is a function of the total circuit current and the equivalent resistances of the separate gas and liquid heater circuits. It is also a function of area; however, the uncertainty in this quantity will be taken as zero, as the heaters are manufactured with nearly identical dimensions.

The uncertainty in heater power from the gas-side heaters can be expressed as the root-sum-square of the product of the partial derivatives of each measured parameters with the uncertainty of that measured parameter within Eq. 4.25.

Following the method outlined by Coleman and Steele [34], this expression can be written as:

$$\frac{U_q}{q_g} = \sqrt{\left(\frac{i_c}{q_g} \frac{\partial q_g}{\partial i_c}\right)^2 \left(\frac{U_{i_c}}{i_c}\right)^2 + \left(\frac{R_g}{q_g} \frac{\partial q_g}{\partial R_g}\right)^2 \left(\frac{U_{R_g}}{R_g}\right)^2 + \left(\frac{R_L}{q_g} \frac{\partial q_g}{\partial R_L}\right)^2 \left(\frac{U_{R_L}}{R_L}\right)^2} \quad (4.26)$$

Where:

$\frac{U_q}{q_g}$ : Uncertainty in gas side heat flux,  $q_g$

$U_{i_c}$ : Uncertainty in full circuit current

$U_{R_g}$ : Uncertainty in equivalent gas circuit resistance

$U_{R_L}$ : Uncertainty in equivalent liquid circuit resistance

Taking the partial derivatives, substituting Eq. 4.25, and carrying out the necessary algebra, Eq. 4.26 then becomes:

$$\frac{U_q}{q_g} = \sqrt{4 \left(\frac{U_{i_c}}{i_c}\right)^2 + \left(\frac{R_L - R_g}{R_g + R_L}\right)^2 \left(\frac{U_{R_g}}{R_g}\right)^2 + \left(\frac{2R_g}{R_g + R_L}\right)^2 \left(\frac{U_{R_L}}{R_L}\right)^2} \quad (4.27)$$

The uncertainty in the full circuit current,  $U_{i_c}$ , in Eq. 4.26 is the measurement error in the current from the C&DH computer and is the sum of the full scale measurement error and the bit conversion error (Eq. 4.28). This value was found to be 0.041A.

$$U_{i_c} = 2\%FS + e_{bit} \quad (4.28)$$

The uncertainties in the equivalent gas and liquid circuit resistances— $U_{R_g}$  and  $U_{R_L}$ , respectively—in Eq. 4.27 are a function of the total measurement error from resistance readings made by an Ohmmeter during integration of each individual heater onto the tank. Both were assumed equal since the same Ohmmeter was used to measure the resistance of each heater on the tank.

These quantities are calculated via Eq. 4.29:

$$U_{R_g} = U_{R_L} = \frac{1}{N \left( \frac{1}{\Delta R_{wrst}} \right)} \quad (4.29)$$

Where:

$N = 7$ : Number of heaters in the specific gas/liquid circuit

$\Delta R_{wrst} = 2.5\Omega$ : Worst-case resistance measurement accuracy of the Ohmmeter

Equations 4.27-4.29 were applied to the gas and liquid side heat flux (Eq. 4.25) using the nominal values of resistance. The circuit current,  $i_c$ , in Eq. 4.27 was taken as the average current measured over the entire time period of the over-temperature thermostat test. The resulting uncertainty in gas and liquid side heat fluxes was found to be 9.6%. This uncertainty was applied to the nominal heat flux calculated for each heater circuit, forming a Q+ and Q- heat flux cases. These bounding values of heat flux were programmed into ANSYS and the solution re-calculated. Results are shown in Section 4.8.2.

#### 4.8.1.2 Tank Mass

Uncertainty in the mass of the tank and all of the parts integrated on it was calculated based on the accuracy of the load cell used to measure the mass of the tank during installation. Mass uncertainty factors into the overall heat capacitance of the system and ultimately how the tank responds to the thermal loads applied to it.

The load cell used during the installation of each propellant tank had a mea-



surement error that resulted in a +/- 1.13kg uncertainty on the propellant tank mass measurement. The total mass of the model was proportionally increased and decreased by this value, with temperature solutions generated for each case. Results are shown in Section [4.8.2](#).

### 4.8.1.3 Temperature Boundary Conditions

Uncertainty also exists in the temperatures used to define the boundary conditions at the tanks interfaces to the rest of the spacecraft. In flight, there will be limited temperature telemetry at the tank interfaces to the rest of the spacecraft, leading to large uncertainties as to the overall thermal behavior of the tank strut interfaces.

Uncertainties in the assigned temperature boundary conditions were analyzed by modifying the nominal assigned boundary temperatures (see Appendix [B](#)) by +/- 10°C. The thermal model was run for each case, and results are shown in Section [4.8.2](#).

## 4.8.2 Uncertainty Analysis Results

Tables [4.12-4.14](#) and Figures [4.35](#) and [4.34](#) show the effects of the uncertainty of each case on the temperatures predicted by the model. For brevity, these tables show the difference in temperatures of each uncertainty case from the nominal temperature predicted by the model ( $\Delta T_{nom}$ ). The tables also show the percent deviation from the nominal temperature, and the sensitivity coefficient,  $C_s$ . The

sensitivity coefficient is defined as the ratio of  $\Delta T_{nom}$  to the difference of the parameter being studied from its nominal value,  $\Delta P_{nom}$  (i.e.  $Q^+ - Q_{nom}$ ). This is shown by Eq. 4.30.

$$C_s = \frac{\Delta T_{nom}}{\Delta P_{nom}} \quad (4.30)$$

Temperatures were taken at the second to last time step for the Gas (PRP\_068) and Liquid (PRP\_072) sensor locations, and at the last time step for all other locations.

Table 4.12: Heater Power Uncertainty Study Results

<b>Location</b>	<b>Q + (<math>\Delta T_{nom}</math>)</b>	<b>Q - (<math>\Delta T_{nom}</math>)</b>	<b>Percent Deviation</b>	<b><math>C_s</math></b>
Gas (PRP_068)	1.102	1.000	2.517	0.582
Boomerang (PRP_053)	0.799	0.764	1.954	0.422
Upper Strut (PRP_054)	0.033	0.035	0.094	0.017
Liq (PRP_072)	1.515	1.821	3.018	0.799
Belly Button Tab (PRP_051)	0.728	0.777	1.821	0.384
LL Strut Tab (PRP_056)	0.416	0.442	1.143	0.220
LL Strut by Ring (PRP_057)	0.02	0.019	0.064	0.011

Table 4.13: Tank Mass Uncertainty Study Results

<b>Location</b>	<b>M + (<math>\Delta T_{nom}</math>)</b>	<b>M - (<math>\Delta T_{nom}</math>)</b>	<b>Percent Deviation</b>	$C_s$
Gas (PRP_068)	0.601	0.648	1.373	0.573
Boomerang (PRP_053)	0.506	0.552	1.238	0.488
Upper Strut (PRP_054)	0.045	0.054	0.128	0.048
Liq (PRP_072)	0.829	0.888	1.651	0.786
Belly Button Tab (PRP_051)	0.475	0.533	1.188	0.472
LL Strut Tab (PRP_056)	0.354	0.413	0.973	0.365
LL Strut by Ring (PRP_057)	0.028	0.035	0.090	0.031

Table 4.14: Temperature Boundary Condition Uncertainty Study Results

<b>Location</b>	<b>T + (<math>\Delta T_{nom}</math>)</b>	<b>T - (<math>\Delta T_{nom}</math>)</b>	<b>Percent Deviation</b>	$C_s$
Gas (PRP_068)	0.789	0.3	1.802	0.079
Boomerang (PRP_053)	0.975	0.7	2.385	0.098
Upper Strut (PRP_054)	5.055	5.114	14.400	0.506
Liq (PRP_072)	0.335	0.7	0.667	0.034
Belly Button Tab (PRP_051)	3.182	3.25	7.961	0.318
LL Strut Tab (PRP_056)	1.036	1.071	2.846	0.104
LL Strut by Ring (PRP_057)	7.468	7.53	24.046	0.747

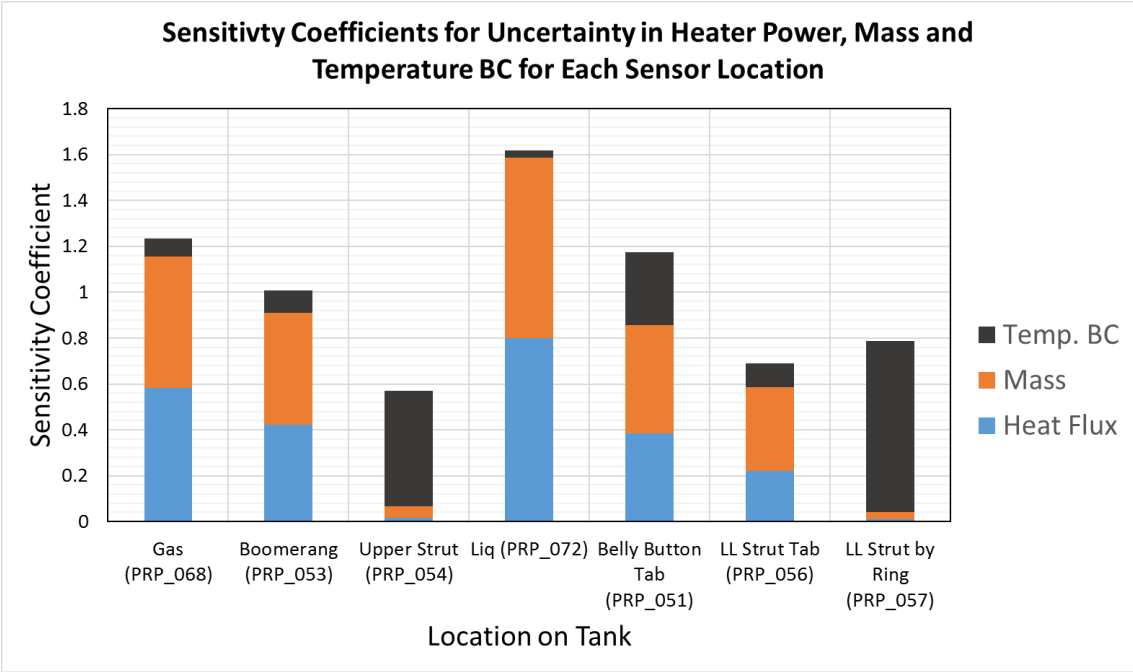


Figure 4.34: The chart shows the sensitivity coefficient,  $C_s$ , of each parameter studied at each sensor location on the tank. Results at the majority of sensor locations are sensitive to uncertainties in applied heat flux and mass. Sensors located nearest the tank interfaces show greater sensitivity to uncertainties in applied Temperature BC.

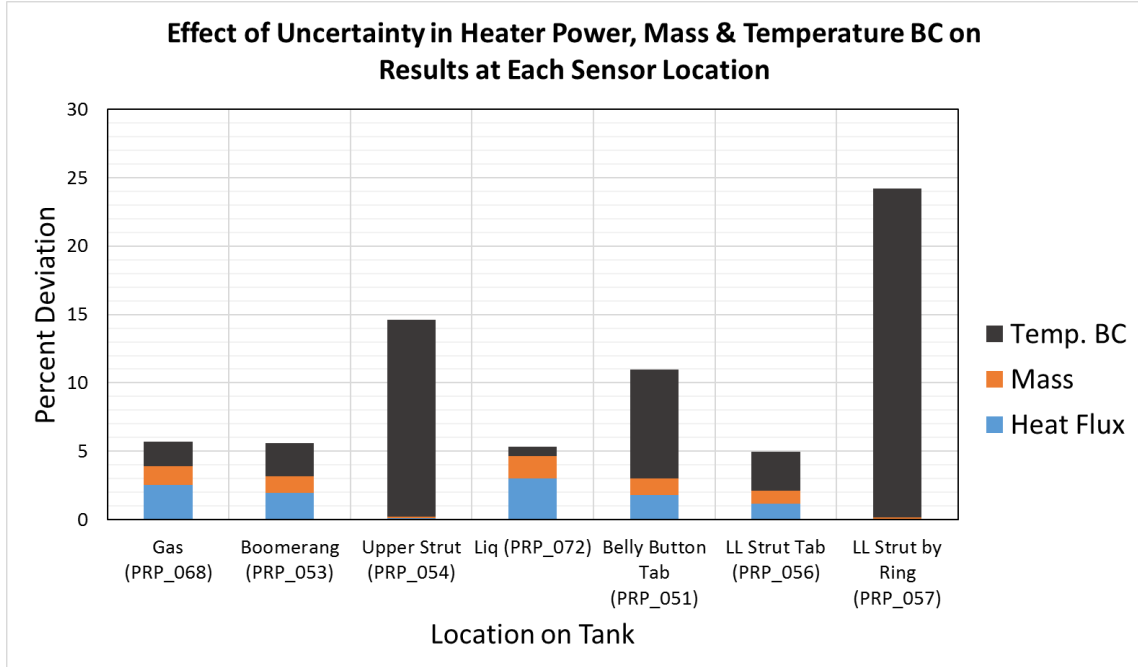


Figure 4.35: The chart shows the percent deviation of each parameter studied at each sensor location on the tank. The percent deviation due to uncertainties in Temperature BC applied to the tank interfaces are very large at locations near those interfaces (i.e. PRP\_057).

### 4.8.3 Discussion

The uncertainty analysis shows that uncertainties in all three parameters—applied heat flux, mass, and temperature boundary condition—impact the temperature predictions of the model, but in different ways.

Figure 4.34 shows the sensitivity coefficients at each sensor location on the tank. The chart shows that the temperature predictions at the majority of the locations, particularly a locations away from strut interfaces, are sensitive to uncertainties in applied heat flux and mass. This is shown by the large  $C_s$  at these

locations, particularly at the Gas (PRP\_068) and Liquid (PRP\_072) Thermistor locations. Temperature predictions at these locations are not particularly sensitive to uncertainties in the magnitude of the temperature boundary condition.

Model predictions near the strut interfaces, however, show a large sensitivity to uncertainties in temperature boundary condition, particularly at the Upper Strut (PRP\_054) and Lower Left Strut (PRP\_057) locations.

The results shown in Figure 4.34 imply that the greatest variability in predicted temperatures will occur at locations away from the strut interfaces due to uncertainties in applied heat flux and mass, and at locations near the strut interfaces due to uncertainties in temperature boundary condition.

When the percent deviation at each location is plotted (Figure 4.35), however, it can be seen that the greatest variability in predicted temperatures occur not due to uncertainties in heat flux or mass, but due to uncertainties in applied temperature boundary conditions at the strut interfaces.

Uncertainties in heat flux and mass have a relatively small effect on predicted temperatures, despite having larger sensitive coefficients, as shown in Figure 4.35. Analyzing the effects at the Gas and Liquid Thermistor locations show that a change in heater power of 10% translates to a temperature change at these locations of approximately 1°C at PRP\_068 and 1.8°C at PRP\_072.

An uncertainty in mass from the load cell affects predicted temperatures by a maximum of approximately +/- 0.9°C per kilogram of mass uncertainty. Both uncertainties in heat flux and mass affect temperatures predicted at all sensor locations to within the same order of magnitude. This contrasts with the effect of

uncertainties in temperature boundary conditions.

Uncertainties in the specified value of the temperature boundary conditions were found to significantly impact the predicted temperatures, particularly of the Upper and Lower Struts and Belly Button Tab (Fig. 4.35). The drastic effects of temperature at the tank interfaces makes sense because there is a much higher magnitude of heat flux induced when the temperature difference between the strut end and specified boundary condition is greater.

A high uncertainty in temperature boundary conditions will mean the model will not accurately predict the temperatures at locations near those boundary conditions. However, Table 4.14 shows that the model will still provide reasonably good temperature predictions at locations away from the strut interfaces, such as at the gas and liquid sensor locations.

The overall effect of these uncertainties on the future predictions of mass will still need to be quantified, as data does not yet exist to make comparisons to characterize these effects. This will be the subject of future work.

## Chapter 5: Phase III: Using the Thermal Model to Estimate EOL Propellant Load

While beyond the scope of this thesis, it is worth explaining how the correlated thermal model will be used to estimate propellant load aboard the MMS spacecraft.

### 5.1 Part A: Model Refinements Using Commissioning Data

The Phase II correlated thermal model will be refined and calibrated using flight data from the MMS spacecraft that were acquired when the propellant tanks were fully loaded. This is expected to be necessary because the propellant mass contained within the tanks will limit the thermal gradients on the propellant tank (see Section 2.1). This step is important for improving the model's accuracy and suitability for prediction of EOL propellant loads.

### 5.2 Part B: Mid-Mission Orbit Change Propellant Gauging

Halfway through the mission in the 2017 time frame, a series of thruster burns will be performed to change the orbit of the MMS constellation so that the MMS constellation passes through the magnetotail region of the magnetosphere. This



mid-mission orbit change will deplete approximately half of the propellant. Prior to and after this burn, the calibrated propellant gauging model will be used to estimate the propellant within the tanks. Flight data from this period will also be used to make further refinements to the model.

Propellant load predicted using the TCM, bookkeeping, and PVT methods will be compared. Since approximately half of the propellant will be consumed, the accuracy of the bookkeeping and PVT methods should still be relatively high and provide a good reference for the TCM method. However, it is important to keep in mind that the accuracy of the TCM should still be relatively low in comparison to the other methods, but nevertheless improved from the estimations made in Part A since the mass of propellant remaining in the tank will be lower, leading to larger and thus easier to measure thermal gradients on the tank wall.

### 5.3 Part C: End of Life Propellant Gauging

After both Parts A & B are completed, the model will be ready to predict the EOL propellant load on the MMS spacecraft. At this point in the mission, the accuracy of the TCM gauging will be approaching a maximum since the amount of mass within the propellant tank is at a minimum, meaning that a large portion of the heat is being stored in the tank wall, rather than in the propellant. Larger thermal gradients will exist on the tank, therefore increasing the slope of the temperature vs. time curve.

EOL propellant estimates will again be compared with both bookkeeping and

PVT methods. In addition, the estimates made previously in Parts A & B will be used to analyze trends in propellant estimation throughout the life of the spacecraft. This means that an overall higher accuracy EOL propellant estimation may be made by reducing uncertainty with the TCM estimate and model.

## 5.4 Approximate Time Line

Parts A-C described previously will take place over a time frame of approximately 1-1.5 years. This time period is primarily driven by the MMS mission life and operations. Figure 5.1 shows an estimated time line of when each part of Phase III will occur. The approximate time frames for when the mid-course correction will occur and EOL period of the mission are shown.

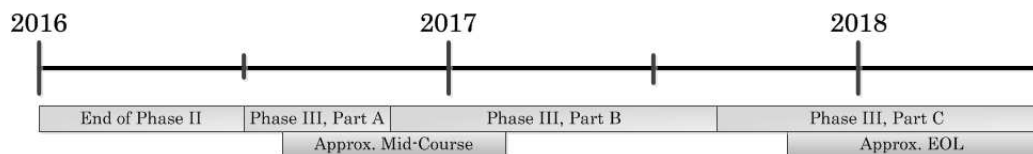


Figure 5.1: Phase III will approximately coincide with major parts of the MMS mission.

## Chapter 6: Conclusion, Issues, Lessons Learned & Future Work

### 6.1 Thesis Conclusion

The objective of this thesis is to develop and correlate a thermal model of the MMS propellant tank that is capable of predicting temperature-time histories, and can be used to make future predictions of propellant load as discussed in Chapter 5. The results presented in Section 4.7 show that the thermal model developed and correlated for this project was able to predict temperatures within  $\pm 3^{\circ}\text{C}$  of thermal vacuum test data at each sensor location, meeting the acceptance criteria defined in Section 1.4. Therefore, the model is sufficient to be used to make future predictions of propellant load within the MMS spacecraft as described in Phase III, meeting the objective of this thesis.

The predictions of temperatures made by the thermal model on the gas portion of the tank were lower than the test data, and temperature predictions on the liquid portion of the tank were higher than the test data. The under-predicted temperatures are thought to be caused by less heat flux in the upper portion of the tank, and greater heat flux in the lower portion of the tank.

The model was also found to be relatively sensitive to uncertainties in applied heat flux and overall mass. An uncertainty of 10% in heat flux translated to

approximately 1-2°C differences in temperatures located nearest the applied heat flux boundary condition, specifically at the gas (PRP\_068) and liquid (PRP\_072) locations. The model showed a difference in predicted temperatures of approximately 0.9°C for 1kg of uncertainty in total tank mass. Temperature predictions near locations of assigned temperature boundary conditions were greatly impacted by uncertainties in the specified temperature. The model greatly under or over predicted temperatures at locations on the strut ends and belly button tab when the assigned temperature boundary condition value was changed. However, temperature predictions at locations away from the strut ends and tabs were only slightly affected.

Though the model was able to be correlated within the defined temperature tolerance, a number of issues remain. The high fidelity of the CAD model and complexity of ANSYS made it difficult to simplify and correlate the model. Limitations in controlling the conductivity of grouped parts also hindered the correlation process. Finally, the cause of the discrepancy in temperature slopes between the model output and test data on the gas side of the tank need further investigation, and better methods of applying conductances to the model need to be implemented.

## 6.2 Issues & Lessons Learned

### 6.2.1 Issues

#### 6.2.1.1 Complexity of the Model

The ANSYS software is a powerful tool that is capable of modeling the finest details of systems. This allows for highly accurate predictive models to be generated. The ability of ANSYS to account for large levels of detail lead to the approach taken in Phase I, which was to directly import the fully detailed CAD model of the Flight Tank into ANSYS. The thinking was that including every part of the tank would produce an accurate model which, in turn, would lead to accurate propellant estimations.

The “costs” of this approach are the need to know the details of every facet of the system being modeled, and an extremely complex mesh and overall ANSYS thermal model. The effects of this were felt primarily in the correlation phase of the project where the model was adjusted to match actual test data. These challenges did not appear as readily in Phase I, which relied on other thermal models for verification. The main problems were with the solid body contacts and the overall solve time.

Even after de-featuring the model as much as possible, the resulting solid model still had a relatively high level of detail. The struts, for example, were reduced from approximately 15 parts (totaling in 14 contact pairs) to four parts. These four parts still required contact information for each of the three contact pairs

that made up the strut assembly. The detailed information on these contacts was not known during MMS integration. Furthermore, money and time did not exist to conduct the tests required to determine what the actual conductance was at each contact pair. This problem is recognized by thermal analysts, and hence modifying the thermal conductance within a part/assembly is used to account for all of the inherent unknown factors within a system to correlate models to test data.

The analysis method of modifying thermal conductance of parts was applied to this project. However, these efforts were hindered by the level of detail needed by ANSYS. While ANSYS does allow parts to share a mesh, which effectively turns multiple parts into one continuous part, this method was found to have problems with modeling heat transfer. Initial modeling efforts using the built-in controls for sharing meshes produced results that showed that heat was not being properly transferred between parts that supposedly shared a mesh. Multiple attempts to solve this problem with the model were attempted, but with no success.

The method of grouping parts using bonded contacts and finding thermal properties based upon the mass fraction (see Section [4.2.3.2](#)) was used to overcome the issues with shared-meshes. This resulted in its own challenges, namely losing the ability to control the conductance of the grouped part directly, which led to modifying the grouped part conductivity (see Section [4.2.3.2](#)). This solution was not ideal, and made the correlation process even more complicated.

### 6.2.1.2 Solve Time

The detail present in the ANSYS model directly impacted the complexity of the mesh required, which in turn impacted the solve time of the model. Even after removing small parts like bolts and washers, the tank mesh contained thousands of nodes. Multiple iterations to reduce the mesh size without impacting quality were done prior to the first correlation process revision. Success was limited because the imported geometry of the tank itself, with its complicated, non-symmetric shapes, and thin parts, required a non-uniform mesh to be generated. Non-uniform meshes drastically increase the number of nodes required to resolve details, which is advantageous for meshing complex geometries like the solid model of the tank used in this project. However, this same geometry means that square meshes, which are primarily uniform and contain far fewer nodes, are not able to be utilized since they cannot capture the details of more geometrically complex shapes.

The complex shapes contained in the detailed solid model of the tank meant that non-uniform meshing had to be utilized on the majority of parts, therefore increasing the number of nodes in the system. Efforts to reduce the mesh complexity were limited, since thermal error (see Section 4.5.2 and Appendix E) would tend to greatly increase throughout the model, causing thermal undershoot, inaccurate heat flux modeling, and myriad of other problems.

The complex geometry and corresponding mesh ultimately meant that the solve time of the model was long. Using the base-mesh (see Section 4.5.2), each run took approximately 45 minutes to completely solve. For comparison, the entire MMS

spacecraft thermal model, which was developed by the MMS Thermal Subsystem Team using Thermal Desktop, took approximately half the time to solve. The Thermal Desktop model had greatly reduced geometric complexity, allowing for a much more basic mesh to be utilized, which in turn allowed for a much shorter solve time. The Thermal Team was able to successfully correlate the spacecraft thermal model [35].

## 6.2.2 Lessons Learned

The following are the main lessons learned from the correlation of the MMS tank thermal model. These are based on the above section, as well as from the process of completing this project.

- **Reduce the complexity of the solid model**

Reducing the complexity of the solid model directly results in a less complicated correlation process, and faster solve times by requiring a less complex mesh. Changes to the models conductance values and the impacts those have on the model response can therefore be seen more clearly and faster, since solve times are less. More control can be achieved by adding complexity, rather than working backwards to reduce complexity, only to have to re-introduce it later.

- **Understand how the software queries results from the solid model**

Temperatures in the ANSYS model were ultimately queried by defining a patch area and taking an area-weighted average of the results on that patch (see



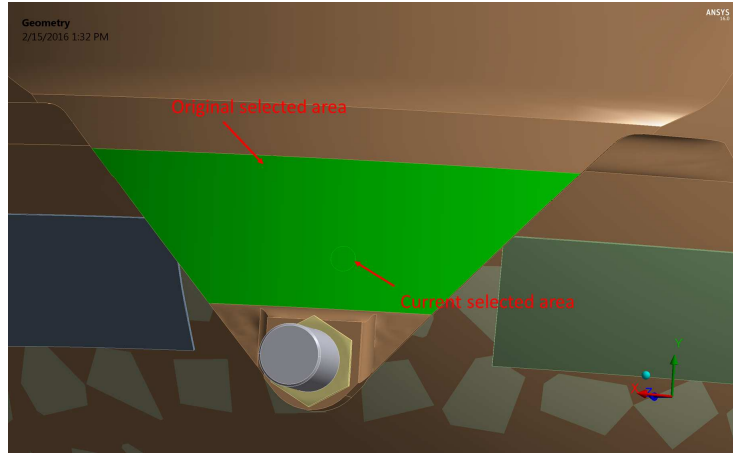
Section 4.5.3). Initially, this was not done. For about half of the correlation process, temperatures were returned from relatively large selected areas. At the time, it was thought that the Temperature Probe tool in ANSYS, which returns temperature results from selected points, lines, areas and bodies, was averaging nodal results on a selected entity. However, it was discovered that the Probe Tool returns the *maximum* temperature from a face (see Revision 33, Appendix F).

For most locations on the model (like PRP\_068), this was not a problem, since the selected area was small, and the temperature gradient across the area was also small. However, this was not the case on larger selected areas, such as the belly button tab (PRP\_051). As shown in Figure 6.1, the area originally selected for this area was large, along with the resulting temperature gradient.

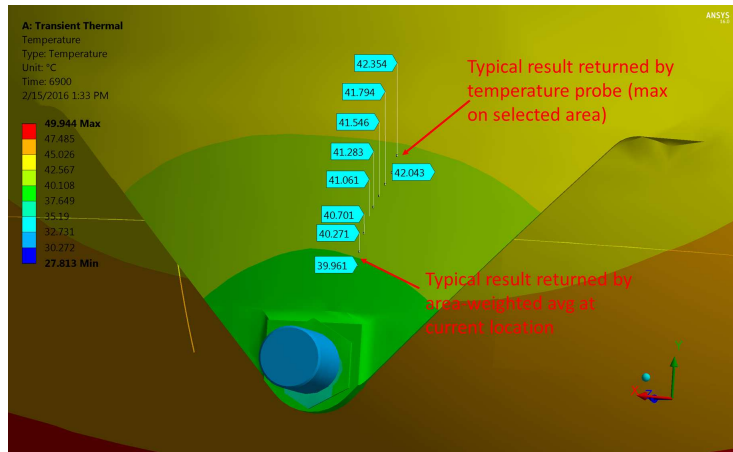
The results originally queried from the selected area at PRP\_051 were returning the maximum temperature value, which was both located farther from the actual location of the 1-wire sensor, and had a much higher temperature due to the large thermal gradient.

Once this error was discovered, all temperature query locations were changed to smaller areas and a script was written to query temperatures using an area-weighted average (see Appendix D). This algorithm accounts for the small temperature gradient on the smaller area. This change improved the overall accuracy of the returned results.

- **Document changes to model and corresponding results in one place**



(a) Query Areas



(b) Temperature Gradient

Figure 6.1: The area initially selected (Fig. 6.1(a)) to query temperature results was large and therefore the temperature gradient present on the surface skewed results (Fig. 6.1(b)). Once the area was revised to coorespond with the as-built 1-wire location, temperature results were more inline with measured data.

While each change made to the thermal model was recorded (see Appendix F), the original change log could have been organized in a more efficient manner. The correlation process involved making a specific change, running the model, and then analyzing the results to see how the change impacted the heat transfer and

temperatures within the model. This analysis was primarily completed by plotting the results in Excel. While this method was useful, it did not easily allow for cumulative trends to be seen from run to run. Graphs from previous runs could be viewed, but this did not allow for the effects of changes at other locations to be easily compared to the results at all locations and from previous iterations.

### 6.3 Future Work

- **Implement an iterative method to correlate model.**

The correlation process presented in Section 4.6 primarily relied on the analyst's understanding the heat transfer physics of the problem, and observing how the system changed with differing inputs of TCC and CMF. While this method was sufficient for this problem and is an acceptable practice for an engineering analysis of this kind with limited input variables, a more robust method and approach using a numerical optimization scheme should be used in the future to correlate the model.

The goal of this iterative scheme would be to minimize the error between the temperature predicted by the thermal model and the temperature from the test data at a given location on the model. This would be accomplished by modifying a set of control variables. In this case, the control variables would be the thermal resistances (effectively TCC or CMF for this problem) at different locations around the tank.

This error can be defined in different ways. One way to define the error is the difference between the predicted temperature,  $T_m$ , and the temperature measured

during the TVAC test,  $T_{test}$ , taken at the last time step in the simulation and normalized by  $T_{test}(t_{end})$ . This definition is shown in Eq. 6.1.

$$\epsilon = \frac{T_m(R_1, R_2, \dots, R_j, t_{end}) - T_{test}(t_{end})}{T_{test}(t_{end})} \quad (6.1)$$

The predicted temperature,  $T_m$ , in Eq. 6.1 is a function of each thermal resistance defined in the model. This value would be found by solving the thermal model for each given value of  $R_j$ .

One technique that could be employed to minimize the error,  $\epsilon$ , is Newton's method. For the 1-dimensional case, the appropriate value of  $R_{k+1}$  that minimizes the error,  $\epsilon$ , can be determined using the following relation [36]:

$$R_{k+1} = R_k - \frac{\epsilon(R_k)}{\epsilon'(R_k)} \quad (6.2)$$

In Eq. 6.2,  $R_k$  is the current estimate of the thermal resistance that minimizes error, and  $\epsilon'(R_k)$  is the derivative of the error function defined with respect to  $R_k$ . To apply Newton's method to account for multiple input parameters,  $R_k$ , Eq. 6.2 can be generalized for the n-dimensional case by replacing the derivative with the Jacobian [37], which can be expressed as:

$$E'_{ij} = \frac{\partial \epsilon_i}{\partial R_j} \quad (6.3)$$

where  $E_i$  is the  $i^{th}$  element in the error function array of n-dimensions, and  $R_j$  is the  $j^{th}$  element of the thermal resistance parameter array of n-dimensions. The partial derivatives in the Jacobian can be approximated using a numerical finite difference scheme, such as a first order forward difference.

In the project described herein, Newton’s method would be applied to find the set of thermal resistances,  $R_k$ , that minimized the error between the calculated temperature and measured temperature at a given location on the model. Since the definition of error in Eq. 6.1 is dependent upon a solution to a complex physical system (i.e. the tank thermal model), instead of finding where the function,  $\epsilon(R_k)$ , was zero, a convergence criterion,  $C_a$  based on the model’s acceptance criterion of +/- 3°C may be used. Equation 6.2 is modified as follows to account for the convergence criterion:

$$R_{k+1_j} = \frac{C_a - \epsilon(R_{k_j})}{E'_{ij}(R_{k_j})} + R_{k_j} \quad (6.4)$$

The analyst would provide an initial guess of the thermal resistance at each location on the tank, solve the model, compute the Jacobian and errors at each location of interest, and then calculate the predicted resistance  $R_{k+1}$  using Eq. 6.4. The values of  $R_{k+1}$  would then serve as the initial guess for the next iteration. This process would be repeated until the convergence criterion,  $C_a$ , is met. Figure 6.2 shows an illustrative example of this process for the first few iterations.

This iterative method, while straight forward in concept, is complicated by the fact that the problem is unsteady. The Jacobian is a function of time, and would likely require its own iteration process to calculate at each time step. The thermal system modeled, despite its numerous simplifications using the TCC and CMF, is complex in nature, and such an iterative solution method may have convergence problems or yield  $R_k$  values that are unrealistic. Despite these drawbacks and challenges, an iterative method of this nature is worth investigating for use in future

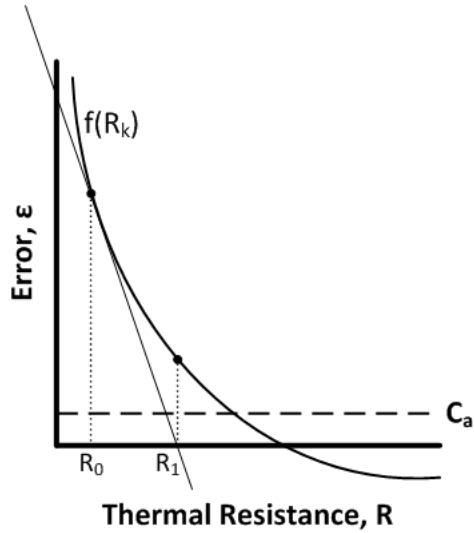


Figure 6.2: Illustration of Newton's method where error,  $\epsilon$  is minimized to the convergence criterion,  $C_a$ , for different parameters of thermal resistance,  $R$ .

Phases of this project.

- **Further refine the heat flux boundary condition to improve temperature predictions throughout the model, particularly in the upper hemisphere.**

The temperature predictions for the Gas Side of the propellant tank were shown to be within tolerance, but under-predicted the test data (see Section 4.7). This under-prediction was stated to likely be caused by how the heat flux from the heaters and interaction with the tape was modeled. Further refinements to how local heat flux from the heaters and how it is distributed by the tape should be made to correct this lack of localized heat flux in the tank. These refinements can include further conductivity studies with the tank CMF.

- **Start Phase III of project**

Phase III of the project, which involves the validation of the model using flight data, is the next major task to be completed. In this Phase, the model will be compared to flight data, and correlated to match the current state of the tank system within the tank. Phase III also will also perform the initial propellant gauging predictions of the propellant remaining in the propulsion system. These predications can be compared to both bookkeeping and PVT methods to bound the results. Initial estimations on uncertainty in the TCM propellant gauging will also be addressed. See Chapter 5 for more details.

- **Address model complexity by switching to Thermal Desktop Implementation**

The complexity of the solid CAD model of the tank, and the resulting complexities that resulted in the ANSYS program itself should be addressed for future implementations of this project. One method to address this would be to switch the analysis software from ANSYS to Thermal Desktop. Thermal desktop allows for basic and even complex geometries to be imported and modeled. It also allows for better control over specifying thermal conductance between parts. This will help reduce some of the issues discussed in Section 6.2.1.1, specifically the need for forming of grouped parts.

- **Add more of the spacecraft structure to account for uncertainties in tank temperature boundary conditions**

The current thermal model of the propellant tank does not include the details of the surrounding spacecraft structure (see Section 4.2.2). This simplification was made since there were ample 1-wire sensors at key locations around the tank during the TVAC test that allowed for temperature knowledge of the tank interfaces to be known. These 1-wire sensors, however, do not return telemetry in flight, and therefore the temperatures at the strut ends will not be known at the same fidelity as during the TVAC test. Results from the initial model validations done in Phase III will help determine how much more of the structure surrounding the spacecraft will need to be modeled to fully capture the thermal boundary conditions around the propellant tank.

- **Analyze impact of convection within fluid of tank during Phase III**

The current thermal model assumed that convection within the gas inside of the tank did not play a major role in the heat transfer of the tank system during the thermal vacuum test (see Section 4.2.2). While this assumption is justified for this model configuration, the propellant tank on orbit is filled with both liquid propellant and pressurant gas. The two are separated by the diaphragm. An analysis at the beginning of Phase III should be completed to determine the extent to which convection plays a role in both the fluid and gas within the tank system on orbit, and how this impacts the overall heat transfer of the system.



## Chapter 7: Acknowledgements

The author would like to thank and acknowledge the following individuals who provided invaluable time, experience and guidance such that this project could be completed.

- **Dr. Christopher Cadou**, Department of Aerospace Engineering, University of Maryland (Advisor & Committee Chair)
- **Dr. Eric Cardiff**, Code 597 Propulsion Branch, Goddard Space Flight Center (NASA Advisor)
- **Dr. Raymond Sedwick**, Department of Aerospace Engineering, University of Maryland (Committee Member)
- **Dr. Bao Yang**, Department of Mechanical Engineering, University of Maryland (Committee Member)
- **Sunil Acharya**, Mallett Technologies
- **Chris Anders**, Code 540 Mechanical Systems Division, Goddard Space Flight Center
- **Mike Commons**, Code 545 Thermal Branch, Goddard Space Flight Center

- **Eric Grob**, Code 545 Thermal Branch, Goddard Space Flight Center
- **Jong Kim**, Code 545 Thermal Branch, Goddard Space Flight Center
- **Paul Mason**, Code 591 Attitude Control Systems Engineering Branch, Goddard Space Flight Center
- **Joe Miller**, Code 597 Propulsion Branch, Goddard Space Flight Center
- **Mike Rife**, Mallett Technologies
- **Jason Solimani**, Code 545 Thermal Branch, Goddard Space Flight Center
- **Eric Stoneking**, Code 591 Guidance, Navigation and Control Systems Branch, Goddard Space Flight Center
- **Dewey Willis**, Code 597 Propulsion Branch, Goddard Space Flight Center
- **Kurt Wolko**, Code 597 Propulsion Branch, Goddard Space Flight Center

## Appendix A: Material Properties

Table A.1: StrutCombo Material Properties

<b>Strutcombo 17-4 Rho</b>	Mass Fraction	Thermal Conductivity ( $\frac{W}{mK}$ )	Specific Heat ( $\frac{J}{kgK}$ )	Density ( $\frac{kg}{m^3}$ )	Source
17-4 PH: Pin	0.21	10.46	460.5	N/A	[38]
6-4 Ti: Tab Itfc	0.24	7.2	554.3 <sup>a</sup>	N/A	[39]
6-4 Ti: Clevis	0.22	7.2	554.3 <sup>a</sup>	N/A	[39]
3-2.5 Ti: Strut	0.34	7.27	554.3 <sup>a</sup>	N/A	[40]
	<b>Mix:</b>	<b>7.91</b>	<b>534.66</b>	<b>Various</b>	
<b>Strutcombo 17-4 Rho Kmult 2x</b>		15.82	534.66	5156.22	
<b>Strutcombo RhoMod</b>		7.91	534.66	5866	
<b>Strutcombo RhoMod Kmult 2x</b>		15.82	534.66	5866	
<b>Strutcombo Upper RhoMod</b>		7.9	534.66	5646.3	
<b>Strutcombo Upper RhoMod Kmult 2.5x</b>		19.75	534.66	5646.3	

<sup>a</sup>Average value of specific heat used for T=7-120°C

Table A.2: TankTiCombo Material Properties

<b>TankTiCombo</b>	Mass Fraction	Thermal Conductivity ( $\frac{W}{mK}$ )	Specific Heat ( $\frac{J}{kgK}$ )	Density ( $\frac{kg}{m^3}$ )	Source
Aluminum Tape, Aluminum 1145-H19 Foil	0.13	225	904	2700	[41]
6-4 Titanium	0.78	7.23	554.14	4428.78	[39]
Diaphragm, EPDM/EPR mix (General)	0.09	0.25	2400	870	[42], [43]
	<b>Mix:</b>	<b>34.69</b>	<b>763.47</b>	<b>Various</b>	
<b>TankTiCombo Upper DeltaDistroRhoMod Kmult 1.5x</b>		52.13	763.5	6570	
<b>TankTiCombo Lower DeltaDistroRhoMod Kmult 2x</b>		69.5	763.5	7246.7	

Table A.3: Kapton Material Properties

	Thermal Conductivity ( $\frac{W}{mK}$ )	Specific Heat ( $\frac{J}{kgK}$ )	Density ( $\frac{kg}{m^3}$ )	Source
Kapton Tape	0.12	1090	1420	[44]

Table A.4: 6-4 Ti Material Properties

	6-4 Titanium				6-4 Titanium Rhomod Kmult 2x	6-4 Titanium Boom RhoMod		
Temperature (°C)	Thermal Conductivity (W/mK)	Specific Heat ( $\frac{J}{kgK}$ )	Density ( $\frac{kg}{m^3}$ )	Source	Thermal Conductivity ( $\frac{W}{mK}$ )	Density ( $\frac{kg}{m^3}$ )	Specific Heat ( $\frac{J}{kgK}$ )	Density ( $\frac{kg}{m^3}$ )
22	7.25	552.66	4428.78	[39]	14.21	6040.02	552.66	7345.7
23	7.25	552.66	4428.78		14.51	6040.02	552.66	7345.7
35	7.33	552.66	4428.78		14.67	6040.02	552.66	7345.7
50	7.41	552.66	4428.78		14.82	6040.02	552.66	7345.7
60	7.46	552.66	4428.78		14.91	6040.02	552.66	7345.7
70	7.5	552.66	4428.78		15.01	6040.02	552.66	7345.7
80	7.55	552.66	4428.78		15.11	6040.02	552.66	7345.7
90	7.62	552.66	4428.78		15.24	6040.02	552.66	7345.7
100	7.7	552.66	4428.78		15.39	6040.02	552.66	7345.7
110	7.8	552.66	4428.78		15.59	6040.02	552.66	7345.7
120	7.92	552.66	4428.78		15.85	6040.02	552.66	7345.7

Table A.5: 304 L Stainless Steel Material Properties

	304L Stainless Steel				304L SS KMult 2X
Temperature (°C)	Thermal Conductivity (W/mK)	Specific Heat ( $\frac{J}{kgK}$ )	Density ( $\frac{kg}{m^3}$ )	Source	Thermal Conductivity ( $\frac{W}{mK}$ )
22	13.73	484.41	7944.1	[38]	41.19
23	13.75	484.83	7944.1		41.24
30	13.87	488.18	7944.1		41.61
40	14.04	492.79	7944.1		42.13
50	14.22	497.39	7944.1		42.65
60	14.39	502.42	7944.1		43.17
70	14.56	507.02	7944.1		43.69
80	14.74	511.63	7944.1		44.21
90	14.91	516.23	7944.1		44.73
100	15.08	521.26	7944.1		45.25
110	15.26	525.86	7944.1		45.77



Table A.6: AR+N2 Mix Material Properties

<b>N2+AR Gas Mix</b>				
Temperature (°C)	Thermal Conductivity (W/mK)	Specific Heat ( $\frac{J}{kgK}$ )	Density ( $\frac{kg}{m^3}$ )	Source
20	0.025	970.59	3.416	[45]
25	0.026	970.59	3.416	
30	0.026	970.59	3.416	
35	0.026	970.59	3.416	
40	0.027	970.59	3.416	
45	0.027	970.59	3.416	
50	0.027	970.59	3.416	
55	0.028	970.59	3.416	
60	0.028	970.59	3.416	
65	0.028	970.59	3.416	
70	0.029	970.59	3.416	

## Appendix B: Boundary Conditions

Table B.1: Boundary Conditions

Temperature (°C)						
Time (s)	Gas Feed Tube <sup>a</sup>	Liquid Feed Tube <sup>a</sup>	Upper Ring to Upper Struts <sup>b</sup>	Lower Ring to Lower Right Strut	Lower Ring to Lower Left Strut	Lower Ring to Pin Plate
0	34.188	29.875	37.73	30.5	30.5	30.5
361	34.063	29.688	37.75	30.5	30.5	30.5
721	33.938	29.563	37.75	30.438	30.438	30.438
1021	33.813	29.438	37.75	30.375	30.375	30.375
1380	33.688	29.313	37.75	30.375	30.375	30.375
1681	33.563	29.188	37.75	30.375	30.375	30.375
1981	33.5	29.063	37.75	30.375	30.375	30.375
2341	33.375	28.938	37.75	30.375	30.375	30.375
2701	33.313	28.875	37.75	30.375	30.375	30.375
3001	33.25	28.75	37.77	30.438	30.438	30.438
3361	33.125	28.625	37.77	30.438	30.438	30.438
3721	33.063	28.563	37.77	30.5	30.5	30.5
4381	33	28.375	37.77	30.5	30.5	30.5
4681	32.938	28.25	37.78	30.563	30.563	30.563
5341	32.875	28.125	37.81	30.625	30.625	30.625
5700	32.875	28.063	37.83	30.688	30.688	30.688
6301	32.813	27.938	37.84	30.688	30.688	30.688
6661	32.813	27.938	37.84	30.75	30.75	30.75
6900	32.813	27.813	37.84	30.75	30.75	30.75

<sup>a</sup>Taken from 1-wire sensor nearest tank tube<sup>b</sup>Average of multiple 1-wire sensors

Table B.2: Radiative Properties

<b>Optical Properties</b>	<b>Emissivity</b>	<b>Ambient Temp (°C)</b>	<b>Source</b>
Axial Pin & Receiver	0.85	31	[46]
Exposed Tank Tabs	0.15	33	[46]
Struts	0.15	31	[46]
Tank Blanket	4.50E-03	31	[47]

## Appendix C: Sensor Location Details

Table C.1: Sensor Locations

<b>Sensor Location</b>	<b>1-Wire Sensor Designation</b>
Tank Belly Button Tab	PRP_051
Boomerang	PRP_053
Upper Right Tank Strut by Ring	PRP_054
Lower Left Tank Strut at Tank Tab	PRP_056
Lower Left Tank Strut by Ring	PRP_057
Gas Thermistor	PRP_068
Liquid Thermistor	PRP_072

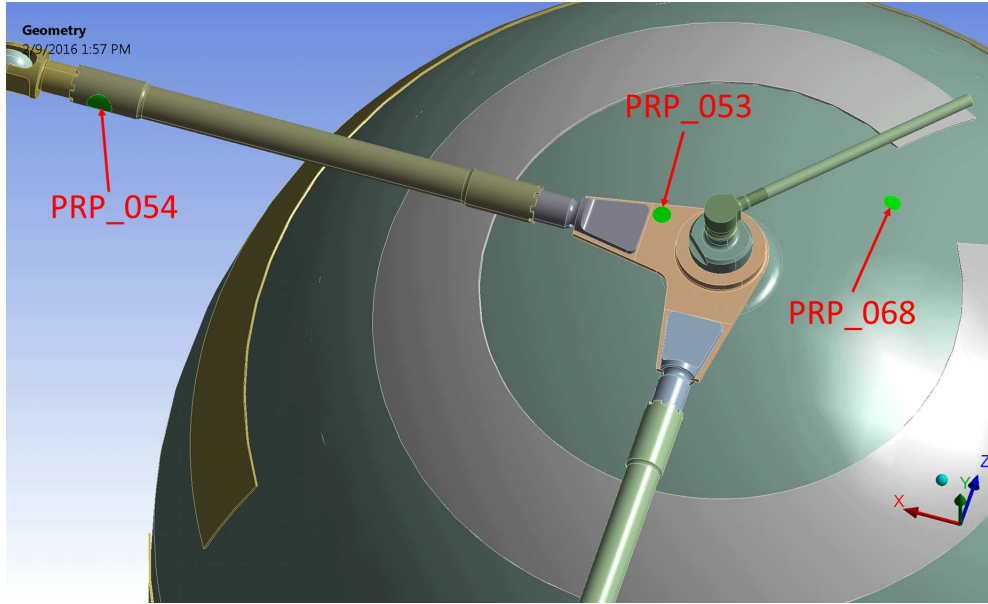


Figure C.1: Gas Side Sensor Locations.

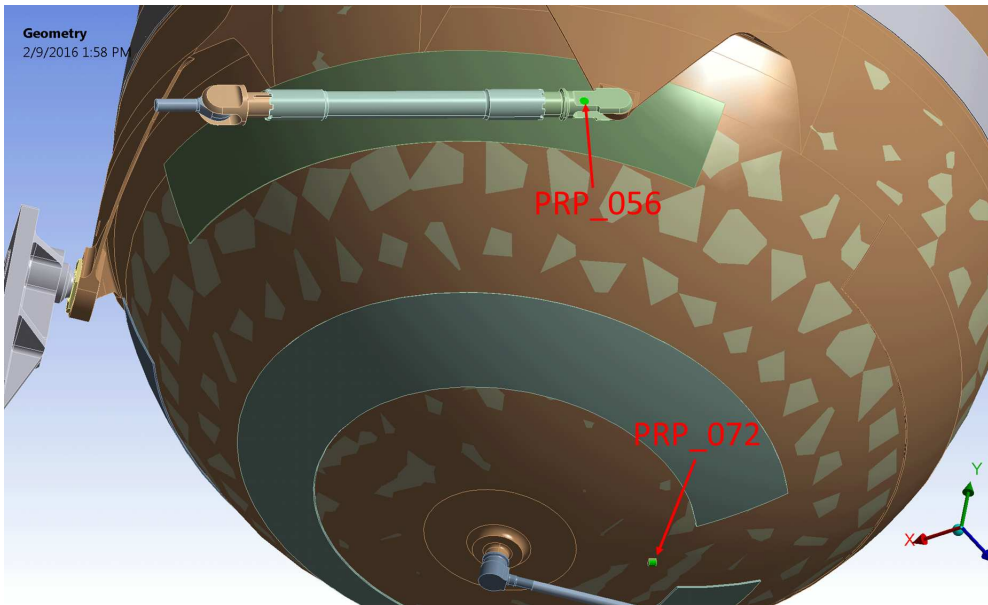


Figure C.2: Liquid Side Sensor Locations.

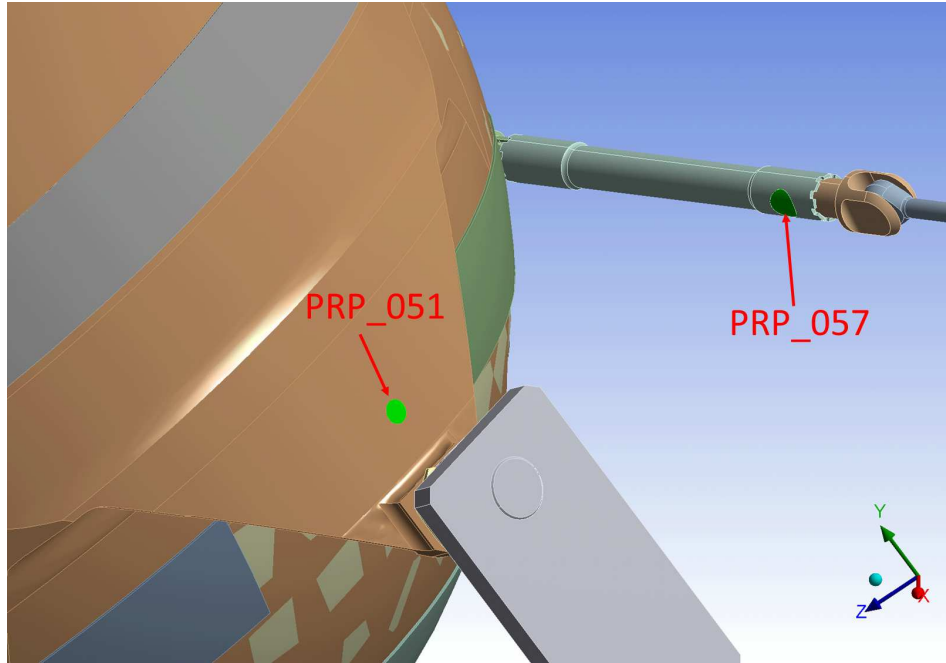


Figure C.3: Liquid Side Sensor Locations (cont.).



## Appendix D: Area-Weighted Average Temperature Algorithm

Temperature results in the ANSYS model were queried using a script that returned the area-weighted average temperature of a selected surface or face. This algorithm works as follows:

- All nodes on the face are selected
- Determine how many nodes are selected
- For all nodes, calculate the following:
  - Determine the area of the elements associated with each node
  - Find the product of the area and temperature
  - Store product of area and temperature in an array
- Sum all elements of the product of area and temperature array
- Sum all areas
- Calculate the average temperature on the surface by dividing the sum of the temperature\*area array by the sum of areas

Illustrative ANSYS APDL code for this algorithm is shown below:

```

*do,j,1,7
  cmsel,s,%selectname(1,j)%
*do,k,1,numss
  set,numls,k
*get,step_time,ACTIVE,,SET,TIME
outdata(k,1,j) = step_time

*stat
*get,n_nodes,node,,count
*dim,node_arnode,array,n_nodes
*dim,node_t_a,array,n_nodes
node_next=0

*do,ii,1,n_nodes
node_next=NDNEXT(node_next)
node_arnode(ii)=ARNODE(node_next)
node_t_a(ii)=ARNODE(node_next)*TEMP(node_next)
*enddo
*vscfun,sum_node_t_a,SUM,node_t_a(1)
*vscfun,sum_area,SUM,node_arnode(1)

temp_avg=sum_node_t_a/sum_area

outdata(k,2,j) = temp_avg
*enddo
*enddo

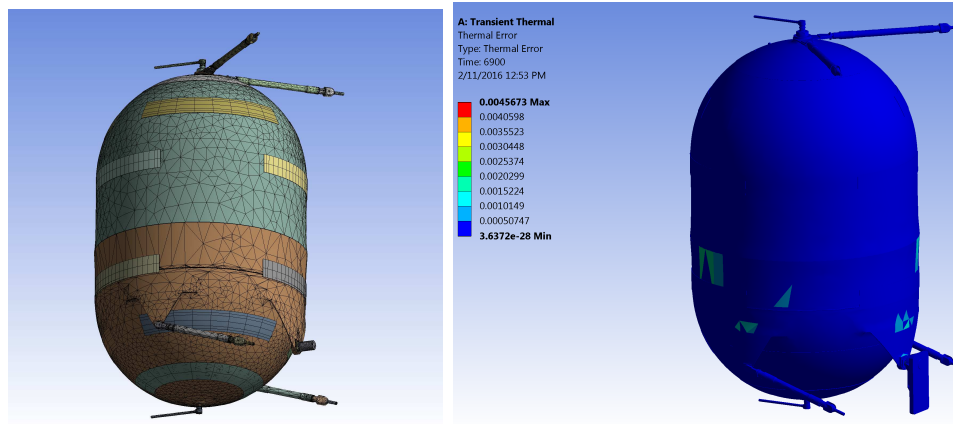
```

## Appendix E: Mesh Sensitivity Study Results

### E.1 Mesh Used in Analysis

Table E.1: Analysis Mesh Statistics

Mesh Statistics	
No. of Elements:	175,245
No. of nodes:	88,390
Typical Solve Time:	45 min



(a) Mesh

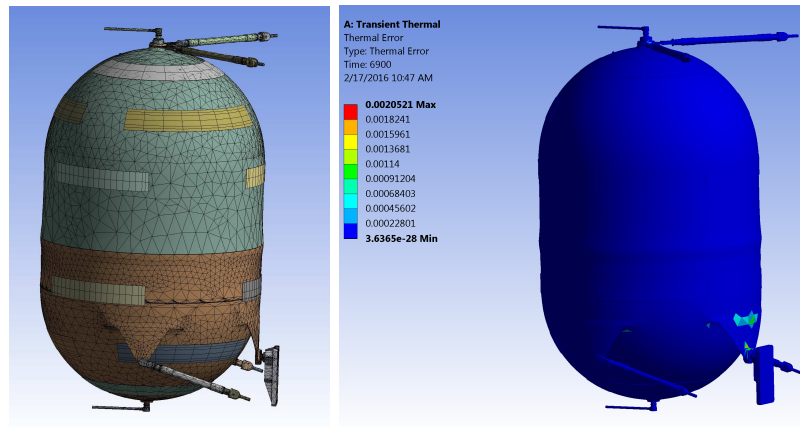
(b) Thermal Error

Figure E.1: Original Mesh & Thermal Error

## E.2 Refined Mesh

Table E.2: Refined Mesh Statistics

Mesh Statistics	
No. of Elements:	223,583
No. of nodes:	114,120
Typical Solve Time:	89 min



(a) Mesh

(b) Thermal Error

Figure E.2: Refined Mesh & Thermal Error

## E.3 Comparison of Mesh Results

The following table shows the temperature difference and percent difference between temperatures calculated using the analysis mesh and the refined mesh. There is no significant difference in results between the two meshes.

Table E.3: Comparison of Mesh Results

<b>Location</b>	<b>Temp. (°C) Analysis Mesh</b>	<b>Temp. (°C) Refined Mesh</b>	<b>Temp. (°C) Diff</b>	<b>% Diff</b>
Gas (PRP_068)	43.783	43.836	0.053	0.121
Boomerang (PRP_053)	40.885	40.902	0.017	0.042
Upper Strut (PRP_054)	35.104	35.105	0.001	0.003
Liq (PRP_072)	50.204	50.227	0.023	0.046
Belly Button Tab (PRP_051)	39.968	40.096	0.128	0.32
LL Strut Tab (PRP_056)	36.401	36.402	0.001	0.003
LL Strut by Ring (PRP_057)	31.057	31.057	0.000	0.000

## Appendix F: Model Change Log

Table F.1: Model Change Log

<b>Run</b>	<b>Changes</b>
4/29/2015, R0	Initial Run
7/10/2015, R0	Revised BCs, updated material props, simplified geometry, reduced mesh size for comp. speed
7/13/2015, R1	Revised BCs around strut interfaces & rings; updated ICs
7/13/2015, R2	Set conductance at Lower Left Tank Strut contact to 200 W/m <sup>2</sup> K
7/13/2015, R3	Set remove conductance values; multiply lower left strut conductivity by 1.5x
7/15/2015, R4	Reduced heater power by 2% to match AS-BUILT in model as best as possible (ANSYS model was 2-3% high); maint lower left strut increased conductance
7/20/2015, R5	Matched heater power in model; higher conductivity in lower left strut; higher conductivity in upper right strut
7/30/2015, R6	Increased conduct. By 1.5x on tank material; Matched heater power in model; higher conductivity in lower left strut; higher conductivity in upper right strut
8/7/2015, R7	Increased k on upper right strut 1.5x; reduced lower left strut k by 50%; Increased conduct. by 1.5x on tank material; Matched heater power in mode
8/17/2015, R8	Removed Temp BC on quad skin; Increased k on tank receiver pin and fitting by 1.5x; Returned Lower Left Strut k to baseline config; Increased k on upper right strut & boomerang by 3.0x; change system IC to 30 degC
8/18/2015, R9	All of R8 changes with following modifications: Increase k on receiver pin and fitting by 2.0x total; Change IC system back to 33 degC; Change IC on Lower Left Strut to 30.7 degC.
8/19/2015, R10	All of R9 changes with following modifications: Increase k on boomerang and upper right strut by 10x

Table F.2: Model Change Log (cont.)

Run	Changes
8/21/2015, R11	Fixed contact issues in struts; maintained all of R10 mods
8/24/2015, R12	Return everything to baseline config
8/26/2015, R13	Remove surrounding structure and apply structure BCs to strut & pin receiver plate instead. Worked out more contact issues with struts; baseline properties
8/27/2015, R14	Increase k on upper right and lower right struts by 2x; reduced BCs
8/27/2015, R15	Increased k on following: upper rt strut 2.5x; upper left strut 2x; tank bosses 2x; gas & liq prop lines 2x; upper & lower hemis 1.5x
8/31/2015, R16	Increased k on following: prop lines (gas & liq) to 3x total; boomerang to 2x total
9/1/2015, R17	Returned to R15 config; refined mesh on upper and lower hemispheres and pin
9/2/2015, R18	Modify R15 Config. Improve mesh on the following: upper & lower hemi by tank boss, all tabs on lower hemisphere, tank pin interface fitting; increase k on liq. Boss to 2.5x; increase k on upper & lower hemi by 2x total
9/4/2015, R19	R18 Config, but changed Lower tank strut BCs to both match PRP_056
9/9/2015, R20	R18 Config; Increased overall model mass (15%) to approx. match As Built Mass
9/10/2015, R21	Shifted mass from upper hemisphere to bottom hemisphere to simulate diaphragm position
9/11/2015, R22	NOTE: Some issue with model, maybe with update. Results suspect! Reverted back to R20 mass config; updated boomerang mass to correspond to measured mass; improved mesh on Liq-A htr



Table F.3: Model Change Log (cont.)

Run	Changes
9/29/2015, R23	Roll back to model saved on 9/1/2015 (R16); Update mass on struts, tank shell, boomerang. Brought model mass in line with as-measured tank mass. Distributed mass to maintain ratio between lower & upper tanks. All other parts of model are the same as R16 (mesh, conductivities, etc.)
10/1/2015, R24	R23 Config; modified IC on lower left strut to 25 deg C (strut body and tab interface)
10/6/2015, R25	R24 Config; Put heater heat flux BC on outside of heater instead of on the contact surface (inside) of heater
10/8/2015, R26	R24 Config; Defined upper and lower tank “zones” and applied heater BCs to zones (gas & liq circuits)
10/13/2015, R27	Change bonded contact Thermal Conductance on lower strut tab interfaces to clevis to value of 127. This is estimated to achieve 1-wire temperature at lower struts
10/20/2015, R28	Decrease lower strut conductance (75)
10/20/2015, R29	Decrease lower strut conductance (50)
10/20/2015, R30	Increase lower strut conductance (175)
10/20/2015, R31	Decrease lower strut conductance (20)
10/21/2015, R32	Maintain lower strut conductance (20); increase lower tank conductivity to 2x
10/22/2015, R33	Change PRP_051 selected face to patch; split out bottom ring interface temp BC to struts and receiver pin plate

Table F.4: Model Change Log (cont.)

Run	Changes
10/23/2015, R34	Change Upper Right Strut conductivity from 2.5x to 2x; change Upper Left Strut conductivity from 2x to 1.5x; change boomerang conductivity from 2x to 1.5x; change PRP_053 location to patch
10/26/2015, R35	Change upper hemi conductivity to 1x (baseline); change gas inlet tube conductivity to 1x (baseline)
10/27/2015, R36	Change upper strut assy conductivities from R34 values to all baseline (1x)
10/27/2015, R37	Increase upper right strut conductivity to 1.5x, create better contact faces on boomerang for beertab interface
10/27/2015, R38	Address contact issues on Boomerang to beer tabs
10/30/2015, R39	Change Boomerang Left and Right Interface conductivity to 150
11/2/2015, R40	Change Boomerang Left and Right Interface conductivity to 100
11/2/2015, R41	Change Boomerang Left and Right Interface conductivity to 20
11/3/2015, R42	Revert Boomerang conductance to Program Control; change upper strut clevis to pin conductance to 150
11/3/2015, R43	Revert Boomerang conductance to Program Control; change upper strut clevis to pin conductance to 100
11/4/2015, R44	Revert Boomerang conductance to Program Control; change upper strut clevis to pin conductance to 50

Table F.5: Model Change Log (cont.)

Run	Changes
11/5/2015, R45	Revert upper strut conductances to baseline; set boomerang conductances to 20 each, set upper hemi conductivity to 1.5x
11/5/2015, R46	Revert boomerang conductances to baseline; change upper strut end conductances to 50; change upper right strut conductivity to 2.5x; maintain upper hemi conductivity at 1.5x
11/5/2015, R47	Change upper strut end conductances to 100; maintain upper right strut conductivity to 2.5x; maintain upper hemi conductivity at 1.5x
11/6/2015, R48	Change upper strut end conductances to 150; maintain upper right strut conductivity to 2.5x; maintain upper hemi conductivity at 1.5x
11/20/2015, R48a	Average temperature over selected area at each 1-wire location recorded below; no other changes
11/20/2015, R49a	Change boomerang conductance to 20 on left and right; moved boomerang and upper strut assy up to fix interference problem; updated boomerang-upperhemi contact surfaces; maintain TCC changes made in R48; record average temperatures below
11/23/2015, R50a	Uncertainty analysis: +Q on heaters; R49a config; record average temperatures below
11/24/2015, R51a	Uncertainty analysis: -Q on heaters; R49a config; record average temperatures below
11/25/2015, R52a	Run Simulation to 10,300s & compare to test data; R49a config; record average temperatures below
11/30/2015, R53a	Correct mass distribution error in tank (upper hemi); record average temperatures below
12/1/2015, R54a	Uncertainty analysis: +Q on heaters; R53a config; record average temperatures below

Table F.6: Model Change Log (cont.)

Run	Changes
12/1/2015, R55a	Uncertainty analysis: -Q on heaters; R53a config; record average temperatures below
12/4/2015, R56a	Uncertainty analysis: MASS MINUS; Q on heaters; R53a config; record average temperatures below
12/4/2015, R57a	Uncertainty analysis: MASS PLUS; Q on heaters; R53a config; record average temperatures below
2/5/2016, R59a	Uncertainty analysis: BC Temperatures +10 deg C; Q on heaters; R53a config; record average temperatures below
2/6/2016, R59b	Uncertainty analysis: BC Temperatures -10 deg C; Q on heaters; R53a config; record average temperatures below

Table F.7: Model Change Log (cont.)

Run	Changes
2/8/2016, R60	Effect of S/C enclosure. Surrounding enclosure in model re-enabled; R53a config; record average temperatures below
2/9/2016, R61	R53a config, but modify N2+Ar gas mix to have constant density (mass) in model. Re-run to see if major effect on system; record average temperatures below
2/12/2016, R62	R53a config with N2+Ar gas mix to have constant density (mass) in model. Refined tank mesh to see if drastic effects on model; record average temperatures below
2/12/2016, R63	R62 Config (refined mesh model), reduced lower right strut k to 1.5x ; record average temperatures below
2/13/2016, R64	R53a Config (baseline mesh model), reduced gas tube k from 3x to baseline ; record average temperatures below. Observed not appreciable difference between temps in R53a (3x cond on gas tube) in R64 results
2/14/2016, R65	All results reviewed. Change R53a Config to following: Lower Strut TCCs 20; Upper Strut TCCs baseline; Boomerang TCC 20, Lower Left strut kmult 1.0x; Lower Right strut kmult 2.0x; upper left strut kmult 1.0x; Upper right strut kmult 1.5x; lower hemi kmult 2.0x; upper hemi kmult 1.5x; record avg temps below

## Bibliography

- [1] National Aeronautics and Space Administration. NASA's MMS Observatories Stacked For Testing. The Magnetospheric Multiscale (MMS) Mission, Jul 2015. Web. Accessed 05-Feb-2016. [https://www.nasa.gov/sites/default/files/mmsstacked\\_beauty\\_small.jpg](https://www.nasa.gov/sites/default/files/mmsstacked_beauty_small.jpg).
- [2] Karen C. Fox. NASA's MMS Spacecraft Achieve Tightest Flying Formation Ever. The Magnetospheric Multiscale (MMS) Mission, October 2015. Web. Accessed 10-Feb-2016. <http://www.nasa.gov/feature/goddard/nasas-mms-spacecraft-achieve-tightest-flying-formation-ever>.
- [3] National Aeronautics and Space Administration. Unlocking the Secrets of the Electron Diffusion Region. The Magnetospheric Multiscale (MMS) Mission, Mar 2016. Web. Accessed 05-Feb-2016. <http://mms.gsfc.nasa.gov/science.html>.
- [4] Kurt Wolko. Propulsion Top Model Assembly, MMS. 2103100E- Internal NASA drawing, Goddard Space Flight Center, Code 461, April 2013.
- [5] Andres Aparicio and Boris Yendler. Thermal Propellant Gauging at EOL, Telstar 11 Implementation. In *SpaceOps 2008*. SpaceOps Conferences, AIAA, May 2008. doi:10.2514/6.2008-3375.
- [6] David G. Gilmore, editor. *Spacecraft Thermal Control Handbook, Vol. 1: Fundamental Technologies*, volume 1, chapter 19, page 748. The Aerospace Press, El Segundo, CA, second edition, 2002.
- [7] David G. Gilmore, editor. *Spacecraft Thermal Control Handbook, Vol. 1: Fundamental Technologies*, volume 1, chapter 19, page 724. The Aerospace Press, El Segundo, CA, second edition, 2002. Fig. 19.3.
- [8] Boris Yendler. Review of Propellant Gauging Methods. In *44th AIAA Aerospace Sciences Meeting and Exhibit*. Aerospace Sciences Meetings, AIAA, January 2009. doi:10.2514/6.2006-939.

- [9] Boris Yendler and S. Chernikov. Comparison of Gauging Methods for Orbital's GEOSTar 1 Satellites. In *SpaceOps 2014 Conference*. SpaceOps Conferences, AIAA, May 2014. doi:10.2514/6.2014-1810.
- [10] Eric Stoneking. Email Correspondence, 2016. Question on Thesis. NASA-GSFC, Code 591, Navigation, Guidance & Control Systems.
- [11] Joseph Miller, Stephen McKim, et al. TRMM Remaining Fuel Estimation Report. Internal NASA Presentation, Goddard Space Flight Center, Code 597, August 2013.
- [12] How does FDF calculate the Thrust Scale Factor? Internal NASA Memo, Goddard Space Flight Center, March 2001.
- [13] Amit Lal and B.N. Raghunandan. Uncertainty analysis of propellant gauging system for spacecraft. *Journal of Spacecraft and Rockets*, 42(5):943–946, September - October 2005. doi: 10.2514/1.9511.
- [14] M. V. CHOBOTOV and G. P. PUROHIT. Low-gravity propellant gauging system for accurate predictions of spacecraft end-of-life. *Journal of Spacecraft and Rockets*, 30(1):92–101, January 1993. doi: 10.2514/3.25475.
- [15] LLC. YSPM. Our Team. Web. Accessed 08-Feb-2016. <http://www.yspm.net/team.html>.
- [16] Boris Yendler and T. Narita. Thermal Propellant Gauging System for BSS 601. In *25th AIAA International Communications Satellite Systems Conference (organized by APSCC)*. International Communications Satellite Systems Conferences (ICSSC), AIAA, April 2007. doi:10.2514/6.2007-3149.
- [17] Boris Yendler. Unconventional Thermal Propellant Gauging System. In *45th AIAA Aerospace Sciences Meeting and Exhibit*. Aerospace Sciences Meetings, AIAA, January 2007. doi:10.2514/6.2007-1363.
- [18] Boris Yendler, Ibrahim Oz, and Lionel Pelenc. Thermal Propellant Gauging, SpaceBus 2000 (Turksat 1C) Implementation. In *AIAA SPACE 2008 Conference & Exposition*. SPACE Conferences and Exposition, AIAA, September 2008. doi:10.2514/6.2008-7697.
- [19] Boris Yendler. Implementation of Thermal Gauging Method for SpaceBus 3000A (ArabSat 2B). In *SpaceOps 2012 Conference*. SpaceOps Conferences, AIAA, June 2012. doi:10.2514/6.2008-7697.
- [20] Boris Yendler, S. Chernikov, et al. Implementation of Thermal Gauging Method for Orbital Sciences Corporation's GEOSTar 1 Satellite. In *SPACE 2013 Conference and Exposition*. SPACE Conferences and Exposition, AIAA, September 2013.

- [21] Ken Brakke. Surface Evolver. Susquehanna University, August 2013. Vers. 2.70, Computer Software. <http://facstaff.susqu.edu/brakke/evolver/evolver.html>.
- [22] C&R Technologies. Thermal Desktop. Cullimor & Ring Technologies, 2016. Computer Software. <http://www.crtech.com/thermaldesktop.html>.
- [23] Robyn Nariyoshi, Sergey Chernikov, and Boris Yendler. Prediction of Spacecraft Remaining Life - Challenges and Achievements. In *49th AIAA/ASME/SAE/ASEE Joint Propulsion Conference*. Joint Propulsion Conferences, AIAA, July 2013. doi:10.2514/6.2013-4162.
- [24] ANSYS Corporation. ANSYS. Thermal Analysis, 2016. Vers. 13.0, Computer Software. <http://www.ansys.com/Products/Structures/Thermal>.
- [25] Stephen A. McKim. MMS Propellant Tank Thermal Capacitance Model, PIP Level II Report. Internal NASA Report, Goddard Space Flight Center, Code 597, February 2012.
- [26] Stephen A. McKim and Amanda Steckel. MMS Propellant Tank Thermal Capacitance Model. In *AIAA Region 1 Young Professional, Student and Education Conference*. Johns Hopkins University Applied Physics Laboratory, AIAA, November 2012. Presentation.
- [27] National Aeronautics and Space Administration. Magnetospheric Multiscale Observatory Integration. The Magnetospheric Multiscale (MMS) Mission, March 2016. Web. Accessed 10-Feb-2016. [http://mms.gsfc.nasa.gov/observatory\\_integration/obs1/obs1\\_07.html](http://mms.gsfc.nasa.gov/observatory_integration/obs1/obs1_07.html).
- [28] John H. Lienhard IV and John H. Lienhard V. *A Heat Transfer Textbook*, chapter 8, page 412. Phlogiston Press, Cambridge Massachusetts, fourth edition, 2011. Web. <http://ahtt.mit.edu>.
- [29] Warren M. Rohsenow and Harry Y. Choi. *Heat, Mass, and Momentum Transfer*, chapter 7, page 162. Prentice-Hall, Inc., Englewood Cliffs, New Jersey, 1961. Eqn 7.69.
- [30] Richard Shelley. APU Diaphragm Testing Test Plan. Technical Report TP-WSTF-682, National Aeronautics and Space Administration, White Sands Test Facility, January 1992. Web. Accessed 10-Feb-2016. <http://ntrs.nasa.gov/archive/nasa/casi.ntrs.nasa.gov/19930020198.pdf>.
- [31] National Aeronautics and Space Administration. Magnetospheric Multiscale Spacecraft Assembly Propulsion Images. The Magnetospheric Multiscale (MMS) Mission, March 2016. Web. Accessed 10-Feb-2016. [http://mms.gsfc.nasa.gov/spacecraft\\_assembly/propulsion/propulsion\\_18.html](http://mms.gsfc.nasa.gov/spacecraft_assembly/propulsion/propulsion_18.html).



- [32] ANSYS Inc. *POST1-Error Approximation Technique, Mechanical APDL Theory Reference*, chapter Error Approximation Technique for Temperature-Based Problems, page 17.7.2. SAS IP, Inc., Cannonsburg, PA, release 16.0 edition, 2014.
- [33] SAS IP Inc., Cannonsburg, PA. *Introduction to ANSYS Mechanical*, first edition, January 2010. Training materials. Slides 8-38 & 8-39.
- [34] Hugh W. Coleman and W. Glenn Steele. *Experimentation, Validation, and Uncertainty Analysis for Engineers*, chapter 4, pages 86–94. John Wiley & Sons, Inc., Hoboken, New Jersey, third edition, 2009.
- [35] Michael Commons. MMS Flight Thermal Model Correlation Summary. 461-TCS-ANYS-0418 Rev.- Internal NASA Presentation, Goddard Space Flight Center, Code 545, August 2015.
- [36] Ross L. Finney and Jr. George B. Thomas. *Calculus*, chapter 3, pages 187–190. Addison-Wesley Publishing Company, Inc., Reading, Massachusetts, second edition, 1994. Section 3.8.
- [37] Yingwei Wang. Methods for Solving Nonlinear Equations. Department of Mathematics, Purdue University, West Lafayette, IN. Class notes. Web. Accessed 08-April-2016. <https://www.math.purdue.edu/~wang838/notes/newton.pdf>.
- [38] Jr. William F. Brown, Chuck Gibson, et al., editors. *Aerospace Structural Metals Handbook*, volume 2. CINDAS/USAF CRDA Handbooks Operation, Purdue University, West Lafayette, IN, 1999 edition, March 1998.
- [39] United States Federal Aviation Administration et al. *MMPDS-40 Metallic materials properties development and standardization (MMPDS)*. Federal Aviation Administration, Washington, D.C., April 2008.
- [40] Jr. William F. Brown, Chuck Gibson, et al., editors. *Aerospace Structural Metals Handbook*, volume 4. CINDAS/USAF CRDA Handbooks Operation, Purdue University, West Lafayette, IN, 1999 edition, March 1998.
- [41] Aluminum 1145-H19-Foil. MatWeb, LLC, 1996-2016. Web. Accessed Sept. 2014. <http://www.matweb.com>.
- [42] Ethylene Propylene Diene Rubber (EPDM, EPT). MakeItFrom.com, 2009-2015. Web. Accessed 11-Nov-2014. <http://www.makeitfrom.com/material-properties/Ethylene-Propylene-Diene-Rubber-EPDM-EPT/>.
- [43] LANXESS Buna LLC, Pittsburgh, PA. *Buna EP Ethylene Propylene Rubber*, 2007 edition, May 2007.

- [44] DuPont, Wilmington, DE. *Summary of Properties for Kapton Polyimide Films*, 2016. Web: <http://www.dupont.com/content/dam/dupont/products-and-services/membranes-and-films/polyimide-films/documents/DEC-Kapton-summary-of-properties.pdf>.
- [45] NIST Standard Reference Database 69. Isobaric Properties for Nitrogen at 44.7 psia. NIST Chemistry WebBook, 2016. Web. Accessed Sept. 2014. <http://webbook.nist.gov/chemistry/fluid/>.
- [46] Code 545 GSFC Thermal Branch. Meeting with Jason Solimani Notes, April 2015. Internal meeting notes: Tank thermal properties.
- [47] Rommel Zara. MMS Propulsion Tank MLI Effective Emittance Test and Model Correlation Report. 461-TCS-RPT-0039 Rev.- Internal NASA Report, Goddard Space Flight Center, Code 545, February 2010.